Large Scale Structures and Radio Galaxy Survey

Song Chen

Supervisor: *Prof. Dr. Dominik J. Schwarz*

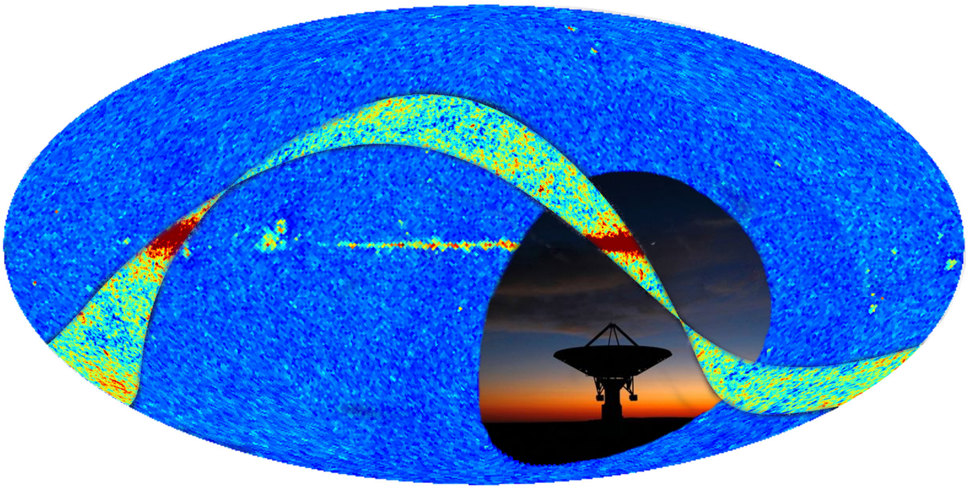

Faculty of Physics

University Bielefeld

A thesis submitted for the degree of

Doctor Rerum Naturalium

September 2015

Relevant Publication:

Song Chen and Dominik J. Schwarz,*Fluctuations of differential number counts of radio continuum sources*, Phys. Rev. D91 (2015) 043507, arXiv:1407.4682

Dominik J. Schwarz, David Bacon, Song Chen, Chris Clarkson, Dragan Huterer, Martin Kunz, Roy Maartens, Alvise Raccanelli, Matthias Rubart, Jean-Luc Starck, *Testing foundations of modern cosmology with SKA all-sky surveys*, PoS AASKA14 (2015) 032, arXiv:1501.03820

Song Chen and Dominik J. Schwarz, *The angular two-point correlation of NVSS galaxies revisited*, submitted to A&A, arXiv:1507.02160

Cover page: NRAO VLA Sky Survey (NVSS) catalogue number density map filled with a radio telescope dish of the KAT-7 Array pointing skyward at the proposed South African site for the Square Kilometre Array (SKA) telescope (Image by: MIKE HUTCHINGS / REUTERS). On top of it is the CMB temperature fluctuations from the Wilkinson Microwave Anisotropy Probe (WMAP).

Abstract

Most cosmological analyses on radio galaxies interpret observations in the homogeneous and isotropic flat Friedmann-Lemaître-Robertson-Walker Universe. However, the real Universe is not perfectly homogeneous and isotropic especially on small scales. In this thesis we investigate the number counts of sources in radio continuum surveys, including all linear order perturbations in a perturbed flat Friedmann-Lemaître-Robertson-Walker Universe. The results are expressed in terms of gauge-invariant quantities and without assuming any specific gauge condition. This general approach allows us to recover gauge invariance explicitly. With the complete derivations of the covariant volume integral on the past light cone, we have identified several contributions to the number counts. To clarify their underlying physics, we present each contribution in terms of scalar, vector and tensor modes. This theoretical framework promises to be widely applicable to continuum radio galaxy surveys to model the expected angular power spectrum and two-point correlation.

We also measure the angular two-point correlation and angular power spectrum from the NRAO VLA Sky Survey (NVSS) of radio galaxies. Contrary to previous claims in the literature, we show that it is consistent with primordial Gaussianity on all angular scales and it is consistent with the best-fit cosmological model from the Planck analysis, as well as the redshift distribution obtained from the Combined EIS-NVSS Survey Of Radio Sources (CENSORS). Our analysis is based on an optimal estimation of the two-point correlation function and makes use of a new mask, which takes into account direction dependent effects of the observations, side lobe effects of bright sources and galactic foreground. We also use a lower flux threshold and take the cosmic radio dipole into account. The latter turns out to be

an essential step in the analysis. This improved cosmological analysis of the NVSS stresses the importance of a flux calibration that is robust and stable on large angular scales for future radio continuum surveys. Considering the fact that the statistical error of the NVSS two-point correlation is too large to detect all relativistic linear order effects, only the redshift space distortion and gravitational lensing effect are investigated in more detail.

To my family.

Contents

List of Figures **iv**

List of Tables **viii**

1 The Large Scale Structure of the Universe **1**

1.1 Homogeneity and Isotropy 1

1.2 Inhomogeneity and Cosmological Perturbations 4

1.3 The Composition of the Universe 5

1.4 History of Radio Cosmology 6

1.5 Radio Cosmology after Planck 8

2 Perturbation Theory and Galaxy Number Counts **13**

2.1 Metric Perturbations 13

2.1.1 Method I : Passive Coordinate Transformations 14

2.1.2 Method II: Active Diffeomorphisms 15

2.2 Gauge-invariant Metric Potentials 16

2.3 Galaxy Number Counts I 17

2.4 Coordinates of the Observer 18

2.4.1 Conformal Transformation 18

2.4.2 Redshift Distortions 20

2.4.3 Specific Flux Fluctuations 22

2.4.4 Number Counts in Observed Spherical Coordinates and Lensing Effect 30

2.5 Galaxy Number Counts II 33

2.5.1 Radio Galaxy Luminosity Function 34

3 Predictions for Galaxy two-point Statistics **37**
3.1 Angular Power Spectrum 38
3.2 Angular two-point Correlation Function 40
3.3 Radio Dipole Correction 42

4 NVSS Angular Power Spectrum and two-point Correlation **44**
4.1 The NVSS Catalogue 44
4.2 Lower Flux Density Threshold 46
4.3 Masking Strategy 48
4.4 Theoretical Expectation 52
4.5 Results 54

5 Discussion **59**
5.1 Cosmological Implications 59
5.2 Residual Systematics 62
5.3 Parity Asymmetry 65
5.4 Next-to-leading order Effects in the Radio Galaxy Angular Power Spectrum 65

6 Conclusion **68**

References **73**

List of Figures

1.1 The large scale structure as observed with galaxy redshift surveys made by corresponding surveys. Top: 2dF galaxy redshift survey [1], Bottom left: Sloan Digital Sky Survey [2], Bottom right: WiggleZ Dark Energy Survey [3]. One can see the isotropic galaxy distribution on large scales. 3

1.2 The CMB temperature anisotropy spectrum from Planck 2015 [4]. The red solid line shows the best fit ΛCDM model 5

1.3 Summary of main cosmological tests using radio sources as probes by Ekers and Miley in 1977 [5] 7

1.4 Hubble Space Telescope images of five 3CR radio galaxies with radio emission contours from the Cambridge four-element interferometer, from [6]. In order of increasing radio size (D): (a) 3C 266 (upper left, $z = 1.272$, $D = 39$ kpc); (b) 3C 368 (centre left, $z = 1.132$,$D = 73$ kpc); (c) 3C 324 (upper right, $z = 1.21$,$D = 96$ kpc); (d) 3C 280 (centre right, $z = 0.996$,$D = 117$ kpc); (e) 3C 65 (bottom, $z = 1.176$,$D = 155$ kpc). . . 9

1.5 Mean angular size against redshift for 82 compact sources by Kellermann [7]. The solid curves represent the expected dependece for FLRW cosmological models for a standard source with a component separation of 41 parsec and deceleration parameter q_0 of 0, 1/2 and 1 and the steady-state model (SS); the dashed line shows the $1/z$ law observed for the separation of double-lobed extend sources. 10

1.6 Top: The cartoon shows how the CMB photon trajectories are affected by the matter distribution between the receiver and the last scattering surface. Bottom: The gravitational lensing power spectrum of the cosmic microwave background from the Planck 2015 results [8]. (Made by ESA and the Planck Collaboration) 11

2.1 Diffeomorphism related background spacetime and physical spacetime . 15
2.2 Radio galaxy spectrum. Top: FIR and radio spectrum of M82 (Condon, J. J. 1992, ARA&A, 30, 575); Bottom: radio spectrum of Cygnus A, Cassiopeia A and Virgo A (Baars, J. W. M. et al. 1977, A&A, 61, 99.) 23
2.3 Affine parameter convention of a light ray in a radio observation. 25
2.4 Flux-redshift relation for different specific luminosities typical for AGNs. The standard Λ cold dark matter model has been adopted, and the spectral index α has been chosen to be 0.75. 28
2.5 Observed position vs. background position. 31
2.6 Local luminosity function at 1.4 GHz derived separately for radio-loud AGNs and SF galaxies in the 6 degree Field Galaxy Survey (6dFGS)-NVSS sample, copy from [9]. 35

3.1 A typical sky coverage of a radio galaxy catalogue with declination $\delta > -40^\circ$ and galactic latitude $|b| > 5^\circ$ 41
3.2 Dimensionless geometric form factor $G_p(\theta)$ of catalogues with sky coverage identical to Fig. 3.1 42

4.1 Surface density σ of the NVSS source catalog in galactic coordinates in Mollweide projection, shown at HEALPIX resolution $Nside = 32$. The color bar shows the surface density in units of number of objects per square degree. Here we include all objects contained in the catalogue. . 45
4.2 Surface density fluctuation, $\Delta\sigma/\overline{\sigma}$, of the NVSS catalogue as a function of declination for several flux density thresholds. The error bars assume Poisson distributed source counts and we mask the region $|b| \leq 5^\circ$. For clarity, the horizontal positions of the $S > 5$ mJy and $S > 15$ mJy data points are slightly offset. 47

4.3 Nearby source count histogram (disks with radius 0.6°). The red bins correspond to nearby source counts around bright radio galaxies with $S > 2.5$ Jy. The blue bins correspond to 1000 randomly picked positions outside the galactic plane ($|b| > 5°$). The maximum of randomly picked counts results in 49 neraby sources. 49

4.4 Poissonness plot of the nearby source counts. λ_o is the mean nearby count over the survey area. N is the total number of sources with $S > 2.5$ Jy. The solid horizontal line corresponds to a perfectly Possion distributed nearby source count. The error bars denote the 99% confidence levels. 49

4.5 NVSS position uncertainty map, relative to the mean beam width $\theta_{\mathrm{FWHM}} = 45''$. 50

4.6 NVSS65 mask. The orange region makes up 64.7% of the sky. Yellow pixels are close to the galactic plane $|b| \leq 5°$ and are excluded to suppress galactic point sources and foregrounds. Blue pixels are excluded due to large position errors. Red and black pixels contain bright sources with significant side lobe effects, black pixels additionally overlap with pixels with high position error. 51

4.7 Surface density of the NVSS source catalog for a flux density threshold of $S > 15$ mJy and applying the NVSS65 mask, shown in galactic coordinates at pixel size $Nside$=32. The color bar shows the surface density σ in units of number of objects per square degree. 52

4.8 NVSS angular two-point correlations for a 5° galactic latitude mask with and without dipole correction. 55

4.9 Angular two-point correlation function $w(\theta)$ from 5° galactic latitude cut (top panel) and the NVSS65 mask (bottom panel). In both cases we include a dipole correction. 56

4.10 Angular two-point correlation function at $1° < \theta < 20°$ from the NVSS catalogue with dipole correction for two different masks. 57

4.11 NVSS angular power spectrum C_l for $S > 15$ mJy, dipole corrected and NVSS65 mask. C_l is evaluated via a Legendre transformation from the angular two-point correlation function. The solid line and the band around it show the theoretical prediction and its cosmic variance. 58

5.1 Angular two-point correlation function as a test for the Hubble constant H_0. The measurement uses the NVSS65 mask with dipole correction. . . 60

5.2 Angular two-point correlation function for different redshift distributions. 61

5.3 Top panel: Surface density fluctuation ($\Delta\sigma/\overline{\sigma}$) of NVSS sources at $S >$ 60 mJy and $S >$ 15 mJy after applying the NVSS65 mask. Bottom panel: The theoretical rms noise level of the NVSS catalogue from [10]. The VLA geodetic latitude is $34°04'44''$. 63

5.4 The HEALPIX pseudo-C_l of the NVSS catalogue with NVSS65 mask for $S >$ 15 mJy and radio dipole subtracted. 64

5.5 WMAP 7-year angular power spectrum 65

5.6 The angular power spectrum difference $C_l^{D+RsD} - C_l^D$ with the NVSS redshift distribution and Gaussian bias. 66

5.7 The angular power spectrum C_l with and without lensing effect. 67

List of Tables

4.1 χ^2-values testing for the isotropy in declination of the NVSS surface density (here with 13 degrees of freedom). 47

4.2 NVSS dipole for various flux density thresholds, measured by means of Healpix at resolution $Nside = 32$ after applying the NVSS65 mask. For comparison we quote the expected kinetic dipole for NVSS radio sources, based on the observed CMB dipole. 54

4.3 χ^2-test for $w(\theta)$ for 49 data points [excluding first bin: $0 < \theta < 3.6°$]. Note: We neglect the correlation between the data points. 57

Chapter 1

The Large Scale Structure of the Universe

1.1 Homogeneity and Isotropy

The contemporary cosmological models are based on the cosmological principle, which states that the Universe, smoothed over large enough scales, is essentially homogeneous and isotropic. Isotropy means given an observer point, the Universe looks the same in every direction. Homogeneity states that matter and radiation are uniformly distributed throughout the Universe.

Based on this principle, Friedmann and Lemaître began their pioneering investigations on cosmology. However, the observational basis for the cosmological principle was not known at that time. Their motivation was driven by considering the simplest possible large scale structure of the Universe and the Copernican principle. The Copernican principle state that there is no specially favored position in the Universe. Since a universe that is isotropic everywhere (three distinct points are enough [11]) is also homogeneous, the cosmological principle is a straightforward conclusion from the combination of the Copernican principle and the isotropy around ourself in a smooth spacetime.

The small structure in the Universe seems to contradict the cosmological principle, for example the center of our Sun and interstellar space are completely different. Considering such fact, one only applies the cosmological principle on the very large scales, and interprets it in a statistical sense. Several large scale statistical homogeneity tests (e.g. [12, 13]) have been applied to the Two-degree-Field Galaxy Redshift Survey [1], the Sloan Digital Sky Survey [2] and the WiggleZ Dark Energy Survey [3], shown in Fig. 1.1. These tests confirmed that the Universe is spatially isotropic and homogeneous at scale above 100 Mpc.

The large scale isotropic and homogeneous cosmology picture describes with great success a wide variety of observational data. Nevertheless, one may still question whether the initial conditions giving rise to such a universe are natural or not. Cosmological inflation [14, 15, 16, 17], proposed in the 1980s, gives a mechanism which can explain the initial conditions. According to the simplest inflation theory, the Universe underwent an extremely rapid exponential expansion, namely inflation. The theory allows the Universe to start from a reasonable small and nearly homogeneous and isotropic patch of spacetime. The previously existing anisotropies and inhomogeneities are diluted during inflation, which leads to the flat, statistically isotropic and homogeneous Universe today.

One of the strongest basis for the cosmological principle is coming from the Cosmic Microwave Background Radiation (CMB). In 1965, Penzias and Wilson first observed the CMB with Earth based Holmdel horn antenna. Later on, the space mission Cosmic Background Explorer (COBE) was launched in 1989, which is regarded as the starting point for cosmology as a precision science. They find the CMB fills the entire sky with remarkably uniform intensity, except the galactic plane and kinetic dipole due to our motion with respect to the CMB rest frame.

In order to understand the origin of the CMB, we need to briefly review the history of the Universe. After the inflationary period, the Universe reverted to a power law expansion rate, and the temperature continued to drop. When the temperature had dropped to around 3000 K, protons and electrons were able to form stable hydrogen atoms. Before that all baryonic matter was in a plasma state and the photon mean free path was short due to Thomson scattering from the free charged particles. After the formation of atoms, the Universe is transparent until the time of reionization. At which time the high energetic photons emitted from the first stars reionize the Universe again. The light released from the early plasma slightly scatter by the free electrons after the reionization. It is perceived today as the CMB, the afterglow of the Big Bang's heat.

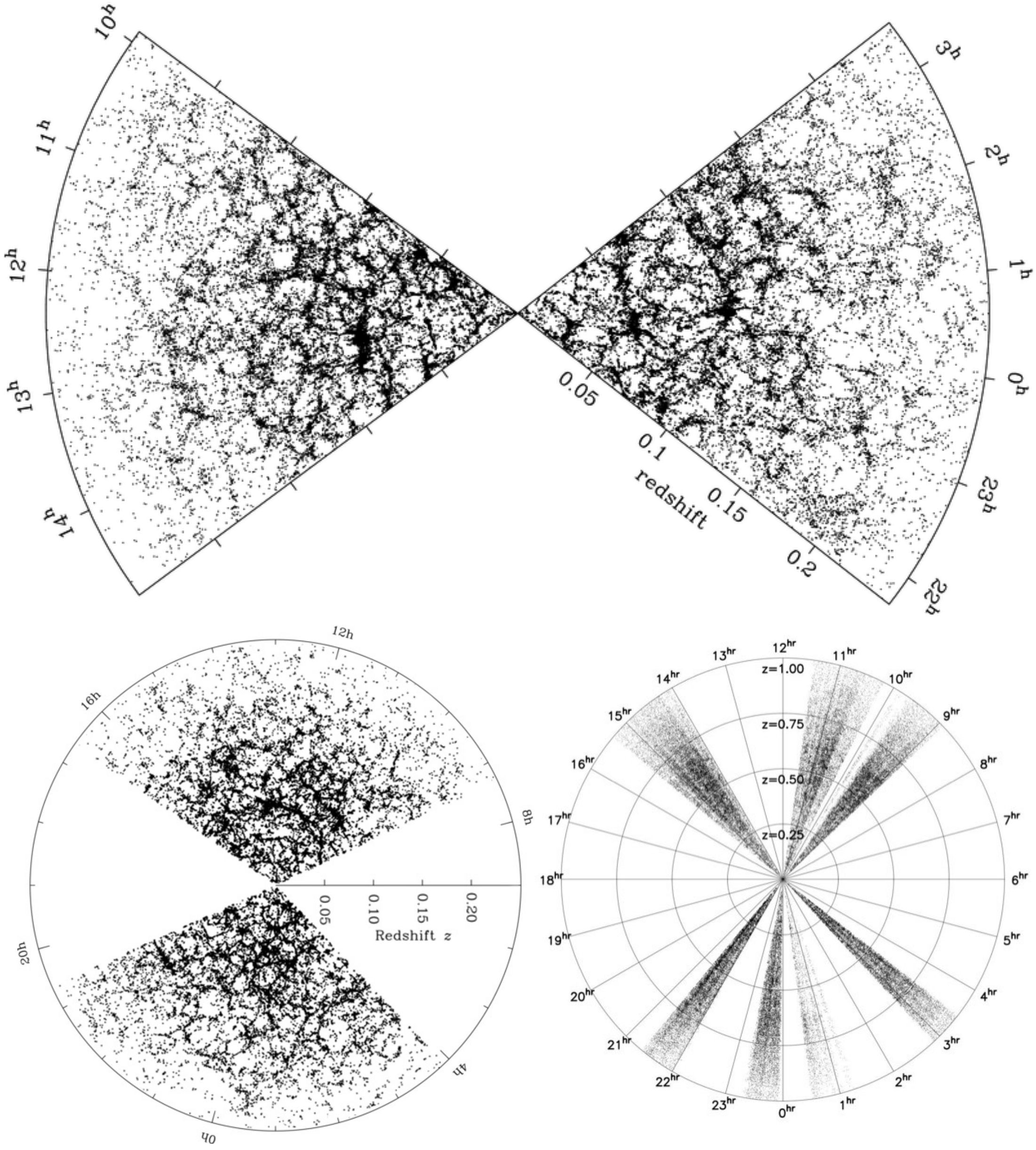

Figure 1.1: The large scale structure as observed with galaxy redshift surveys made by corresponding surveys. Top: 2dF galaxy redshift survey [1], Bottom left: Sloan Digital Sky Survey [2], Bottom right: WiggleZ Dark Energy Survey [3]. One can see the isotropic galaxy distribution on large scales.

1.2 Inhomogeneity and Cosmological Perturbations

On the other hand, inflation also predicts the emergence of the Gaussian quantum fluctuations, which become the seeds of large scale structures. This fact is indirectly confirmed by the CMB observation as well. On top of the full sky 2.73 K thermal radiation, a $\Delta T/T \sim 10^{-5}$ rms temperature anisotropy signal was detected by COBE with more than 7 σ [18] after dipole subtraction. This inhomogeneity of the early Universe has played an important role in the history of modern precision cosmology.

One way to describe the deviations from the isotropy and homogeneity of the Universe is perturbation theory. It considers a small perturbation $\delta g_{\mu\nu}$ around a background metric $\bar{g}_{\mu\nu}$, which is homogeneous and isotropic,

$$g_{\mu\nu} = \bar{g}_{\mu\nu} + \delta g_{\mu\nu} \ . \tag{1.1}$$

Then one can solve the Einstein equations with linear perturbations in an expanding background,

$$\bar{R}_{\mu\nu} + \delta R_{\mu\nu} - \frac{1}{2}\bar{R} g_{\mu\nu} - \frac{1}{2}\delta R \bar{g}_{\mu\nu} - \frac{1}{2}\bar{R}\delta g_{\mu\nu} = 8\pi G \bar{T}_{\mu\nu} + 8\pi G \delta T_{\mu\nu} \ . \tag{1.2}$$

One can rewrite this equation into two equations, one for the background and the other for the perturbations. This decomposition simplifies the calculation. However, one should keep in mind that this decomposition is correct only when the perturbations stay small enough during the evolution. For the small scale perturbations at late time, the linear perturbation theory breaks down. One has to rely on higher order perturbation theory or N-body simulations, dependent on the scale.

The pioneering work on perturbation theory in Friedmann-Lemaître-Robertson-Walker (FLRW) cosmological models was made by Lifshitz and Khalatnikov [19]. After that, the subject was studied by many authors.

This procedure sounds like a straightforward task. However, the interpretation has led to confusion for several years. The fact that not all perturbed metrics are physical, is not adequately addressed in some of the early papers. At that time most approaches pick simple coordinate conditions and keep track of physical modes and coordinate artifacts (also called gauge modes). Often simple coordinate conditions (gauge choices) do not fix the coordinates completely. For instance, the gauge transformation

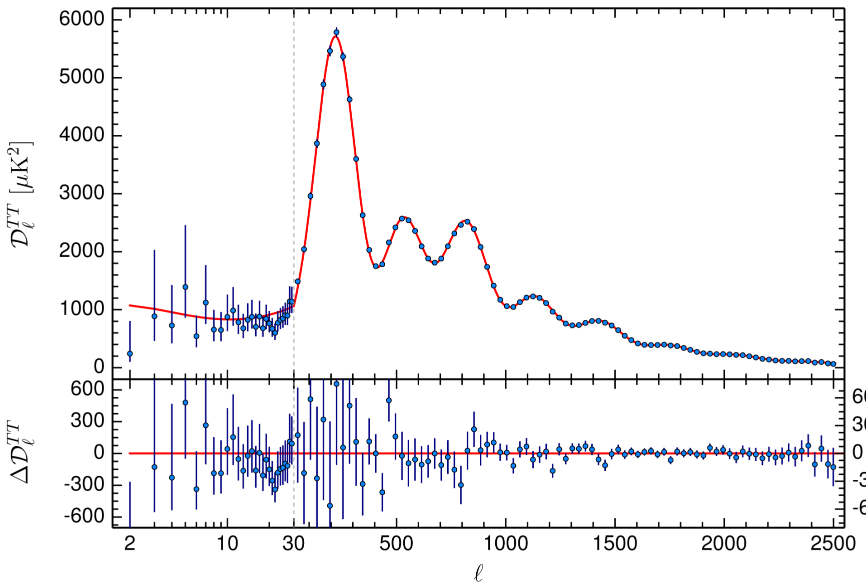

Figure 1.2: The CMB temperature anisotropy spectrum from Planck 2015 [4]. The red solid line shows the best fit ΛCDM model

of synchronous gauge contains two arbitrary integration constants, which will lead to unphysical gauge mode solutions for density perturbations outside the horizon.

A more elegant way to deal with this gauge issue is the gauge invariant approach in which one only focuses on the metric variables which are independent of the choice of coordinates. This approach eliminates the gauge dependence entirely rather than to just specify and understand it. Bardeen [20, 21] and Gerlach and Sengupta [22] made important work on this gauge-invariant approach to gravitational perturbations and cosmological perturbations. The gauge invariant approach will be discussed in more detail in chapter 2.

1.3 The Composition of the Universe

The motivation to study the large scale structure includes understanding the matter content of the Universe, testing general relativity on large scales and testing primordial Gaussianity. The measurement of the spatial anisotropy spectrum of the CMB temperature (see Fig. 1.2) suggested that our Universe consists of 68.3% dark energy and 26.8% dark matter [23]. Dark energy has been introduced as a component driving the accelerated expansion of the Universe and dark matter is a hypothetical matter which is only inferred from its gravitational effects. Both of them play important roles in the large scale structure formation, and they are two of the greatest mysteries in modern physics.

Many models attempt to explain observations without introducing dark energy. The most popular solution is modifying gravity at large scales. This involves another fundamental question, whether general relativity is the true theory for gravity. The study of the large scale structure can help us to break the degeneracy between modified gravity and dark energy.

One of the most well motivated ideas to understand dark energy is cosmological back reaction [24]. The standard cosmological perturbation theory always considers the evolution of the spatial average. However, the true observation is the spatial average of the evolved perturbations. Spatial average and time evolution do not commute, and the difference between the two cases can drive the expansion of the Universe. Due to the difficulty in averaging of tensors in curved spacetime, this issue is still open.

On the other hand, the investigations of the large scale structure contribute a lot in revealing the nature of dark matter. In the early 1980s, the hot dark matter model was popular, which consists of dark matter particles that have a free-streaming length much larger than a proto-galaxy. It has been ruled out latter, because hot dark matter washes out all small structures through free streaming. The hot dark matter model suggests that the super-clusters form first, which then fragment into galaxies. This is in conflict with deep field galaxy observations [25].

To verify those theories, one has to rely on a large amount of large scale structure observations to give tighter constraints on the evolution of perturbations and the expansion history.

1.4 History of Radio Cosmology

During 1960s and 1970s, people were very enthusiastic searching for the cosmological implications of the study of radio sources. In those early days, their reasons were quite clear [26]. First, radio emission is intense and can be observed of cosmological distances far beyond the reach of optical telescopes. Second, the radio sky background and foreground are relatively clean compared to the optical sky. Third, for Earth based

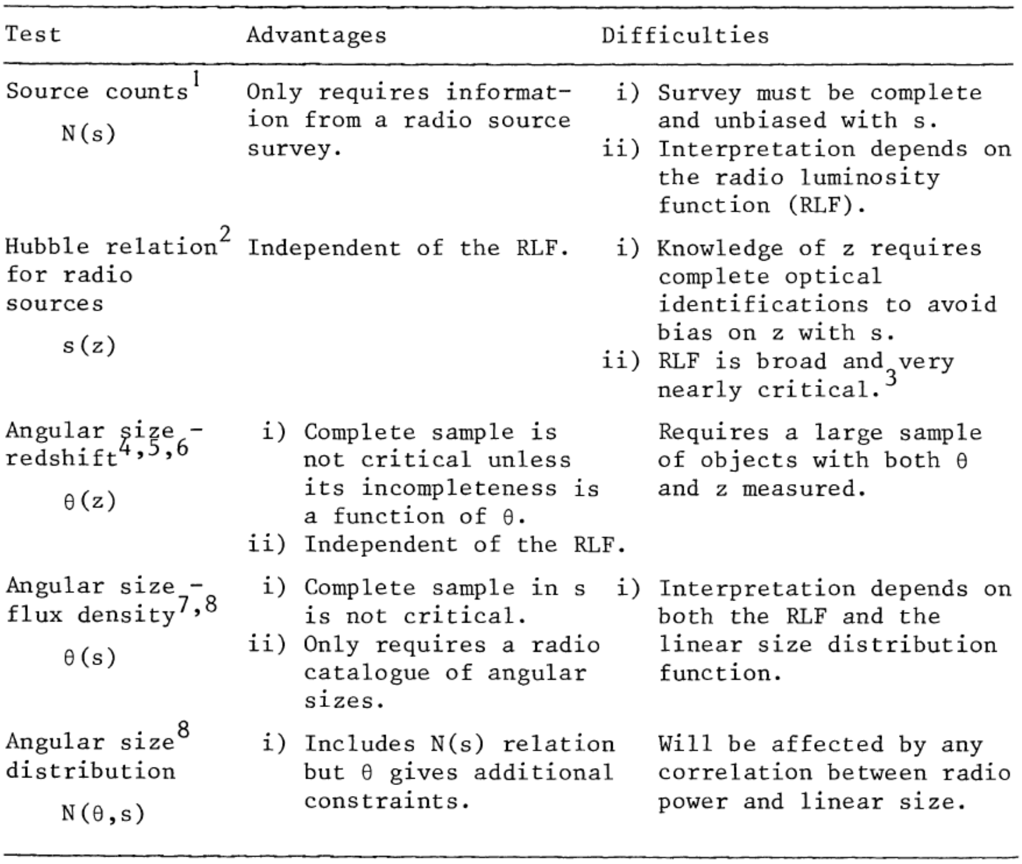

Test	Advantages	Difficulties
Source counts[1] N(s)	Only requires information from a radio source survey.	i) Survey must be complete and unbiased with s. ii) Interpretation depends on the radio luminosity function (RLF).
Hubble relation[2] for radio sources s(z)	Independent of the RLF.	i) Knowledge of z requires complete optical identifications to avoid bias on z with s. ii) RLF is broad and very nearly critical.[3]
Angular size - redshift[4,5,6] θ(z)	i) Complete sample is not critical unless its incompleteness is a function of θ. ii) Independent of the RLF.	Requires a large sample of objects with both θ and z measured.
Angular size - flux density[7,8] θ(s)	i) Complete sample in s is not critical. ii) Only requires a radio catalogue of angular sizes.	i) Interpretation depends on both the RLF and the linear size distribution function.
Angular size[8] distribution N(θ,s)	i) Includes N(s) relation but θ gives additional constraints.	Will be affected by any correlation between radio power and linear size.

Figure 1.3: Summary of main cosmological tests using radio sources as probes by Ekers and Miley in 1977 [5]

telescopes the transparency window in radio frequency is much wider than for optical frequencies. Forth, the galactic absorption of radio frequencies is negligible.

These advantages do not transform into significant contributions in cosmology after the discovery of the CMB. In 1977, Ekers and Miley summarized the main radio sources cosmological tests at that time, shown in Fig. 1.3. The first test faces the difficulty which arises from the lack of knowledge of the radio source origin and evolution. Thus, the radio luminosity function (RLF) is not well understood, which is still true today. The second test requires redshift information, which is hard to determine for the radio galaxies from radio observation alone. It is mainly because the lack of shape features in radio spectra (except for the 21cm hydrogen line).

The remaining three tests involving angular sizes of radio sources looked promising to learn about the geometry of the Universe in 1970s. It measures the angular separation of the radio components of double radio sources. Typical double radio sources associated with optical images are shown in Fig. 1.4. However this separation cannot be used as a standard rod, because the median angular separation of the source components is observed to be roughly inversely proportional to redshift [27]. There are many models that try to explain why the separation of the radio source components might be smaller in the past. For instance, the interstellar and intergalactic gas density was greater in the past such that the source components cannot travel so far [28].

Another version of the angular size test is using compact radio sources through Very Long Baseline Interferometry [7]. Since the compact sources are deeply embedded within the central regions of the host galaxy, they may be less affect by the intergalactic and interstellar medium. This angular diameter-redshift relation is shown in Fig. 1.5. They contradict suppernova measurements, as this result is consistent with a deceleration parameter today $q_0 = 0.5$.

These cosmological tests are very limited due to the degeneracy between the cosmological model and the evolution of radio galaxy. However, one can combine these measurements with the CMB and other cosmological observations to learn about the properties of radio galaxies [29].

1.5 Radio Cosmology after Planck

The CMB has been the main observational tool in cosmology for about three decades by now. It provides 2-dimensional information about the last scattering surface, which allows us to constrain cosmological parameters with unprecedented accuracy. Recently, the cosmological tests with CMB lensing have achieved a lot of success. The CMB lensing information has been measured precisely and gives additional information about the integrated gravitational potential along the line of sight [8].

Similar to the CMB lensing, radio galaxy continuum surveys can also give an integrated structure information along the line of sight. The current radio galaxy continuum surveys contain more than 10^6 galaxies with mean redshift around 0.5, and provide a natural platform for large scale structure research with considerable statistical advantages. However, it has not received sufficient attention in cosmology during the past years. The new generation of radio telescopes now under construction such as

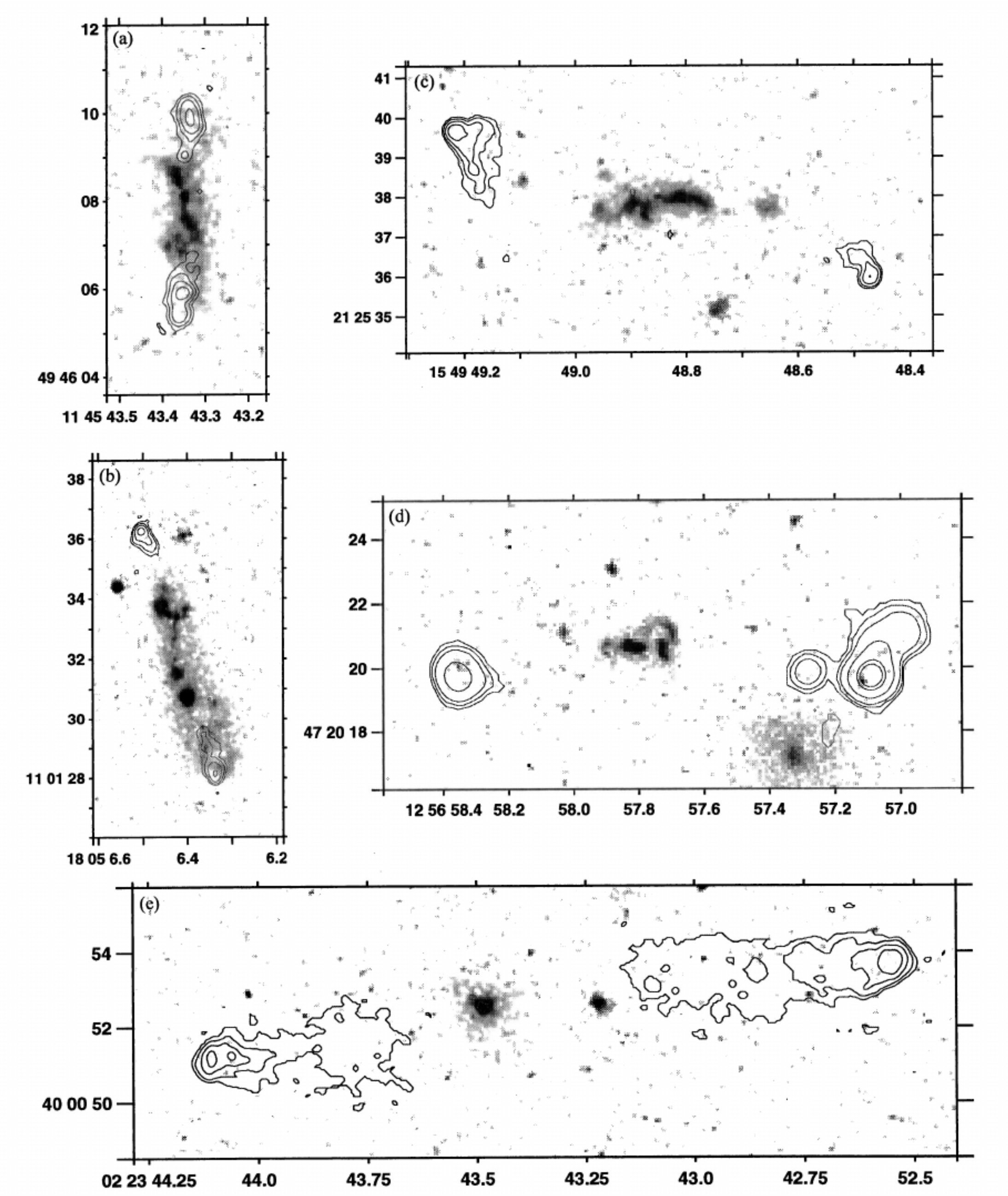

Figure 1.4: Hubble Space Telescope images of five 3CR radio galaxies with radio emission contours from the Cambridge four-element interferometer, from [6]. In order of increasing radio size (D): (a) 3C 266 (upper left, $z = 1.272$, $D = 39$ kpc); (b) 3C 368 (centre left, $z = 1.132$,$D = 73$ kpc); (c) 3C 324 (upper right, $z = 1.21$,$D = 96$ kpc); (d) 3C 280 (centre right, $z = 0.996$,$D = 117$ kpc); (e) 3C 65 (bottom, $z = 1.176$,$D = 155$ kpc).

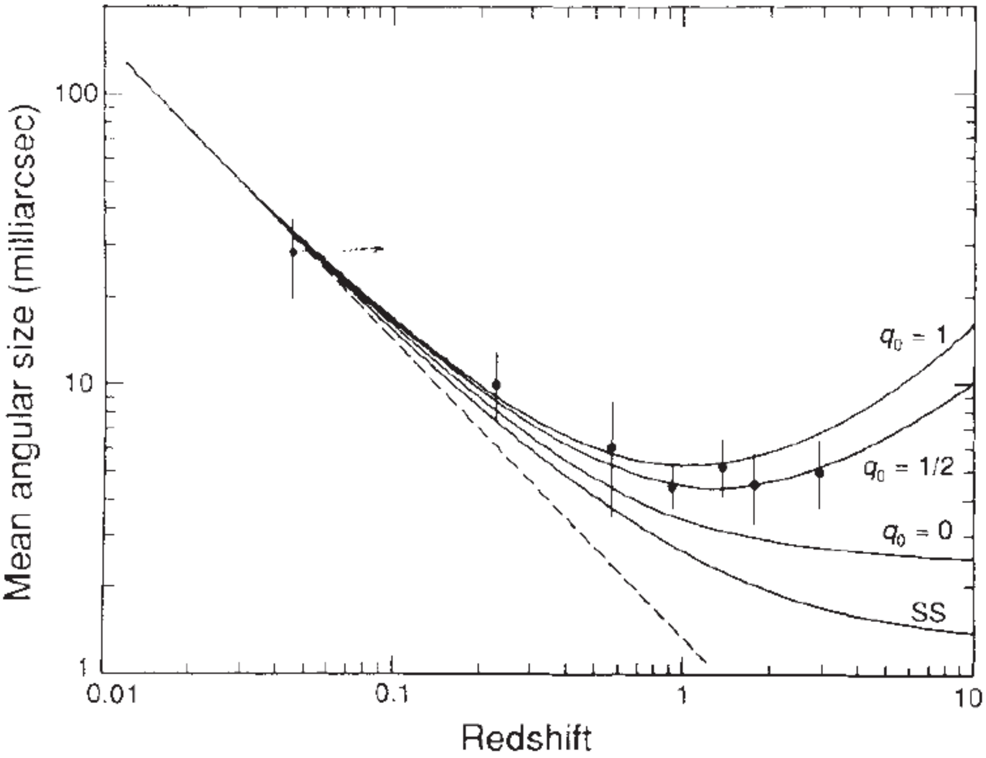

Figure 1.5: Mean angular size against redshift for 82 compact sources by Kellermann [7]. The solid curves represent the expected dependece for FLRW cosmological models for a standard source with a component separation of 41 parsec and deceleration parameter q_0 of 0, 1/2 and 1 and the steady-state model (SS); the dashed line shows the $1/z$ law observed for the separation of double-lobed extend sources.

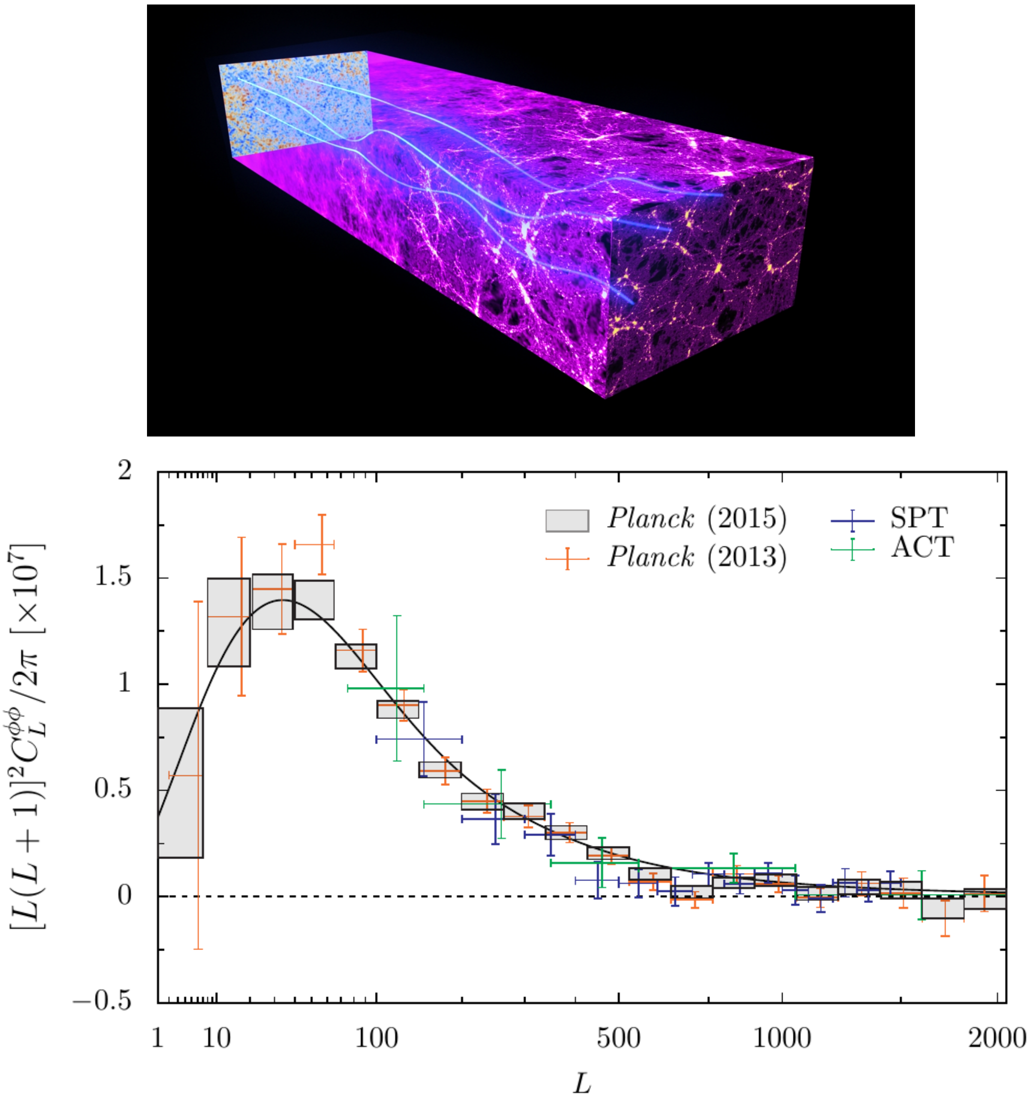

Figure 1.6: Top: The cartoon shows how the CMB photon trajectories are affected by the matter distribution between the receiver and the last scattering surface. Bottom: The gravitational lensing power spectrum of the cosmic microwave background from the Planck 2015 results [8]. (Made by ESA and the Planck Collaboration)

Low Frequency Array (LOFAR)[1], the Australian Square Kilometre Array Pathfinder (ASKAP)[2], MeerKAT[3] and Square Kilometre Array (SKA)[4], will provide even larger and deeper radio galaxy continuum surveys, capable of detecting galaxies above redshift 3. Those galaxies are roughly located in the middle of the last scattering surface and us, having the strongest lensing effect according to general relativity. Combining the CMB lensing and radio galaxies enables one to better test gravity and understand the structure evolution [30].

Moreover, the next generation of radio telescopes are capable to map the intensity of the 21cm line up to a redshift of 5. This will allow radio galaxy surveys to do precision cosmology alone. It can be a competitive way to probe the 3-dimensional large scale structure, which would bring precision cosmology to a new stage [31].

---

[1] URL: www.lofar.org

[2] URL: www.atnf.csiro.au/projects/askap/

[3] URL: www.ska.ac.za/meerkat/

[4] URL: www.skatelescope.org

Chapter 2

Perturbation Theory and Galaxy Number Counts

2.1 Metric Perturbations

The real universe is not perfectly homogeneous. The inhomogeneities in the matter distribution induce metric perturbations, which can be decomposed into irreducible components, based on the symmetry properties with respect to spatial rotations and translations. More precisely the metric perturbations $\delta g_{\mu\nu}$ can be categorized into three distinct types: scalar mode perturbations, vector mode perturbations and tensor mode perturbations. At the linear order different types of perturbation evolve independently and can thus be investigated separately. In this thesis, we consider linear perturbations of a spatially isotropic, homogeneous and flat metric, largely following the notation of [32]. The line element is expressed as

$$\begin{aligned} \mathrm{d}s^2 \quad = \quad & -a^2(1+2\phi)\mathrm{d}\eta^2 - 2a^2(B_{,i}+S_i)\mathrm{d}\eta\mathrm{d}x^i \\ & +a^2[(1+2\psi)\delta_{ij} + 2E_{,ij} + F_{i,j} + F_{j,i} + h_{ij}]\mathrm{d}x^i\mathrm{d}x^j, \end{aligned} \tag{2.1}$$

where a is the scale factor, $B_{,i} = \partial B/\partial x^i$, and S_i and F_i are transverse vectors, i.e. their divergencies vanish ($S^i_{,i} = 0$ and $F^i_{,i} = 0$). The transverse, traceless tensor h_{ij} satisfies the four constraints $h^i_i = 0, h^i_{j,i} = 0$.

The scalar mode perturbations contain four metric components ϕ, ψ, B, E, which play an important role in the structure formation. The vector mode perturbations

S_i and F_i describe the rotational motion of the fluid, which decays fast as the universe expands. The tensor mode perturbation h_{ij} corresponds to the propagation of gravitational waves.

As we discussed in the introduction, when the metric is perturbed, it is not trivial to distinguish physical modes from the gauge modes which arise purely from the choice of a coordinate system. In other words, the decomposition of the metric into a background plus a perturbation is not unique [33].

There are two equivalent methods to describe the gauge transformations of these perturbations, one is to consider them as passive coordinate transformations (also see [32]), the other is to view them as active diffeomorphism (also see [33]), both will be explained in the following sections.

2.1.1 Method I : Passive Coordinate Transformations

In the passive coordinate transformation method, the metric perturbation is defined as the difference between the physical metric and the background metric at the same physical point

$$\delta g_{\mu\nu}(x) = g_{\mu\nu}(x) - \bar{g}_{\mu\nu}(x) \quad . \tag{2.2}$$

Let us consider the infinitesimal coordinate transformation

$$x^\mu \to \tilde{x}^\mu = x^\mu + \xi^\mu \quad . \tag{2.3}$$

At a given point in space-time, the metric transforms following the tensor transformation law

$$\begin{aligned} \tilde{g}_{\mu\nu}(\tilde{x}) &= \frac{\partial x^\gamma}{\partial \tilde{x}^\mu}\frac{\partial x^\sigma}{\partial \tilde{x}^\nu} g_{\gamma\sigma}(x) \\ &\approx \bar{g}_{\mu\nu}(x) + \delta g_{\mu\nu}(x) - \bar{g}_{\mu\sigma}\xi^\sigma_{,\nu} - \bar{g}_{\gamma\nu}\xi^\gamma_{,\mu} \quad . \end{aligned} \tag{2.4}$$

After splitting the metric into background and perturbation in the new coordinate $\tilde{x}$, one obtains

$$\delta\tilde{g}_{\mu\nu}(\tilde{x}) = \delta g_{\mu\nu}(x) + \bar{g}_{\mu\nu}(x) - \bar{g}_{\mu\nu}(\tilde{x}) - \bar{g}_{\mu\sigma}\xi^\sigma_{,\nu} - \bar{g}_{\gamma\nu}\xi^\gamma_{,\mu} \quad . \tag{2.5}$$

Since

$$\bar{g}_{\mu\nu}(\tilde{x}) \approx \bar{g}_{\mu\nu}(x) + \bar{g}_{\mu\nu,\rho}(x)\xi^\rho \quad , \tag{2.6}$$

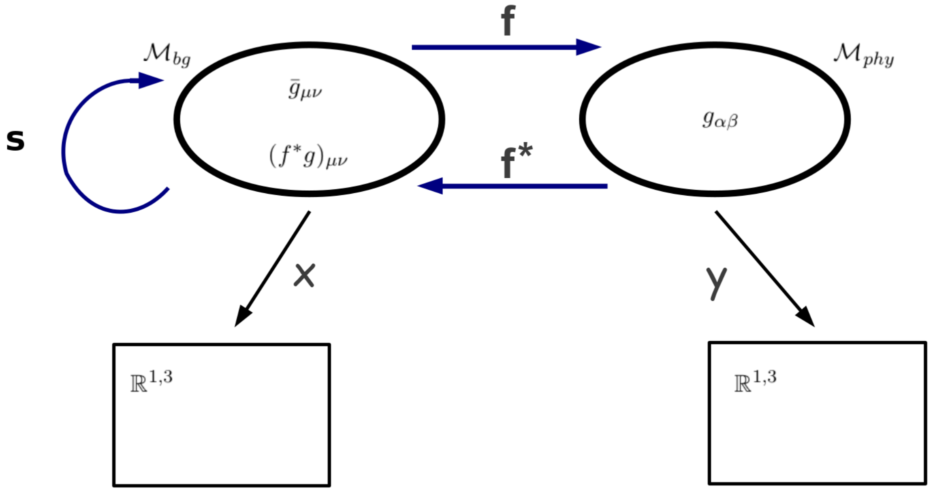

Figure 2.1: Diffeomorphism related background spacetime and physical spacetime

we rederive the metric perturbation gauge transformation law as

$$\begin{aligned} \delta\tilde{g}_{\mu\nu}(\tilde{x}) &= \delta g_{\mu\nu}(x) - \bar{g}_{\mu\nu,\rho}(x)\xi^{\rho} - \bar{g}_{\mu\sigma}\xi^{\sigma}_{,\nu} - \bar{g}_{\gamma\nu}\xi^{\gamma}_{,\mu} \\ &= \delta g_{\mu\nu}(x) - \nabla_{\mu}\xi_{\nu} - \nabla_{\nu}\xi_{\mu} \quad , \end{aligned} \tag{2.7}$$

where ∇_μ is the covariant derivative.

2.1.2 Method II: Active Diffeomorphisms

In this method, the linear perturbation theory can be considered as three parts: a background spacetime M_{bg}, a physical spacetime M_{phy} and a diffeomorphism $f : M_{\text{bg}} \to M_{\text{phy}}$, which states that the map between the two manifolds is invertible. One can imagine that the manifolds M_{bg} and M_{phy} are essentially the same, but possess different metrics. We use a flat FLRW metric $\bar{g}_{\mu\nu}$ on the M_{bg} and on M_{phy} we have some general metric $g_{\alpha\beta}$. We could also say that M_{bg} is equipped with coordinates x^μ and M_{phy} equipped with coordinates y^α. The diffeomorphism f allows us to move the metrics back and forth between the background and physical space-times, as shown in Fig. 2.1.

For simplicity we construct the linear perturbation theory on the background spacetime and pull back $g_{\alpha\beta}$ to $M_{\rm bg}$. The perturbation is defined as the difference between the background metric $\bar{g}_{\mu\nu}$ and the pullback metric $(f^*g)_{\mu\nu}$, where f^* can be thought as pulling back through f,

$$\delta g_{\mu\nu} = (f^*g)_{\mu\nu} - \bar{g}_{\mu\nu} \ . \tag{2.8}$$

Thus the metric in Eq. (2.1) actually is the constructed pullback metric. With this construction the components of metric perturbation $\delta g_{\mu\nu}$ are not necessary small. We have to limit our choices to diffeomorphisms for which $\delta g_{\mu\nu}$ is small enough. Even with this constraint, there is still a large number of allowed diffeomorphisms between the two spacetimes. To show that, one simply assigns an infinitesimal vector field on the background spacetime. This vector field generates a diffeomorphism $s : M_{\rm bg} \to M_{\rm bg}$, as shown in Fig. 2.1. If a diffeomorphism f fulfills the constraint, then so does $f \circ s$, where $\circ$ denotes the composition of two maps. The new metric perturbation becomes

$$\begin{aligned} \delta\tilde{g}_{\mu\nu} &= [(f\circ s)^* g]_{\mu\nu} - \bar{g}_{\mu\nu} \\ &= [s^*(f^*g)]_{\mu\nu} - \bar{g}_{\mu\nu} \\ &= s^*(\bar{g} + \delta g)_{\mu\nu} - \bar{g}_{\mu\nu} \\ &= s^*(\bar{g}_{\mu\nu}) + s^*(\delta g_{\mu\nu}) - \bar{g}_{\mu\nu} \\ &\approx \delta g_{\mu\nu} + \mathcal{L}_\xi \bar{g}_{\mu\nu} \ , \end{aligned} \tag{2.9}$$

where in the last line we used the approximation $s^*(\delta g_{\mu\nu}) \approx \delta g_{\mu\nu}$, while the remaining two terms $s^*(\bar{g}_{\mu\nu}) - \bar{g}_{\mu\nu}$ yield $\mathcal{L}_\xi \bar{g}_{\mu\nu} = 2\nabla_{(\mu}\xi_{\nu)}$, a Lie derivative of the background metric along the infinitesimal vector field ξ_μ. Thus one gets the gauge transformation law in linearized theory,

$$\delta\tilde{g}_{\mu\nu} = \delta g_{\mu\nu} + \nabla_\mu\xi_\nu + \nabla_\nu\xi_\mu \tag{2.10}$$

The above formula is the same as the one derived from a passive coordinate transformation, up to a change of sign of ξ^μ. Our following calculation uses the gauge transformation law in passive coordinate transformation convention (see Eq. (2.7)).

2.2 Gauge-invariant Metric Potentials

In a FLRW universe with a metric as in Eq. (2.1), there are in total 10 degrees of freedom, and not all of them are physical. Using the gauge transformation law Eq. (2.7), we obtain

$$\begin{aligned} &\phi \to \tilde{\phi} = \phi - \mathcal{H}\xi^0 - \dot{\xi}^0 \ , && B \to \tilde{B} = B + \dot{\zeta} - \xi^0 \ , \\ &\psi \to \tilde{\psi} = \psi - \mathcal{H}\xi^0 \ , && E \to \tilde{E} = E - \zeta \ , \\ &S_i \to \tilde{S}_i = S_i + \dot{\xi}_{\perp i} \ , && F_i \to \tilde{F}_i = F_i - \xi_{\perp i}, \end{aligned}$$

where $\xi^\mu \equiv (\xi^0, \xi^i)$ and $\xi^i = \xi^i_\perp + \zeta^{,i}$. A dot denotes a derivative with respect to the conformal time η and $\mathcal{H} \equiv \dot{a}/a$. By choosing ξ^μ appropriately, we can eliminate 4 coordinate degrees of freedom or we can construct gauge invariant metric potentials:

$$\Phi \equiv \phi - \mathcal{H}(B + \dot{E}) - (\dot{B} + \ddot{E}) \ , \tag{2.11}$$

$$\Psi \equiv \psi - \mathcal{H}(B + \dot{E}) \ , \tag{2.12}$$

$$U_i \equiv S_i + \dot{F}_i \ . \tag{2.13}$$

They do not change under the coordinate transformations, and correspond to real physical inhomogeneities.

2.3 Galaxy Number Counts I

We can consider our past light cone to be a three-dimensional hypersurface of the four-dimensional space-time. Within this hypersurface, the four coordinates x^μ may be expressed by smooth functions of three parameters. For convenience we use the light cone constraint to fix the conformal time η, and choose the three parameters on the past light cone to be the spherical coordinates (r, θ, ϕ). In a second step (next section) we connect them to the observed source positions on the sky and to observed comoving source distances.

The total number of galaxies on the past light cone (plc) can be computed by considering a covariant hypersurface integral [34]

$$N = \int_{\mathrm{plc}} n_{\mathrm{phy}} u^\mu \mathrm{d}S_\mu, \tag{2.14}$$

where $n_{\mathrm{phy}} = n_{\mathrm{phy}}(\eta, x^i)$ is the inhomogeneous physical number density, $u^0 = (1 - \phi)/a, u^i = v^i/a$ are the components of the four-velocity field of galaxies and

$$\begin{aligned} \mathrm{d}S_\mu &= \epsilon_{\mu\nu\sigma\rho}\mathrm{d}x^\nu \mathrm{d}x^\sigma \mathrm{d}x^\rho \\ &= \epsilon_{\mu\nu\sigma\rho}\frac{\partial x^\nu}{\partial r}\frac{\partial x^\sigma}{\partial \theta}\frac{\partial x^\rho}{\partial \varphi}\mathrm{d}r\mathrm{d}\theta\mathrm{d}\varphi, \end{aligned} \tag{2.15}$$

with $\epsilon_{\mu\nu\sigma\rho} = \sqrt{-g}[\mu\,\nu\,\sigma\,\rho]$ denoting the Levi-Civita pseudo-tensor.

At linear order, the covariant volume integral can be written as

$$\begin{aligned} N &= \int_{\text{plc}} n_{\text{phy}} u^{\mu} \epsilon_{\mu\nu\sigma\rho} \frac{\partial x^{\nu}}{\partial r} \frac{\partial x^{\sigma}}{\partial \theta} \frac{\partial x^{\rho}}{\partial \varphi} \mathrm{d}r \mathrm{d}\theta \mathrm{d}\varphi \\ &= \int_{\text{plc}} n_{\text{phy}} a^3 r^2 [1 + 3\psi + \nabla^2 E + v^i e_i^r] \mathrm{d}r \mathrm{d}\Omega, \end{aligned} \tag{2.16}$$

where e_i^r denotes the radial unit vector. Here, the terms 3ψ and $\nabla^2 E$ are due to the distortion of the spatial volume, the term $v^i e_i^r$ is due to the light cone projection. Let us stress that this result holds true for all coordinate systems in which the observer is at rest, i.e. v^i denote the velocity of the sources. In order to express N in another frame (e.g. the CMB rest frame) one has to replace v^i by $(v^i - v_o^i)$, where v_o^i denotes the observer's peculiar velocity. This can be easily seen from the fact that linearized Lorentz boosts reduce to Galilean transformations which do not modify the volume, but affect the light cone projection. By construction N is a gauge invariant quantity, which we have checked explicitly.

2.4 Coordinates of the Observer

In the previous section, the number count has been expressed as an integral over the coordinates (r, θ, φ). However, these coordinates do not agree with the coordinates used by the observer. The actual observables are redshift and/or flux, instead of coordinate distance, and position (two observed angles), instead of the angular coordinates introduced above. The following subsection briefly reviews the redshift and luminosity distance distortions up to first order in cosmological perturbations.

2.4.1 Conformal Transformation

Conformal transformations preserve the causal structure of space-time. Thus we can find the null geodesics of a linearly perturbed Minkowski space-time and relate them to the null-geodesics of the spatially flat Friedmann-Lemaître-Robertson-Walker cosmologies via a conformal transformation provided by the scale factor. This strategy was used in [35, 36, 37].

For completeness, we repeat the most essential steps of the proof in our notation following [38].

We consider a conformal transformation

$$g_{\mu\nu} \to \hat{g}_{\mu\nu} = \Omega^2 g_{\mu\nu} \quad . \tag{2.17}$$

From now on ˆ denote the objects in conformal related geometry. We denote ∇_μ to be the covariant derivative operator associated with $g_{\mu\nu}$, and $\hat{\nabla}_\mu$ to be associated with $\hat{g}_{\mu\nu}$. The relation between $\hat{\nabla}_\mu$ and ∇_μ is given by

$$\hat{\nabla}_\mu w_\nu = \nabla_\mu w_\nu - C^\gamma_{\mu\nu} w_\gamma \quad , \tag{2.18}$$

where $C^\gamma_{\mu\nu}$ is a smooth tensor field which satisfies $C^\gamma_{\mu\nu} = C^\gamma_{\nu\mu}$. It becomes the Christoffel symbol, when ∇_μ is an ordinary partial derivative operator. Using the symmetry property of $C^\gamma_{\mu\nu}$ and metric compatibility, we obtain

$$C^\gamma_{\mu\nu} = \frac{1}{2}\hat{g}^{\gamma\rho}(\nabla_\mu \hat{g}_{\nu\rho} + \nabla_\nu \hat{g}_{\mu\rho} - \nabla_\rho \hat{g}_{\mu\nu}) \tag{2.19}$$

Since $\nabla_\mu g_{\nu\gamma} = 0$, we get

$$C^\gamma_{\mu\nu} = \delta^\gamma_\mu \nabla_\nu \ln\Omega + \delta^\gamma_\nu \nabla_\mu \ln\Omega - g_{\mu\nu} g^{\gamma\rho} \nabla_\rho \ln\Omega \quad . \tag{2.20}$$

We use $C^\gamma_{\mu\nu}$ to compare the geodesics with respect to different metrics. Assuming V^μ is the tangent vector to an affinely parametrized geodesic, then

$$V^\mu \nabla_\mu V^\nu = 0 \quad , \tag{2.21}$$

and thus

$$V^\mu \hat{\nabla}_\mu V^\nu = 2V^\nu V^\gamma \nabla_\gamma \ln\Omega - (g_{\mu\gamma} V^\mu V^\gamma) g^{\nu\rho} \nabla_\rho \ln\Omega \quad . \tag{2.22}$$

In the case of null geodesics the second term vanishes, and this equation becomes the non-affine parametrized geodesic equation. The affine parameter $\hat{\lambda}$ for $\hat{\nabla}_\mu$ is related to the original affine parameter λ by

$$\frac{\mathrm{d}\hat{\lambda}}{\mathrm{d}\lambda} = c\Omega^2 \quad , \tag{2.23}$$

where c is a constant. Thus, we can conclude that null geodesics are conformally invariant. In the following section, perturbations are first evaluated in a perturbed Minkowski space-time and then conformally related to the physical space-time.

2.4.2 Redshift Distortions

Now, we consider a conformal transformation

$$g_{\mu\nu} \to \hat{g}_{\mu\nu} = a^2 g_{\mu\nu} \quad . \tag{2.24}$$

The physical redshift is defined as

$$z = \frac{\omega_{\rm s}}{\omega_{\rm o}} - 1 = \frac{(\hat{u}_\mu \hat{k}^\mu)_{\rm s}}{(\hat{u}_\nu \hat{k}^\nu)_{\rm o}} - 1 \quad , \tag{2.25}$$

where $\omega_{\rm s}$ and $\omega_{\rm o}$ are the frequencies at the source and observer, respectively. $\hat{k}^\mu$ and k^μ are the light-like wave vectors associated with $\hat{g}_{\mu\nu}$ and $g_{\mu\nu}$. $\hat{u}^\mu$ and u^μ are the 4-velocities associated with $\hat{g}_{\mu\nu}$ and $g_{\mu\nu}$.

Using Eq. 2.23 and $\mathrm{d}\hat{s}^2 = a^2 \mathrm{d}s^2$, we obtain $\hat{k}^\mu = k^\mu / a^2$. Since $\hat{u}^\mu$ is time-like 4-velocity $\hat{u}^\mu = \mathrm{d}x^\mu / d\hat{\tau}$, we get $\hat{u}^\mu = u^\mu / a$.

Thus

$$z = \frac{a_{\rm o}(u_\mu k^\mu)_{\rm s}}{a_{\rm s}(u_\nu k^\nu)_{\rm o}} - 1 \quad . \tag{2.26}$$

The null geodesic $x^\mu(\lambda)$, with λ denoting an affine parameter, can be decomposed into a background path plus a perturbation,

$$x^\mu(\lambda) = x^{(0)\mu}(\lambda) + x^{(1)\mu}(\lambda), \tag{2.27}$$

where $x^{(0)\mu}$ is a null geodesic in Minkowski space-time, and we assume that the metric perturbations are small. The lightlike wave vector is therefore

$$k^\mu = \frac{\mathrm{d}x^{(0)\mu}}{\mathrm{d}\lambda}, \quad l^\mu = \frac{\mathrm{d}x^{(1)\mu}}{\mathrm{d}\lambda}. \tag{2.28}$$

At first order, the null condition becomes

$$\begin{aligned} -k^0 l^0 + k^i l^i = {} & k^2 \phi + (B_{,i} + S_i) k^i k^0 \\ & - k^i k^j (\psi \delta_{ij} + E_{,ij} + \frac{1}{2} F_{i,j} + \frac{1}{2} F_{j,i} + \frac{1}{2} h_{ij}), \end{aligned} \tag{2.29}$$

where we define $(k^0)^2 = (k^i e_i)^2 \equiv k^2$.

Now we turn to the perturbed geodesic equation. The zeroth order geodesic equation simply tells us that $x^{(0)\mu}$ is a straight trajectory, while the first order geodesic equation is

$$\frac{\mathrm{d}l^\mu}{\mathrm{d}\lambda} = -2\Gamma^{(0)\mu}_{\rho\sigma} k^\rho l^\sigma - \Gamma^{(1)\mu}_{\rho\sigma} k^\rho k^\sigma - \Gamma^{(0)\mu}_{\rho\sigma,\nu} k^\rho k^\sigma x^{(1)\nu}. \tag{2.30}$$

For the flat background,

$$\frac{\mathrm{d}l^\mu}{\mathrm{d}\lambda} = -\Gamma^{(1)\mu}_{\rho\sigma} k^\rho k^\sigma . \tag{2.31}$$

The temporal component of this equation is

$$\begin{aligned}\frac{\mathrm{d}l^0}{\mathrm{d}\lambda} &= -2\frac{\mathrm{d}\phi}{\mathrm{d}\lambda}k^0 + k^2[\dot\phi - \dot\psi] - k^i k^j [\dot E_{,ij} + B_{,ij} \\ &\quad + \frac{1}{2}(S_{i,j} + S_{j,i} + \dot F_{i,j} + \dot F_{j,i}) + \frac{1}{2}\dot h_{ij}],\end{aligned} \tag{2.32}$$

where we used $\mathrm{d}\phi/\mathrm{d}\lambda = \dot\phi \mathrm{d}\eta/\mathrm{d}\lambda + \phi_{,i}\mathrm{d}x^i/\mathrm{d}\lambda$.

After integrating Eq. (2.32), we obtain the temporal component of the wave number perturbation

$$\begin{aligned}l^0|^{\mathrm{s}}_{\mathrm{o}} &= -2k^0\phi|^{\mathrm{s}}_{\mathrm{o}} + k^2\int_{\lambda_{\mathrm{o}}}^{\lambda_{\mathrm{s}}} \mathrm{d}\lambda'[\dot\phi - \dot\psi] - k^2\int_{\lambda_{\mathrm{o}}}^{\lambda_{\mathrm{s}}} \mathrm{d}\lambda' e^{ri}e^{rj}[\dot E_{,ij} \\ &\quad + B_{,ij} + \frac{1}{2}(S_{i,j} + S_{j,i} + \dot F_{i,j} + \dot F_{j,i} + \dot h_{ij})],\end{aligned} \tag{2.33}$$

where e^{ri} denotes the unit vector pointing from the observer to the source. With l^0 one can further evaluate the redshift at linear order, by means of

$$1 + z = \frac{a_{\mathrm{o}}}{a_{\mathrm{s}}}\,\frac{(k\cdot u^{(0)})_{\mathrm{s}} + (k\cdot u^{(1)})_{\mathrm{s}} + (l\cdot u^{(0)})_{\mathrm{s}}}{(k\cdot u^{(0)})_{\mathrm{o}} + (k\cdot u^{(1)})_{\mathrm{o}} + (l\cdot u^{(0)})_{\mathrm{o}}}. \tag{2.34}$$

Since u^i is of first order, only the time component of l^μ contributes and we find

$$\begin{aligned}1 + z &= \frac{\mathcal{A}_{\mathrm{o}}}{\mathcal{A}_{\mathrm{s}}}[1 - \Phi|^{\mathrm{s}}_{\mathrm{o}} + e^{ri}V_i|^{\mathrm{s}}_{\mathrm{o}} + k^0\int_{\lambda_{\mathrm{o}}}^{\lambda_{\mathrm{s}}}\mathrm{d}\lambda'(\dot\Phi - \dot\Psi) \\ &\quad - \frac{1}{2}k^0\int_{\lambda_{\mathrm{o}}}^{\lambda_{\mathrm{s}}}\mathrm{d}\lambda' e^{ri}e^{rj}(U_{i,j} + U_{j,i} + \dot h_{ij})],\end{aligned} \tag{2.35}$$

with the gauge invariant ratio of scale factors $\frac{\mathcal{A}_{\mathrm{o}}}{\mathcal{A}_{\mathrm{s}}} \equiv \frac{a_{\mathrm{o}}}{a_{\mathrm{s}}}(1 - \mathcal{H}(B + \dot E)|^{\mathrm{s}}_{\mathrm{o}})$ and the gauge invariant velocity $V_i \equiv v_i - S_i + \dot E_{,i}$. Thus this expression is manifestly gauge invariant. The affine parameter λ is related to conformal time via $\mathrm{d}\eta = k^0\mathrm{d}\lambda$. Our sign convention and the notation is illustrated in Fig. 2.3.

For convenience, we define $1 + z \equiv \frac{a_{\mathrm{o}}}{a_{\mathrm{s}}}(1 + \delta z)$, and thus the gauge dependent redshift distortion becomes

$$\begin{aligned}\delta z &= -\mathcal{H}(B + \dot E)|^{\mathrm{s}}_{\mathrm{o}} - \Phi|^{\mathrm{s}}_{\mathrm{o}} + e^{ri}V_i|^{\mathrm{s}}_{\mathrm{o}} + k^0\int_{\lambda_{\mathrm{o}}}^{\lambda_{\mathrm{s}}}\mathrm{d}\lambda'(\dot\Phi - \dot\Psi) \\ &\quad - \frac{1}{2}k^0\int_{\lambda_{\mathrm{o}}}^{\lambda_{\mathrm{s}}}\mathrm{d}\lambda' e^{ri}e^{rj}(U_{i,j} + U_{j,i} + \dot h_{ij}).\end{aligned} \tag{2.36}$$

From this equation, one can clearly see the well-known gravitational redshift, the Doppler shift and the integrated Sachs-Wolfe effect, as well as vector mode and gravitational wave contributions. A gauge-invariant redshift perturbation can be define as

$$1+z=\frac{\mathcal{A}_{\rm o}}{\mathcal{A}_{\rm s}}(1+\delta Z)\ \ ,\ \ \delta Z=\delta z+\mathcal{H}(B+\dot{E})|_{\rm o}^{\rm s} \tag{2.37}$$

We also introduce the notation $1+\bar{z}\equiv\frac{a_{\rm o}}{a_{\rm s}}$ to indicate the unperturbed redshift, which will be used later.

2.4.3 Specific Flux Fluctuations

Radio sources typically have featureless (power law) spectra, see Fig. 2.2. Their redshift cannot be obtained from radio continuum observations. However, we observe the specific flux. The observed specific flux of a radio source is also affected by metric fluctuations. This effect modifies any distance estimate based on the ratio of specific fluxes (assuming for a moment that we would know the specific luminosities).

The energy momentum tensor of monochromatic photons with frequency ω and 4-wave vector $\hat{k}^\mu$ is [39, 40]

$$T^{\mu\nu}=\frac{1}{8\pi}\mathscr{A}^2(\omega,\lambda)\hat{k}^\mu\hat{k}^\nu, \tag{2.38}$$

where $\mathscr{A}$ is the amplitude in the eikonal approximation of geometric optics. Here, we use $\hat{k}^\mu$ to distinguish the physical wave vector from k^μ, the wave vector in the conformally related Minkowski space-time.

The specific flux is given by a projection of the energy-momentum,

$$S\equiv-e_\alpha u_{\rm o}^\nu T^\mu_\nu h^\alpha_\mu, \tag{2.39}$$

where h^α_μ is the spatial projection tensor, orthogonal to the observer four-velocity $u_{\rm o}^\nu$, and e_α is a unit space like vector pointing in the direction of the 3 wave vector in the observer rest frame. These vectors are defined at the observer, and we parallel transport the wave vector and energy-momentum tensor along the geodesic. We find the specific flux density is

$$S(\omega)=\frac{1}{8\pi}\mathscr{A}^2(\omega,\lambda)\omega^2. \tag{2.40}$$

The emitted photon number in a frequency band of width $d\omega_{\rm s}$, solid angle $d\Omega_{\rm s}$, and proper time interval $d\tau_{\rm s}$ can be expressed in terms of the specific luminosity of a source

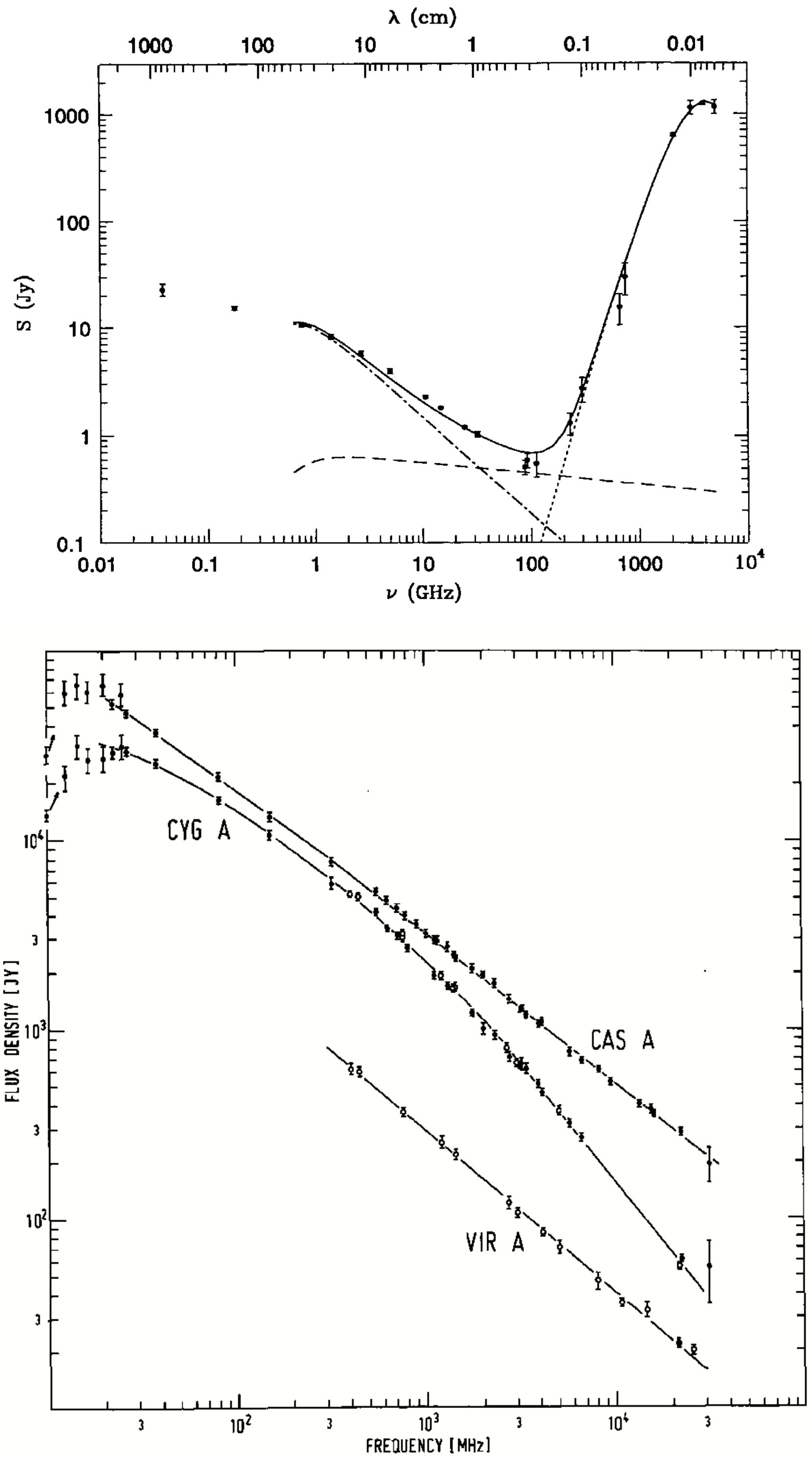

Figure 2.2: Radio galaxy spectrum. Top: FIR and radio spectrum of M82 (Condon, J. J. 1992, ARA&A, 30, 575); Bottom: radio spectrum of Cygnus A, Cassiopeia A and Virgo A (Baars, J. W. M. et al. 1977, A&A, 61, 99.)

$L(\omega_{\rm s}) \equiv 4\pi R_{\rm s}^2 S_{\rm s}(\omega_{\rm s})$ ($R_{\rm s}$ is a distance not too far from the center of the source) and reads

$$\mathrm{dN}_\gamma = \frac{\mathrm{L}(\omega_{\rm s})}{4\pi\omega_{\rm s}}\mathrm{d}\omega_{\rm s}\mathrm{d}\Omega_{\rm s}\mathrm{d}\tau_{\rm s}. \tag{2.41}$$

Due to the conservation of photon number (neglecting absorption and emission along the line of sight to a source) we can relate that to the observed specific flux density [41],

$$\frac{L(\omega_{\rm s})}{4\pi\omega_{\rm s}}\mathrm{d}\omega_{\rm s}\mathrm{d}\Omega_{\rm s}\mathrm{d}\tau_{\rm s} = \frac{S_{\rm o}(\omega_{\rm o})}{\omega_{\rm o}}\mathrm{d}\omega_{\rm o}\mathrm{d}A_{\rm o}\mathrm{d}\tau_{\rm o}, \tag{2.42}$$

where $\mathrm{d}A_{\rm o}$ is the photons passed area which orthogonal to the ray direction in an observer's 3-space.

The (monochromatic) luminosity distance $D_{\rm L}$ is

$$D_L \equiv \sqrt{\frac{L_{\rm s}(\omega_{\rm s})\mathrm{d}\omega_{\rm s}}{4\pi S_{\rm o}(\omega_{\rm o})\mathrm{d}\omega_{\rm o}}} = \frac{\mathscr{A}_{\rm s}\omega_{\rm s}}{\mathscr{A}_{\rm o}\omega_{\rm o}}R_{\rm s} \tag{2.43}$$

In this thesis we provide some essential steps for deriving the luminosity distance at linear order, which was discussed many times [35, 37, 42, 43]. Here, we closely follow the result of Sasaki [35].

According to the energy-momentum conservation and the geodesic equation,

$$\hat{\nabla}_\mu(\mathscr{A}^2\hat{k}^\mu) = 2\mathscr{A}(\frac{\mathrm{d}\mathscr{A}}{\mathrm{d}\hat{\lambda}} + \frac{1}{2}\mathscr{A}\hat{\vartheta}) = 0, \tag{2.44}$$

where $\hat{\vartheta} \equiv \hat{\nabla}_\mu\hat{k}^\mu$.

In the conformally related geometry, one can verify that

$$\nabla_\mu(\mathscr{A}^2a^2k^\mu) = 2\mathscr{A}a(\frac{\mathrm{d}(\mathscr{A}a)}{\mathrm{d}\lambda} + \frac{1}{2}\mathscr{A}a\vartheta) = 0, \tag{2.45}$$

where $\vartheta \equiv \nabla_\mu k^\mu$ is the expansion of the congruence. The evolution of ϑ is described by its covariant derivative along the null path,

$$\frac{\mathrm{d}\vartheta}{\mathrm{d}\lambda} = -R_{\mu\nu}k^\mu k^\nu - \frac{1}{2}\vartheta^2 - 2\sigma^2 \ , \ \sigma^2 = \frac{1}{2}[k^{(\alpha;\beta)}k_{(\alpha;\beta)} - \frac{1}{2}\vartheta^2] \ , \tag{2.46}$$

where σ is the shear of the congruence and $\sigma = 0$ for the spherical symmetric sources (for instance a source associated with a Kerr metric will have non zero shear). At the

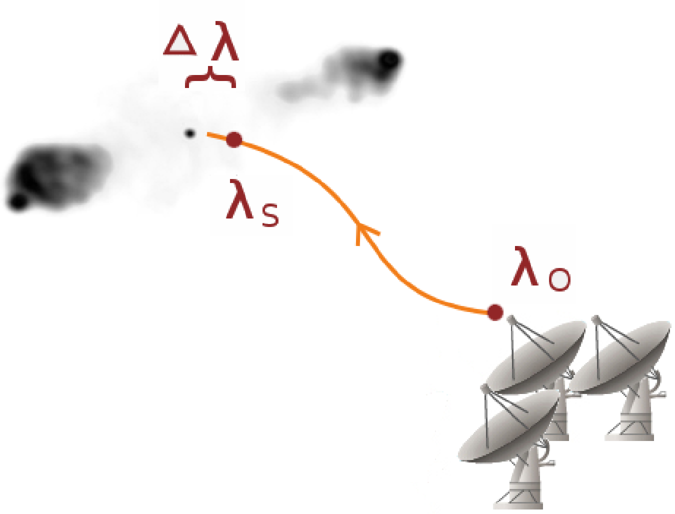

Figure 2.3: Affine parameter convention of a light ray in a radio observation.

zeroth order, the Ricci tensor vanishes in the conformally related geometry, thus one simply gets

$$\begin{aligned}\frac{\mathrm{d}\bar{\vartheta}}{\mathrm{d}\lambda}+\frac{1}{2}\bar{\vartheta}^2&=0,\\ \bar{\vartheta}&=\frac{2}{\lambda+c}.\end{aligned} \tag{2.47}$$

We define λ_o and $\lambda_\mathrm{s}+\Delta\lambda_\mathrm{s}$ for the affine parameter at observer and source, respectively.

As shown in Fig. 2.3, we assume the source is spherical (imagine a large sphere contains core and jets) and its radius in terms of the affine parameter is $\Delta\lambda_\mathrm{s}$. At the point source $\bar{\vartheta}\to\infty$, then $c=-\lambda_\mathrm{s}-\Delta\lambda_\mathrm{s}$, therefore to zeroth order

$$\bar{\vartheta}=\frac{2}{\lambda-\lambda_\mathrm{s}-\Delta\lambda_\mathrm{s}}. \tag{2.48}$$

At first order,

$$\frac{\mathrm{d}\delta\vartheta}{\mathrm{d}\lambda}=-\delta R_{\mu\nu}k^\mu k^\nu-\bar{\vartheta}\delta\vartheta. \tag{2.49}$$

Integration of Eq. (2.49) with the boundary condition $\delta\vartheta(\lambda_\mathrm{s})=0$ yields

$$\delta\vartheta(\lambda)=\frac{1}{(\lambda-\lambda_\mathrm{s}-\Delta\lambda_\mathrm{s})^2}\int_\lambda^{\lambda_\mathrm{s}}(\lambda'-\lambda_\mathrm{s}-\Delta\lambda_\mathrm{s})^2\delta R_{\mu\nu}k^\mu k^\nu\mathrm{d}\lambda'. \tag{2.50}$$

According to Eq. (2.45)

$$\mathscr{A}a = c_1 \exp[-\int_{\lambda_\mathrm{o}}^{\lambda} \frac{\vartheta}{2}\mathrm{d}\lambda]. \tag{2.51}$$

Therefore

$$\frac{\mathscr{A}(\lambda_\mathrm{s})a(\lambda_\mathrm{s})}{\mathscr{A}(\lambda_\mathrm{o})a(\lambda_\mathrm{o})} = \frac{\lambda_\mathrm{s}-\lambda_\mathrm{o}+\Delta\lambda_\mathrm{s}}{\Delta\lambda_\mathrm{s}} \exp[-\int_{\lambda_\mathrm{o}}^{\lambda_\mathrm{s}} \frac{\delta\vartheta}{2}\mathrm{d}\lambda]. \tag{2.52}$$

In the local inertial frame of the source $(\tilde{\eta}, \tilde{x}^i)$,

$$\omega = g_{\mu\nu}u^\mu \hat{k}^\nu = \frac{-1}{a^2}\frac{\mathrm{d}\tilde{\eta}}{\mathrm{d}\lambda}, \tag{2.53}$$

and thus

$$R_\mathrm{s} = \sqrt{\delta_{ij}\mathrm{d}\tilde{x}^i\mathrm{d}\tilde{x}^j} = |\Delta\tilde{\eta}| = a_\mathrm{s}^2\Delta\lambda_\mathrm{s}\omega_\mathrm{s}. \tag{2.54}$$

In the limit $\Delta\lambda_\mathrm{s} \to 0$, the luminosity distance is

$$\begin{aligned} D_\mathrm{L} &= (1+z)\frac{\mathscr{A}_\mathrm{s}}{\mathscr{A}_\mathrm{o}}R_\mathrm{s} \\ &= a_\mathrm{o}(1+z)\frac{a_\mathrm{s}\omega_\mathrm{s}}{k^0}(\eta_\mathrm{s}-\eta_\mathrm{o})[1 - \frac{1}{\eta_\mathrm{s}-\eta_\mathrm{o}}\int_{\lambda_\mathrm{o}}^{\lambda_\mathrm{s}} l^0\mathrm{d}\lambda \\ &\quad -\int_{\lambda_\mathrm{o}}^{\lambda_\mathrm{s}}\frac{\delta\vartheta}{2}\mathrm{d}\lambda] \ , \end{aligned} \tag{2.55}$$

where the term proportional to l^0 comes from replacing the affine parameter by the conformal time. At leading order we can further write

$$\frac{1}{\eta_\mathrm{s}-\eta_\mathrm{o}}\int_{\lambda_\mathrm{o}}^{\lambda_\mathrm{s}} l^0\mathrm{d}\lambda = \frac{1}{\lambda_\mathrm{s}-\lambda_\mathrm{o}}\int_{\lambda_\mathrm{o}}^{\lambda_\mathrm{s}} \frac{l^0}{k^0}\mathrm{d}\lambda. \tag{2.56}$$

Using integration by parts yields

$$\int_{\lambda_\mathrm{o}}^{\lambda_\mathrm{s}} l^0\mathrm{d}\lambda = \int_{\lambda_\mathrm{o}}^{\lambda_\mathrm{s}}(\lambda_\mathrm{s}-\lambda)\frac{\mathrm{d}l^0}{\mathrm{d}\lambda}\mathrm{d}\lambda + (\lambda_\mathrm{s}-\lambda_\mathrm{o})l^0(\lambda_\mathrm{o}). \tag{2.57}$$

According to Eq. (2.32)

$$\begin{aligned} &\int_{\lambda_\mathrm{o}}^{\lambda_\mathrm{s}}\mathrm{d}\lambda(\lambda_\mathrm{s}-\lambda)\frac{\mathrm{d}l^0}{\mathrm{d}\lambda} \\ = &\int_{\lambda_\mathrm{o}}^{\lambda_\mathrm{s}}(\lambda_\mathrm{s}-\lambda)k^2\left[\dot{\Phi}-\dot{\Psi}-\frac{1}{2}e^ie^j(U_{i,j}+U_{j,i}+\dot{h}_{ij})\right]\mathrm{d}\lambda \\ &-2k^0\int_{\lambda_\mathrm{o}}^{\lambda_\mathrm{s}}\left[\phi-(\ddot{E}+\dot{B})\right]\mathrm{d}\lambda - [\dot{E}+B]|_\mathrm{o}^\mathrm{s} \\ &+(\lambda_\mathrm{s}-\lambda_\mathrm{o})[2k^0\phi_\mathrm{o}-k^0(\ddot{E}_\mathrm{o}+\dot{B}_\mathrm{o})+k^i(\dot{E}_\mathrm{o}+B_\mathrm{o})_{,i}] \ , \end{aligned} \tag{2.58}$$

Inserting Eq. (2.50) into the last term of Eq. (2.55), and integrating by parts, we find

$$\begin{aligned}\int_{\lambda_\mathrm{o}}^{\lambda_\mathrm{s}} \frac{\delta\vartheta}{2}\mathrm{d}\lambda &= \int_{\lambda_\mathrm{o}}^{\lambda_\mathrm{s}} \frac{(\lambda_\mathrm{s}-\lambda)(\lambda-\lambda_\mathrm{o})}{2(\lambda_\mathrm{s}-\lambda_\mathrm{o})}\delta R_{\mu\nu}k^\mu k^\nu \mathrm{d}\lambda \\ &= \int_{\lambda_\mathrm{o}}^{\lambda_\mathrm{s}} \mathrm{d}\lambda \frac{(\lambda_\mathrm{s}-\lambda)(\lambda-\lambda_\mathrm{o})}{2(\lambda_\mathrm{s}-\lambda_\mathrm{o})} k^2 \Big[\Delta[\Phi-\Psi] - \Delta U_i e^i \\ &\quad -[\Phi-\Psi]_{,ij}e^ie^j + \frac{1}{2}[\dot{U}_{i,j}+\dot{U}_{j,i}+\ddot{h}_{ij}-\Delta h_{ij}]e^ie^j\Big] \\ &\quad -\psi_\mathrm{s}-\psi_\mathrm{o}+\frac{2}{\lambda_\mathrm{s}-\lambda_\mathrm{o}}\int_{\lambda_\mathrm{o}}^{\lambda_\mathrm{s}}\psi\mathrm{d}\lambda \end{aligned} \tag{2.59}$$

Recall that the photon frequency ω_s is

$$\omega_\mathrm{s} = g_{\mu\nu}u^\mu\hat{k}^\nu = \frac{1}{a_\mathrm{s}}[-k^0 - k^0\phi + k^i(v_i - B_{,i} - S_i) - l^0_\mathrm{s}] \ . \tag{2.60}$$

Finally, inserting Eq. (2.59) and Eq. (2.58) into Eq. (2.55), the luminosity distance can be expressed in terms of gauge invariant quantities as

$$\begin{aligned} &D_\mathrm{L} = \mathcal{A}_\mathrm{o}(1+z)(\chi_\mathrm{o}-\chi_\mathrm{s})\Big[1+\Psi_\mathrm{o}-\Phi_\mathrm{s}+\Psi_\mathrm{s}+e^i(V_i)_\mathrm{s}+k^0\int_{\lambda_\mathrm{o}}^{\lambda_\mathrm{s}}(\dot{\Phi}-\dot{\Psi})\mathrm{d}\lambda \\ &+\frac{2}{\eta_\mathrm{s}-\eta_\mathrm{o}}\int_{\lambda_\mathrm{o}}^{\lambda_\mathrm{s}}k^0(\Phi-\Psi)\mathrm{d}\lambda - \frac{1}{\eta_\mathrm{s}-\eta_\mathrm{o}}\int_{\lambda_\mathrm{o}}^{\lambda_\mathrm{s}}(\lambda_\mathrm{s}-\lambda)k^2(\dot{\Phi}-\dot{\Psi})\mathrm{d}\lambda \\ &-\int_{\lambda_\mathrm{o}}^{\lambda_\mathrm{s}}\mathrm{d}\lambda\frac{(\lambda_\mathrm{s}-\lambda)(\lambda-\lambda_\mathrm{o})}{2(\lambda_\mathrm{s}-\lambda_\mathrm{o})}k^2[\Delta(\Phi-\Psi)-(\Phi-\Psi)_{,ij}e^ie^j] \\ &-k^0\int_{\lambda_\mathrm{o}}^{\lambda_\mathrm{s}}\frac{1}{2}e^ie^j(U_{i,j}+U_{j,i}+\dot{h}_{ij})\mathrm{d}\lambda \\ &+\frac{1}{\eta_\mathrm{s}-\eta_\mathrm{o}}\int_{\lambda_\mathrm{o}}^{\lambda_\mathrm{s}}(\lambda_\mathrm{s}-\lambda)k^2[\frac{1}{2}e^ie^j(U_{i,j}+U_{j,i}+\dot{h}_{ij})]\mathrm{d}\lambda \\ &-\int_{\lambda_\mathrm{o}}^{\lambda_\mathrm{s}}\mathrm{d}\lambda\frac{(\lambda_\mathrm{s}-\lambda)(\lambda-\lambda_\mathrm{o})}{2(\lambda_\mathrm{s}-\lambda_\mathrm{o})}k^2[\frac{1}{2}(\dot{U}_{i,j}+\dot{U}_{j,i}+\ddot{h}_{ij}-\Delta h_{ij})e^ie^j-\Delta U_ie^i]\Big], \end{aligned} \tag{2.61}$$

where $\chi_\mathrm{o}-\chi_\mathrm{s}\equiv\eta_\mathrm{o}-\eta_\mathrm{s}+[\dot{E}+B]|^\mathrm{o}_\mathrm{s}$.

At long wavelengths, synchrotron radiation is the dominant radiation process, which suggests that the emitted flux density from a radio source follows a power law (see Fig. 2.2),

$$S_\mathrm{s}(\omega_\mathrm{s}) \propto \omega_\mathrm{s}^{-\alpha}, \tag{2.62}$$

where α is the spectral index.

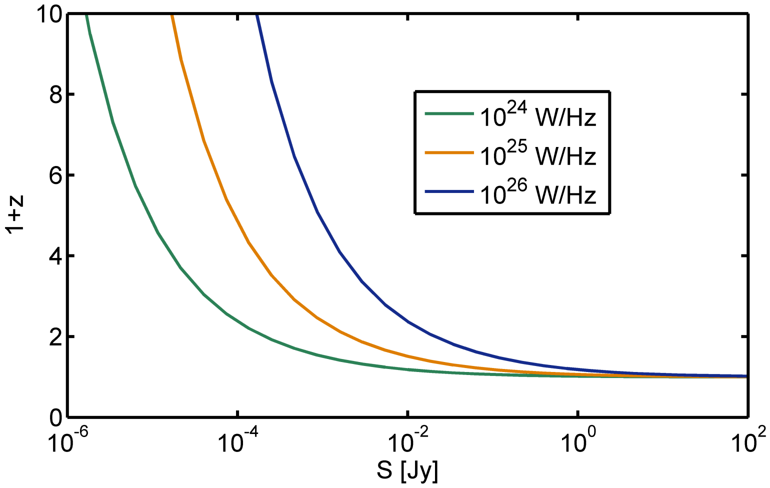

Figure 2.4: Flux-redshift relation for different specific luminosities typical for AGNs. The standard Λ cold dark matter model has been adopted, and the spectral index α has been chosen to be 0.75.

To infer the distance of a source that is neither monochromatic nor thermal requires the detailed knowledge of its spectrum (besides its luminosity). For featureless spectra the redshift is typically unknown. It is thus convenient to compare the observed specific flux density to the specific luminosity at the observed frequency and we use the observed bandwidth. We define the specific luminosity distance,

$$D_S \equiv \sqrt{\frac{L_\mathrm{s}(\omega_\mathrm{o})\mathrm{d}\omega_\mathrm{o}}{4\pi S_\mathrm{o}(\omega_\mathrm{o})\mathrm{d}\omega_\mathrm{o}}} = (1+z)^{(\alpha-1)/2} D_L. \tag{2.63}$$

The last term in Eq. (2.63) connects the specific luminosity distance with the (monochromatic/bolometric) luminosity distance D_L.

In the following our task is to calculate the specific flux density of a radio source, taking all linear fluctuations into account. We can write

$$S_\mathrm{o}(\omega_\mathrm{o}) = S_\mathrm{s}(\omega_\mathrm{o})\frac{R_\mathrm{s}^2}{D_S^2} = \frac{L_\mathrm{s}(\omega_\mathrm{o})}{4\pi}\frac{1}{(1+z)^{\alpha+1}R_\mathrm{o}^2}. \tag{2.64}$$

where $D_L = R_\mathrm{o}(1+z)$ and $R_\mathrm{o} \equiv \sqrt{\mathrm{d}A_\mathrm{o}/\mathrm{d}\Omega_\mathrm{s}}$is the physical distance (today).

For the standard cosmological (homogeneous and isotropic) model, this relation between flux density and redshift is shown in Fig. 2.4 for several typical specific luminosities of radio sources. The linear distortions of redshift were presented in the previous subsection. Analogous to the redshift distortion, we define the physical distance fluctuation δ_d via

$$R_\mathrm{o} = \frac{D_\mathrm{L}}{1+z} = a_\mathrm{o}(\eta_\mathrm{o} - \eta_\mathrm{s})[1 + \delta_d], \tag{2.65}$$

where δ_d is then given by comparison with the expression for the luminosity distance at linear order, which has been discussed in [35, 37, 42].

According to Eq. 2.61 R_o can be expressed in terms of gauge invariant quantities as

$$\begin{aligned}
R_\mathrm{o} \;=\;& \mathcal{A}_\mathrm{o}(\chi_\mathrm{o} - \chi_\mathrm{s})\Bigg[1 + \Psi_\mathrm{o} - \Phi_\mathrm{s} + \Psi_\mathrm{s} + e^i(V_i)_\mathrm{s} + k^0 \int_{\lambda_\mathrm{o}}^{\lambda_\mathrm{s}} (\dot{\Phi} - \dot{\Psi})\mathrm{d}\lambda \\
& + \frac{2}{\eta_\mathrm{s} - \eta_\mathrm{o}} \int_{\lambda_\mathrm{o}}^{\lambda_\mathrm{s}} k^0(\Phi - \Psi)\mathrm{d}\lambda - \frac{1}{\eta_\mathrm{s} - \eta_\mathrm{o}} \int_{\lambda_\mathrm{o}}^{\lambda_\mathrm{s}} (\lambda_\mathrm{s} - \lambda)k^2(\dot{\Phi} - \dot{\Psi})\mathrm{d}\lambda \\
& - \int_{\lambda_\mathrm{o}}^{\lambda_\mathrm{s}} \mathrm{d}\lambda \frac{(\lambda_\mathrm{s} - \lambda)(\lambda - \lambda_\mathrm{o})}{2(\lambda_\mathrm{s} - \lambda_\mathrm{o})} k^2 \Big[\Delta(\Phi - \Psi) - (\Phi - \Psi)_{,ij}e^i e^j\Big] \\
& - k^0 \int_{\lambda_\mathrm{o}}^{\lambda_\mathrm{s}} \frac{1}{2} e^i e^j (U_{i,j} + U_{j,i} + \dot{h}_{ij})\mathrm{d}\lambda \\
& + \frac{1}{\eta_\mathrm{s} - \eta_\mathrm{o}} \int_{\lambda_\mathrm{o}}^{\lambda_\mathrm{s}} (\lambda_\mathrm{s} - \lambda)k^2[\frac{1}{2} e^i e^j (U_{i,j} + U_{j,i} + \dot{h}_{ij})]\mathrm{d}\lambda \\
& - \int_{\lambda_\mathrm{o}}^{\lambda_\mathrm{s}} \mathrm{d}\lambda \frac{(\lambda_\mathrm{s} - \lambda)(\lambda - \lambda_\mathrm{o})}{2(\lambda_\mathrm{s} - \lambda_\mathrm{o})} k^2[\frac{1}{2}(\dot{U}_{i,j} + \dot{U}_{j,i} + \ddot{h}_{ij} - \Delta h_{ij})e^i e^j - \Delta U_i e^i]\Bigg].
\end{aligned} \tag{2.66}$$

We have checked that R_o is manifestly gauge invariant.

As shown so far, distortions of the specific flux are affected by redshift distortions δz and physical distance fluctuations δ_d. Besides these geometrical effects, the specific luminosity and spectra of different sources are not identical, which provides another source of fluctuation. Thus, we allow $L_\mathrm{s}(\omega_\mathrm{o})$ and α to vary and denote its fluctuations by $\delta L_\mathrm{s}(\omega_\mathrm{o}) = L_\mathrm{s}(\omega_\mathrm{o}) - \bar{L}_\mathrm{s}(\omega_\mathrm{o})$ and $\delta\alpha = \alpha - \bar{\alpha}$, respectively. The specific flux density can be written as

$$S_\mathrm{o}(\omega_\mathrm{o}) = \bar{S}_\mathrm{o}(\omega_\mathrm{o})(1 + \delta_S), \tag{2.67}$$

where

$$\bar{S}_\mathrm{o}(\omega_\mathrm{o}) = \frac{\bar{L}_\mathrm{s}(\omega_\mathrm{o})}{4\pi a_\mathrm{o}^2(1+\bar{z})^{\bar{\alpha}+1}(\eta_\mathrm{o} - \eta_\mathrm{s})^2} \tag{2.68}$$

and the specific flux fluctuation is

$$\delta_S = \frac{\delta L_\mathrm{s}(\omega_\mathrm{o})}{\bar{L}_\mathrm{s}(\omega_\mathrm{o})} - 2\delta_d - (\bar{\alpha}+1)\delta z - \delta\alpha \ln(1+\bar{z}). \tag{2.69}$$

On one hand, at high redshifts and large fields of view (a large sample) the geometric terms $(-2\delta_d - (\bar{\alpha}+1)\delta z)$ are likely to dominate δ_S. On the other hand, at low redshift and small fields of view, $\delta\alpha$ and δL_s may play a significant role, which might explain some of the variation observed[44] in the differential number counts in small fields.

2.4.4 Number Counts in Observed Spherical Coordinates and Lensing Effect

The fluctuations mentioned above have to be taken into account when we do the coordinate transformation from the background coordinates (r, θ, φ) to the observed coordinates $(r_\mathrm{o}, \theta_\mathrm{o}, \varphi_\mathrm{o})$ (see Fig. 2.5). We assume that the two sets of coordinates are related by small quantities, such that

$$\begin{aligned} r &= r_\mathrm{o} + \delta r, \\ \theta &= \theta_\mathrm{o} + \delta\theta, \\ \varphi &= \varphi_\mathrm{o} + \delta\varphi. \end{aligned} \tag{2.70}$$

The comoving distance fluctuation is defined as the difference between the line of sight distance r in the comoving coordinates and the distance r_o inferred from the observed flux density S_o for a fixed luminosity, measured spectral index and assumed luminosity. Unlike the former, r_o is in principle a measurable quantity and it is invariant under coordinate transformations.

The observed flux is a function of the conformal time. Using $\bar{r} \equiv \eta_\mathrm{o} - \eta$ and Eq. (2.68), we explicitly define the function $\bar{r} = \bar{r}(\bar{S}_\mathrm{o})$, and the inferred distance $r_\mathrm{o} \equiv \bar{r}(S_\mathrm{o})$. Expanding this definition at background flux leads to

$$\begin{aligned} \bar{r}(S_\mathrm{o}) &= \bar{r}(\bar{S}_\mathrm{o}) + \frac{\mathrm{d}\bar{r}}{\mathrm{d}\bar{S}_\mathrm{o}}(S_\mathrm{o} - \bar{S}_\mathrm{o}) \\ r_\mathrm{o} &= \eta_\mathrm{o} - \eta - \frac{(\eta_\mathrm{o} - \eta)\delta_S}{2 + (\bar{\alpha}+1)(\eta_\mathrm{o} - \eta)\mathcal{H}}. \end{aligned} \tag{2.71}$$

The linear order light cone relation in the background coordinates is

$$\eta_\mathrm{o} - \eta - \int_\lambda^{\lambda_\mathrm{o}} \mathrm{d}\lambda' l^0 = r - \int_{\lambda_\mathrm{o}}^{\lambda} \mathrm{d}\lambda l^i e_i^r, \tag{2.72}$$

where l^μ is the wave vector fluctuation caused by metric fluctuation in the conformally related geometry, which is mentioned in the previous section on redshift distortion.

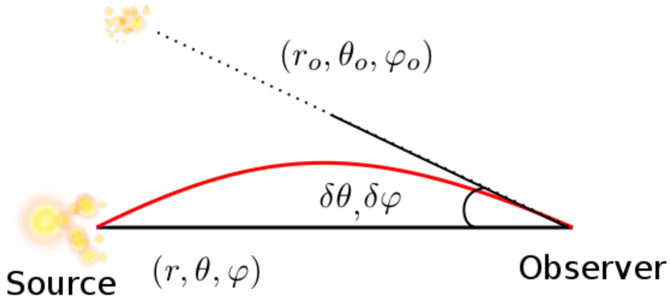

Figure 2.5: Observed position vs. background position.

According to the null condition Eq. (2.29), one can find the comoving distance fluctuation

$$\begin{aligned}\delta r &= r - r_{\rm o} \qquad (2.73)\\ &= \frac{r_{\rm o}\delta_S}{2+(\bar\alpha+1)r_{\rm o}\mathcal{H}} + [\frac{k^iF_i}{k^0} - B + \frac{k^iE_{,i}}{k^0} - \dot E]|_{\rm o}^{\rm s}\\ &+ \int_{\rm o}^{\rm s} {\rm d}\lambda(-k^0\Phi + k^0\Psi - U_ik^i + \frac{k^ik^j}{2k^0}h_{ij}),\end{aligned}$$

where we have replaced $\eta_{\rm o} - \eta$ by $r_{\rm o}$, which introduces contributions at higher order that we neglect.

Metric perturbations can deflect and disperse light rays and thus displace the observed angles on the sky (see Fig. 2.5). Following [45], we start from an infinitesimal angle deviation $\delta\theta$,

$$r\delta\theta = e_{\theta i}\delta x^i = \int_{\rm o}^{\rm s} {\rm d}\lambda e_{\theta i} l^i, \qquad (2.74)$$

where $e^{\theta i}$ is the unit vector pointing into the angular direction. Since angles are not affected by conformal transformations, $\delta\theta$ can be calculated from the geodesic equation in the conformally related geometry,

$$\begin{aligned}\frac{{\rm d}l^i}{{\rm d}\lambda} &= -\Gamma^{(1)i}_{\sigma\rho}k^\sigma k^\rho\\ &= -\frac{1}{2}\delta^{i\alpha}(g^{(1)}_{\sigma\alpha,\rho} + g^{(1)}_{\rho\alpha,\sigma} - g^{(1)}_{\sigma\rho,\alpha})k^\sigma k^\rho\\ &= -\frac{{\rm d}\delta^{i\alpha}g^{(1)}_{\sigma\alpha}}{{\rm d}\lambda}k^\sigma + \frac{1}{2}\delta^{i\alpha}g^{(1)}_{\sigma\rho,\alpha}k^\sigma k^\rho. \qquad (2.75)\end{aligned}$$

With the help of $\frac{\mathrm{d}k^\mu}{\mathrm{d}\lambda} = \Gamma^{(0)\mu}_{\sigma\rho} k^\sigma k^\rho = 0$, we find

$$e_{\theta i} l^i|_{\mathrm{o}}^{\mathrm{s}} = -e^{\theta i}[g^{(1)}_{0i} k^0 + g^{(1)}_{ji} k^j]_{\mathrm{o}}^{\mathrm{s}} + \frac{1}{2}\int_{\mathrm{o}}^{\mathrm{s}} \mathrm{d}\lambda e^{\theta i} g^{(1)}_{\sigma\rho,i} k^\sigma k^\rho. \tag{2.76}$$

Integrate $e_{\theta i} l^i$ along the path to obtain

$$\begin{aligned} \delta\theta &= -\frac{1}{r_{\mathrm{o}}}\int_{\mathrm{o}}^{\mathrm{s}} \mathrm{d}\lambda \bigg(e^{\theta i}[g^{(1)}_{0i} k^0 + g^{(1)}_{ji} k^j]_{\mathrm{o}}^{\mathrm{s}} \\ &\quad - \frac{\lambda_{\mathrm{s}} - \lambda}{2r} g^{(1)}_{\sigma\rho,\theta} k^\sigma k^\rho \bigg), \end{aligned} \tag{2.77}$$

where the double integral can be simplified as $\int_{\lambda_{\mathrm{o}}}^{\lambda_{\mathrm{s}}} \mathrm{d}\lambda' \int_{\lambda_{\mathrm{o}}}^{\lambda'} f(\lambda)\mathrm{d}\lambda = \int_{\lambda_{\mathrm{o}}}^{\lambda_{\mathrm{s}}} f(\lambda)(\lambda_{\mathrm{s}} - \lambda)\mathrm{d}\lambda$, and we use $e^{\theta i} g^{(1)}_{\sigma\rho,i} = g^{(1)}_{\sigma\rho,\theta}/r$.

An analogous calculation gives

$$\begin{aligned} \delta\varphi &= -\frac{1}{r_{\mathrm{o}}\sin\theta_{\mathrm{o}}}\int_{\mathrm{o}}^{\mathrm{s}} \mathrm{d}\lambda \bigg(e^{\varphi i}[g^{(1)}_{0i} k^0 + g^{(1)}_{ji} k^j]_{\mathrm{o}}^{\mathrm{s}} \\ &\quad - \frac{\lambda_{\mathrm{s}} - \lambda}{2r\sin\theta_{\mathrm{o}}} g^{(1)}_{\sigma\rho,\varphi} k^\sigma k^\rho \bigg). \end{aligned} \tag{2.78}$$

For further details see [45].

The Jacobian of the transformation from the background coordinates to the observed coordinates is

$$\det(J) = \frac{1}{S_o}\frac{-r_{\mathrm{o}}}{2 + (\bar{\alpha}+1) r_{\mathrm{o}}\mathcal{H}}[1 + \frac{\mathrm{d}\delta r}{\mathrm{d}r_{\mathrm{o}}} + \frac{\partial\delta\theta}{\partial\theta_{\mathrm{o}}} + \frac{\partial\delta\varphi}{\partial\varphi_{\mathrm{o}}}]. \tag{2.79}$$

The prefactor is gauge invariant, since it is the derivative of observed flux with respect to the inferred distance r_{o}. To linear order,

$$\frac{\mathrm{d}\delta r}{\mathrm{d}r_{\mathrm{o}}} = \frac{\partial\delta r}{\partial r} - \frac{\partial\delta r}{\partial\eta}, \tag{2.80}$$

and according to the transformation law of vectors, the three-velocity of the source can be expressed in observed coordinates as

$$V'^i = v^i - \frac{\partial\delta x^i}{\partial\eta}. \tag{2.81}$$

2.5 Galaxy Number Counts II

We combine the previous results with the expression for Eq. (2.16) to obtain the total number count for the sources with identical luminosity,

$$\begin{aligned} N &= \int \mathrm{d}\Omega_\mathrm{o} \int \frac{\mathrm{d}S_\mathrm{o}}{S_\mathrm{o}} \frac{a^3 r_\mathrm{o}^3 n_\mathrm{phy}}{2+(\bar{\alpha}+1) r_\mathrm{o}\mathcal{H}} [1+3\psi+\Delta E \\ &\quad + V'^{i} e_i^r + 2\frac{\delta r}{r_\mathrm{o}} + \frac{\partial \delta r}{\partial r_\mathrm{o}} - 2\kappa_\mathrm{g}], \end{aligned} \tag{2.82}$$

where we changed $\partial\delta r/\partial r$ to $\partial\delta r/\partial r_\mathrm{o}$, since δr is a first order quantity. κ_g denotes the gravitational lensing convergence,

$$\kappa_\mathrm{g} = -\frac{1}{2}[(\cot\theta_\mathrm{o} + \frac{\partial}{\partial\theta_\mathrm{o}})\delta\theta + \frac{\partial\delta\varphi}{\partial\varphi_\mathrm{o}}]. \tag{2.83}$$

Inserting the angular displacements into Eq. (2.83), we get

$$\begin{aligned} \kappa_\mathrm{g} = \frac{1}{2r_\mathrm{o}} \int_\mathrm{o}^\mathrm{s} \mathrm{d}\lambda(\lambda_\mathrm{s}-\lambda) \Bigg[\frac{1}{2r(\lambda)} \hat{\nabla}^2 \left(2k^2(\Phi-\Psi) + 2U_i k^i k^0 - k^i k^j h_{ij}\right) \quad (2.84) \\ +[(\cot\theta_\mathrm{o} + \frac{\partial}{\partial\theta_\mathrm{o}})e^{\theta i} + \frac{1}{\sin(\theta_\mathrm{o})}\frac{\partial}{\partial\varphi_\mathrm{o}} e^{\varphi i}] \frac{\mathrm{d}}{\mathrm{d}\lambda}(-U_i k^0 + h_{ij}k^j) \\ +[(\cot\theta_\mathrm{o} + \frac{\partial}{\partial\theta_\mathrm{o}})e^{\theta i} + \frac{1}{\sin(\theta_\mathrm{o})}\frac{\partial}{\partial\varphi_\mathrm{o}} e^{\varphi i}] \frac{\mathrm{d}^2}{\mathrm{d}\lambda^2}\left(E_{,i} + F_i\right) \Bigg], \end{aligned}$$

where $\hat{\nabla}^2$ is the Laplacian operator on a unit sphere,

$$\hat{\nabla}^2 = \cot\theta_\mathrm{o}\frac{\partial}{\partial\theta} + \frac{\partial^2}{\partial\theta_\mathrm{o}^2} + \frac{1}{\sin^2(\theta_\mathrm{o})}\frac{\partial^2}{\partial\varphi_\mathrm{o}^2}. \tag{2.85}$$

According to its definition, κ_g describes the solid angle difference between the observer coordinates and the background coordinates. Since the background coordinates are not measurable, κ_g changes under coordinate transformations. A gauge invariant quantity,

$$\begin{aligned} K_\mathrm{g} &\equiv \kappa_\mathrm{g} - \frac{1}{2r_\mathrm{o}} \int_\mathrm{o}^\mathrm{s} \mathrm{d}\lambda(\lambda_\mathrm{s}-\lambda)[(\cot\theta_\mathrm{o} + \frac{\partial}{\partial\theta_\mathrm{o}})e^{\theta i} \\ &\quad + \frac{1}{\sin(\theta_\mathrm{o})}\frac{\partial}{\partial\varphi_\mathrm{o}} e^{\varphi i}] \frac{\mathrm{d}^2}{\mathrm{d}\lambda^2}\left(E_{,i} + F_i\right), \end{aligned} \tag{2.86}$$

can be inferred from the angular diameter distance fluctuations. After gauge fixing, K_g agrees with the gravitational lensing convergence in [46, 47]. Additionally, it is useful to also define a gauge invariant comoving distance fluctuation

$$\delta R \equiv \delta r - [\frac{k^i F_i}{k^0} + \frac{k^i E_{,i}}{k^0}]|_\mathrm{o}^\mathrm{s}. \tag{2.87}$$

The gauge dependent contributions in κ_{g} and δr, which depend on the position of the source, cancel the ΔE term (from $\sqrt{-g}$) in Eq. (2.82).

We have checked that the result Eq. (2.82) agrees with [48] at the background level after replacing flux density by redshift. Our comoving distance fluctuation is different due to the different choice of observable (we consider flux density, they consider redshift).

2.5.1 Radio Galaxy Luminosity Function

In the previous sections, we have evaluated the effect of volume fluctuations, without fully specifying the physical number density n_{phy}. The physical number density n_{phy} can be separate into a mean number density $\bar{n}_{\mathrm{phy}}$ and a fluctuation around it δ_g,

$$n_{\mathrm{phy}} = \bar{n}_{\mathrm{phy}}(1+\delta_g) \tag{2.88}$$

where the mean number density $\bar{n}_{\mathrm{phy}}$ can be written as the composition of the radio galaxy intrinsic luminosity function and its evolution.

Radio sources fall into two principle classes, active galactic nuclei (AGN) and star forming galaxies (SFG). The physical number density n_{phy} can be considered as the sum of all classes of sources (e.g. AGN or SFG, or any finer classification),

$$n_{\mathrm{phy}}(L, S_{\mathrm{o}}, \theta_{\mathrm{o}}, \varphi_{\mathrm{o}}) = \sum_i \rho_i(L) p_i(L, r_{\mathrm{o}})(1+\Delta_{g_i}(L, S_{\mathrm{o}}, \theta_{\mathrm{o}}, \varphi_{\mathrm{o}})),$$

where the index i characterizes the different types of sources, $\rho_i(L)$ and $p_i(L, r_{\mathrm{o}})$ are the local (today's) luminosity function and the generalized evolution function. Δ_{g_i} is the gauge invariant number density fluctuation in observed coordinates.

The measured local luminosity function is shown in Fig. 2.6. It is common to parametrize the radio luminosity function in terms of a sum of double power-laws [49],

$$\rho(L) = \rho_n[(\frac{L}{L_c})^{\beta} + (\frac{L}{L_c})^{\gamma}]^{-1}. \tag{2.89}$$

Another prominent function is the Schechter luminosity function [50]

$$\rho(L) = \rho_n(\frac{L}{L_c})^{-\beta}\exp(-\frac{L}{L_c}), \tag{2.90}$$

which has a physical foundation, in contrast to the double power-law function. The Schechter luminosity function reflects the expected mass distribution of galaxies formed

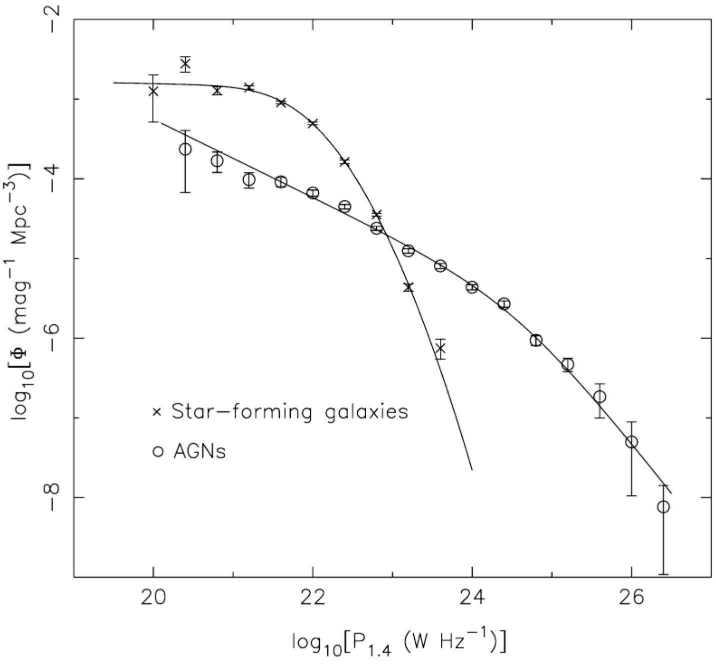

Figure 2.6: Local luminosity function at 1.4 GHz derived separately for radio-loud AGNs and SF galaxies in the 6 degree Field Galaxy Survey (6dFGS)-NVSS sample, copy from [9].

by self-similar gravitational condensation and thus should be the luminosity function of galaxies having the same mass-to-light ratio. It fits the optical galaxies well, but cuts off far more sharply at high luminosities for radio galaxies.

We thus arrive at one of the central results of this thesis, the expression for the number counts including all linear order effects,

$$\begin{aligned}\sigma(>S_t) &\equiv \frac{\mathrm{d}N}{\mathrm{d}\Omega_\mathrm{o}}(>S_t) \\ &= \sum_i \int_{S_t}^{\infty} \frac{\mathrm{d}S_\mathrm{o}}{S_\mathrm{o}} \int_0^{\infty} \mathrm{d}L \rho_i(L) p_i(L, r_\mathrm{o}) \frac{\mathcal{A}^3 r_o^3}{2 + (\bar{\alpha}_i + 1) r_o \mathcal{H}} \times \\ &\quad [1 + \Delta_{g_i} + 3\Psi + V' \cdot e^r + 2\frac{\delta R}{r_o} + \frac{\partial \delta R}{\partial r_o} - 2K_\mathrm{g}].\end{aligned} \tag{2.91}$$

Chapter 3

Predictions for Galaxy two-point Statistics

The full relativistic expression of the galaxy number count up to linear order is discussed in the previous chapter. Considering the statistical error of a radio galaxy survey is large, we first take the dominated leading term, i.e. the physical number density fluctuation into account and neglect all other effects. The next-to-leading effect will be discussed in the discussion 5.4. Since the luminosity and density evolution of radio galaxies is quite significant and there is no widely recognized evolution model in luminosity space, we turn to redshift space and define a galaxy surface density fluctuation as

$$\begin{aligned} \Theta(\hat{n}) &\equiv \frac{\sigma(>S_t)(\hat{n})-\bar{\sigma}}{\bar{\sigma}} \\ &= \frac{1}{\bar{\sigma}}\int \mathrm{d}z \frac{a^3 r_{\mathrm{o}}^2}{H}\bar{n}_{\mathrm{phy}}\delta_g \\ &= \frac{1}{\bar{\sigma}}\int \mathrm{d}z f(z)\delta_g \ , \end{aligned} \tag{3.1}$$

where $f(z)$ is the differential number density of sources per solid angle at redshift z with source flux density above S_t. Next one has to relate the number density fluctuation to the underlying matter density fluctuation δ_m. We assume that

$$\delta_g(z,\hat{n}) = b(z)\delta_m(z,\hat{n}) \tag{3.2}$$

where $b(z)$ denotes the bias, and $\delta_m(z,\hat{n})$ is the matter density contrast in synchronous comoving gauge. Due to the broad shape of the luminosity function, the radio galaxy redshift distribution shows only a weak dependence on the flux threshold S_t [51, 52]. This argument holds true, as for $S >$ few mJy the differential number counts are dominated by active galactic nuclei, i.e. the flux density threshold is well above the flux density of a typical star forming galaxy. Accordingly we drop the flux threshold S_t in Eq. 3.1.

It is straightforward to decompose the observed sky into the spherical harmonics

$$\Theta(\hat{n}) = \sum_{l,m} a_{lm} Y_{lm}(\hat{n}) \ , \tag{3.3}$$

where $Y_{lm}(\hat{n})$ denote the spherical harmonic functions. One can also express $\Theta(\hat{n})$ as

$$\begin{aligned} \Theta(\hat{n}) &= \frac{1}{\bar{\sigma}} \int \mathrm{d}z f(z) b(z) \int \frac{\mathrm{d}^3 k}{(2\pi)^3} e^{i\vec{k}\vec{r}} \delta_m(\vec{k}, z) \\ &= \frac{1}{\bar{\sigma}} \int \mathrm{d}z f(z) b(z) D(z) \int \frac{\mathrm{d}^3 k}{(2\pi)^3} e^{i\vec{k}\vec{r}} \delta_m(\vec{k}) \ , \end{aligned} \tag{3.4}$$

where $D(z)$ is the growth factor and $\vec{r} \equiv \hat{n} r(z)$. Since $e^{i\vec{k}\vec{r}} = 4\pi \sum_{lm} i^l j_l(kr) Y^*_{lm}(\hat{k}) Y_{lm}(\hat{n})$ the coefficient a_{lm} can be obtained as

$$\begin{aligned} a_{lm} &= \frac{4\pi}{\bar{\sigma}} i^l \int \frac{\mathrm{d}^3 k}{(2\pi)^3} \int \mathrm{d}z f(z) b(z) D(z) j_\ell|(kr) Y^*_{lm}(\hat{k}) \delta_m(\vec{k},) \\ &= 4\pi i^l \int \frac{\mathrm{d}^3 k}{(2\pi)^3} W_l(k) Y^*_{lm}(\hat{k}) \delta_m(\vec{k}) \ , \end{aligned} \tag{3.5}$$

where $j_\ell(x)$ is a spherical Bessel function of the first kind and $W_l(k)$ is the window function

$$W_l(k) \equiv \frac{1}{\bar{\sigma}} \int \mathrm{d}z f(z) b(z) D(z) j_\ell(kr) \ . \tag{3.6}$$

3.1 Angular Power Spectrum

Since many catalogues list angular positions of galaxies, it is practical to think of the matter distribution as a distribution of point-like objects. By assuming all the objects are nearly identical, one can describe the 2D distribution with the n-point correlation functions. Among the n-point correlation functions, the two-point correlation function is the most important one in a Gaussian random field. Even though the number of radio sources in a pixel is governed by the Poisson distribution, Gaussian distribution is a good approximation as long as the mean number of radio sources per pixel is large enough (The meaning of 'large' depends on how good an agreement one requires and some people put requirement > 10 [53]).

The angular power spectrum C_l is defined as the variance of the a_{lm}:

$$\langle a_{lm} a^*_{l'm'} \rangle = \delta_{ll'} \delta_{mm'} C_l \quad , \tag{3.7}$$

where $\langle\rangle$ denote ensemble averaging and

$$\langle a_{lm} a^*_{l'm'} \rangle = (4\pi)^2 i^l (-i)^{l'} \int \frac{\mathrm{d}^3k \mathrm{d}^3k'}{(2\pi)^6} W_l(k) W_{l'}(k') Y^*_{lm}(\hat{k}) Y_{l'm'}(\hat{k}') \langle \delta_m(\vec{k}) \delta^*_m(\vec{k'}) \rangle \ . \tag{3.8}$$

With the hypothesis of homogeneity and isotropy, $\langle \delta_m(\vec{k}) \delta^*_m(\vec{k'}) \rangle = (2\pi)^3 P(k) \delta^{(3)}(\vec{k} - \vec{k}')$, the expression simplifies,

$$\begin{aligned} \langle a_{lm} a^*_{l'm'} \rangle &= i^l (-i)^{l'} \frac{2}{\pi} \int \mathrm{d}^3k W_l(k) W_{l'}(k) Y^*_{lm}(\hat{k}) Y_{l'm'}(\hat{k}) P(k) \\ &= 4\pi \int \frac{\mathrm{d}k}{k} W_l(k)^2 \frac{k^3 P(k)}{2\pi^2} \delta_{ll'} \delta_{mm'} \end{aligned} \tag{3.9}$$

where the last line we used the orthogonality condition for spherical harmonics and $P(k)$ is the matter power spectrum today.

It is worth to clarify that one can not directly measure C_l, because we have only one universe, i.e. one set of a_{lm}. To solve this issue, one has trade averaging over an ensemble for averaging over space. In our case, for a given multipole l we consider a_{lm}s with $2l + 1$ different value of m as a statistical ensemble. Therefore, one can define an estimator for C_l,

$$\hat{C}_l \equiv \frac{1}{2l+1} \sum_{m=-l}^{l} |a_{lm}|^2 \quad . \tag{3.10}$$

In such case, it is important to note that we do not have much information for low multipoles, i.e. small l. There is a fundamental uncertainty of $\hat{C}l$, named cosmic variance. It is due to the finite number of harmonics associated with the lth multipole. If a_{lm}s are Gaussian distributed, then $\sum_{m=-l}^{l} |a_{lm}|^2$ following a χ^2 distribution and the rms of C_l is

$$\Delta C_l = C_l \sqrt{\frac{2}{2l+1}} \quad . \tag{3.11}$$

3.2 Angular two-point Correlation Function

The angular two-point correlation $w(\theta)$ is defined as the joint probability δP of finding galaxies in both of the elements of solid angle $\delta\Omega_1$ and $\delta\Omega_2$ separated by an angle θ [54],

$$\delta P = \bar{\sigma}^2 \delta\Omega_1 \delta\Omega_2 [1 + w(\theta)] \tag{3.12}$$

where $\bar{\sigma}$ is the mean surface density.

For a statistically isotropic distribution of radio galaxies the angular two-point correlation $w(\theta)$ can be determined from the angular power spectrum C_l,

$$\begin{aligned} w(\theta) &\equiv \langle \Theta(\hat{n}) \Theta(\hat{n}') \rangle \\ &= \sum_{ll'mm'} \langle \Theta(\hat{n}) \Theta(\hat{n}') \rangle Y_{lm}(\hat{n}) Y^*_{l'm'}(\hat{n}') \\ &= \sum_l C_l \sum_{m=-l}^{l} Y_{lm}(\hat{n}) Y^*_{lm}(\hat{n}') \\ &= \frac{1}{4\pi} \sum_l (2l+1) C_l P_l(\cos\theta) \,, \end{aligned} \tag{3.13}$$

where $P_l(x)$ are Legendre polynomials. Similarly, using the orthogonality of $P_l(x)$

$$C_l = 2\pi \int_{-1}^{1} w(\theta) P_l(\cos\theta) \mathrm{d}\cos\theta \quad . \tag{3.14}$$

The angular two-point correlation could be estimated from [54]

$$1 + w(\theta) = \frac{DD}{N(N+1)/2} \frac{\Omega}{\langle \delta\Omega \rangle} \tag{3.15}$$

where DD denotes the count of pairs at separation θ and N denotes the total number of objects considered in the analysis. $N(N+1)/2$ is the total number of possible pairs. Ω is the solid angle of the survey, and $\langle \delta\Omega \rangle$ is the averaged solid angle of the ring θ to $\theta + \delta\theta$ within Ω for a randomly placed ring center in Ω.

In the full sky case, $\langle \delta\Omega \rangle = 2\pi \sin\theta\delta\theta$. Several methods for computing $\langle \delta\Omega \rangle$ have been used. For the very complicated Ω, it cannot be computed analytically, one has to derive $\langle \delta\Omega \rangle$ by means of Monte Carlo integration [55].

However, it turns out that the estimator in Eq. 3.15 is not optimal. For our analysis we use the optimized estimator found by Landy and Szalay [56],

$$w_{\mathrm{LS}}(\theta) = \frac{N_{\mathrm{r}}(N_{\mathrm{r}}+1)}{N(N+1)} \frac{DD}{\overline{\overline{RR}}} - N(N_{\mathrm{r}}+1) \frac{\overline{DR}}{\overline{\overline{RR}}} + 1 \tag{3.16}$$

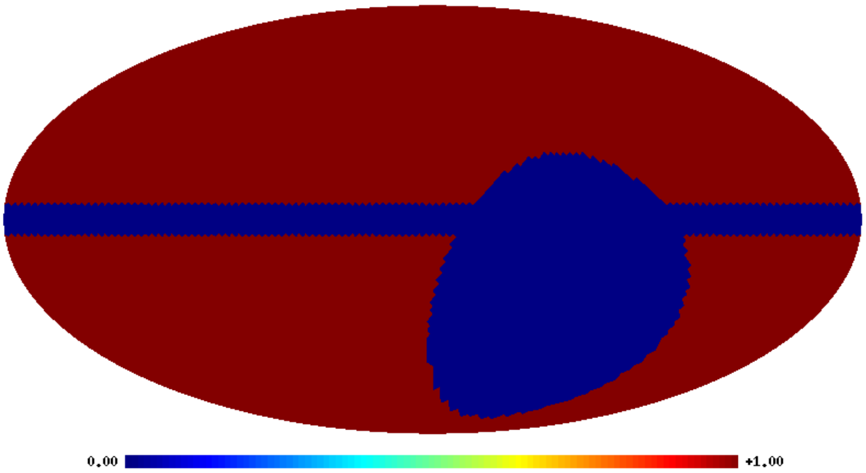

Figure 3.1: A typical sky coverage of a radio galaxy catalogue with declination $\delta > -40^\circ$ and galactic latitude $|b| > 5^\circ$

where, $\overline{RR}$ means the averaged pair counts over a large number of random simulations, and $\overline{DR}$ is the averaged data-random cross pair count for a large number of random simulations. $N_{\rm r}$ denotes the number of sources in the random catalogues. It is necessary to clarify that the simulated random sources R have to be identical for $\overline{RR}$ and $\overline{DR}$ to minimize the statistical uncertainty. Under the assumption that higher order correlations among galaxies can be ignored, the Landy and Szalay estimator has a "Poisson error"

$$\delta w_{\rm LS}(\theta) = \frac{1}{\sqrt{DD}} \frac{1 + w_{\rm LS}(\theta)}{1 + w_\Omega}, \tag{3.17}$$

where w_Ω is the mean of the two-point correlation function over the sampling geometry,

$$w_\Omega = \int_\Omega G_p(\theta) w(\theta) {\rm d}\Omega \ , \tag{3.18}$$

where $G_p(\theta) = \langle \delta\Omega \rangle / \Omega$ is a dimensionless geometric form factor which is equal to the fraction of unique cell pairs separated by distance $\theta \pm {\rm d}\theta/2$ [56].

For a typical ground based radio survey in the north hemisphere of earth, the survey can not fully cover the whole sky and the galactic plane need to be cutoff, whose boundaries are shown in Fig. 3.1. We evaluate $G_p(\theta)$ in such boundary condition in Fig. 3.2. This result do not significant deviate from the full sky dimensionless geometric form factor $G_p^{\rm full}(\theta) = \sin\theta\delta\theta/2$. Since the variance of angular two point correlation is proportion to $1/G_p(\theta)$, the $G_p(\theta)$ curve in Fig. 3.2 indicates that the angular two

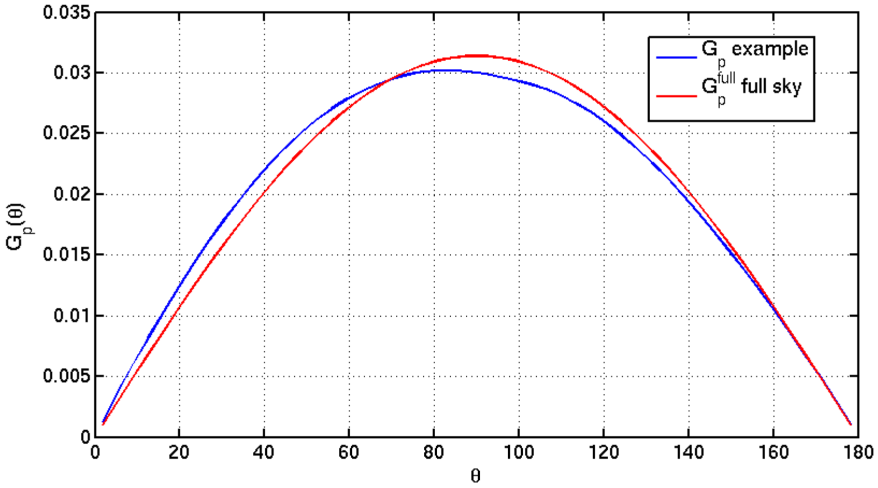

Figure 3.2: Dimensionless geometric form factor $G_p(\theta)$ of catalogues with sky coverage identical to Fig. 3.1

point correlation is most sensitive to the angular separation around 80° in such survey coverage.

3.3 Radio Dipole Correction

The radio dipole signal is believed to result dominantly from our peculiar motion [57] with respect to the cosmic rest frame of radio galaxies, due to the fact that the mean redshift of radio galaxies is above one. If this rest frame is the same as the CMB rest frame, then the dipole measured in the radio catalog should agree with the CMB dipole measured by WMAP and Planck [58, 59]. Previous studies [60, 61, 62, 63] measured the radio dipole for the NVSS catalog. It is actually significantly bigger than expected, by a factor of two to four, depending on the details of the analysis [60, 61, 62, 63]. A compatible excess dipole has been found from the Westerbork Northern Sky Survey(WENSS) catalogue [63], which observed the sky of a different frequency. The origin of this dipole excess is currently unknown. One possibility might be that it is a combination of local large scale structure [64] and a kinetic component due to Doppler shift and aberration.

A local structure dipole, as well as the kinetic dipole, violate the assumption of statistical isotropy that is implicit in the way how we estimate $w(\theta)$. The standard dipole subtraction approach for pixelized maps is relatively straightforward. First, one evaluates the dipole amplitude and direction through a linear dipole estimator on the pixelized map. Then one subtracts the measured dipole contributions at each pixel. However, we do not use the pixelized map to measure the correlation function, but rather extract it using the measured positions of all radio sources outside the mask. In order to do so, we have to include the effect of a dipole into the Landy-Szalay estimator.

Thus we simulate random catalogues which include the measured dipole, denoted by R_d below, and employ the following estimator,

$$w_\mathrm{LS}^\mathrm{d}(\theta) = \frac{N_\mathrm{r}(N_\mathrm{r}+1)}{N(N+1)}\frac{DD}{\overline{RR}} - N(N_\mathrm{r}+1)\frac{\overline{DR_\mathrm{d}}}{\overline{RR}} + \frac{\overline{R_\mathrm{d}R_\mathrm{d}}}{\overline{RR}}. \tag{3.19}$$

The dipole simulations R_d are achieved by the following procedures: First, we assign a uniform random number t to each simulated object, then modify this number based on the angular separation θ between the object and the dipole direction,

$$t = \mathrm{Random}[0,1) + \frac{d}{2}\cos\theta \ . \tag{3.20}$$

Then we add the objects with $t \geq 0.5$ to the R_d catalogue and drop the others. Each random catalogue contains $N_\mathrm{r} = 10^6$ objects and we average over 10 such catalogues.

The dipole modified estimator (3.19) makes use of the full position information of the sources and by simulating a large amount of random catalogues, we minimize the uncertainty in $w_\mathrm{LS}^\mathrm{d}(\theta)$. The computational load is the only disadvantage of this procedure.

Chapter 4

NVSS Angular Power Spectrum and two-point Correlation

4.1 The NVSS Catalogue

The NRAO VLA Sky Survey [10] used the D and DnC antenna configurations of the Very Large Array (VLA). The survey was carried out between 1993 and 1997. Continuum intensity and linear polarization images at 1.4 GHz have been obtained, covering the whole northern and part of the southern sky at declinations $\delta > -40^\circ$. The D configuration of the VLA was used to cover the sky from $\delta = -10^\circ$ to $\delta = 78^\circ$, the rest was filled in by means of the DnC configuration. The obtained images have on average FWHM resolution $\theta_{\mathrm{FWHM}} = 45''$, which is significantly larger than the median angular size of faint extragalactic sources (around $10''$). This survey design sacrifices resolution to achieve high surface brightness, which is needed to achieve flux-limit completeness.

Since the NVSS point-source response is much larger than the median angular size of extragalactic sources, most of the information on the NVSS total intensity images is well represented by elliptical Gaussian fits. The fitted parameters formed the NVSS catalog of sources (not all of them are individual sources). The NVSS catalogue contains almost 2 million discrete sources with flux density above 2.5 mJy. Below we use the source positions in right ascension α and declination δ, the integrated flux density S, as well as their errors.

The NVSS catalogue contains several artificial effects [65]: First, the catalogue shows a configuration effect, which is easily seen in figure 4.1 as steps in surface density

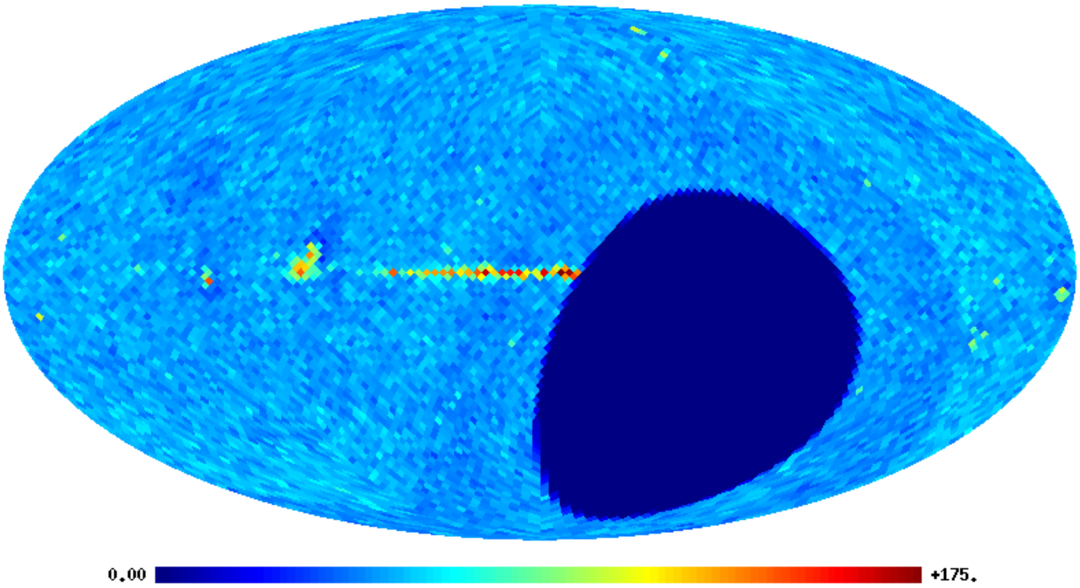

Figure 4.1: Surface density σ of the NVSS source catalog in galactic coordinates in Mollweide projection, shown at HEALPIX resolution $Nside = 32$. The color bar shows the surface density in units of number of objects per square degree. Here we include all objects contained in the catalogue.

at $\delta \sim 78^\circ$ and $\delta \sim -10^\circ$, which are the borders between the D and DnC configurations on the map. Secondly, the side lobes of the bright sources can obscure the presence of weak nearby sources. They are not completely removed by cleaning. The NVSS local dynamic range of the total intensity images is about 1000 to one. Thus, sources closer than about 0.6° to a bright source of flux density S and fainter than $10^{-3}S$ may only be caused by side lobes [10].

Besides these two unphysical effects, there is also a foreground of point sources mainly from the Milky Way (see figure 4.1) and smooth components of radiation from the galaxy itself. These contaminations can influence the VLA noise temperature, and further change the completeness in certain areas on the sky.

All these effects need to be treated carefully, otherwise the statistical analysis based on the contaminated map will be biased. Here we choose to apply a lower flux density threshold and to mask the catalogue to address these issues.

4.2 Lower Flux Density Threshold

Two different VLA configurations (D and DnC) have been used to compile the NVSS catalogue. The VLA C configuration is less compact and thus has a better resolution of $15''$, compared to $45''$ of the D configuration. The DnC configuration is a hybrid configuration in which the antennas on the east and west arms are in D configuration, but those on the north arm are in C configuration to enhance their view of sources at low elevation. Using the DnC configuration changes the synthesized beam and the resolution of declination with respect to the D configuration. This shifts the brightness sensitivity and completeness between the parts of sky observed with different configurations.

The source catalog is derived from intensity images, therefore it is brightness sensitivity limited. Apparently, the D configuration has higher brightness sensitivity than the DnC configuration. Thus one expects to obtain a more complete catalogue for the part of the sky observed by means of the D configuration.

The completeness shift of the DnC configuration sky w.r.t. the D configuration sky can be considered as a faint source selection based on the position angle, noise, confusion and cataloging procedures. It is not clear whether this selection may further introduce a tension in source distribution between the two parts of the sky. Therefore, it is safe to either use one configuration alone (which would reduce the sky coverage by an significant amount), or to choose a higher flux density threshold for the cosmological analysis (which reduces the source density and increases the shot noise).

[66] argue that this configuration effect is only significant at flux densities $S < 10$ mJy. In figure 4.2 we plot the surface density fluctuation, $\Delta\sigma/\overline{\sigma} = \sigma/\overline{\sigma} - 1$, as a function of declination. The dependence of the surface density fluctuation on declination resembles the theoretical rms noise level of the NVSS catalogue [10], which is further discussed in discussion 5.2. One can see that the declination dependence of the surface density is less than 2.5% and the mean value of the DnC configuration is clearly lower than that of the D configuration. This configuration effect is more pronounced at lower thresholds.

This finding is also supported by a χ^2-analysis testing for deviations from isotropy in declination

$$\chi^2 \equiv \sum_{i=1}^{N_{\rm bin}} \frac{\left(\frac{\Delta\sigma_i}{\bar{\sigma}}\right)^2}{\left(\delta\left[\frac{\Delta\sigma}{\bar{\sigma}}\right]_i\right)^2} = \sum_{i=1}^{N_{\rm bin}} \Omega_i \frac{(\Delta\sigma_i)^2}{\sigma_i}, \tag{4.1}$$

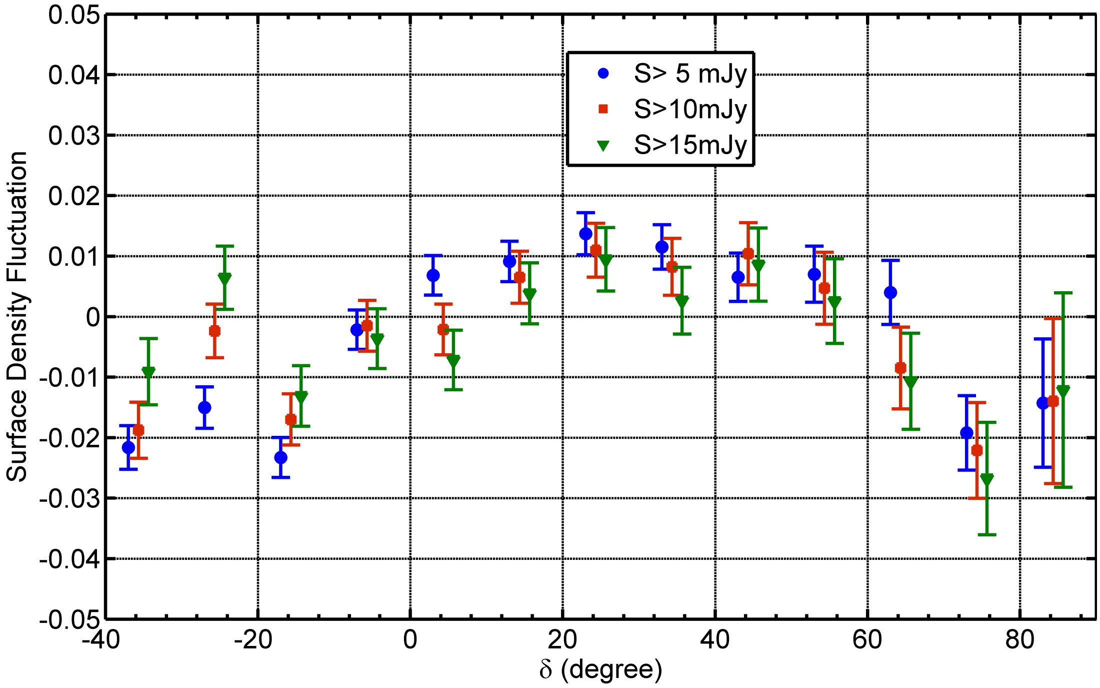

Figure 4.2: Surface density fluctuation, $\Delta\sigma/\overline{\sigma}$, of the NVSS catalogue as a function of declination for several flux density thresholds. The error bars assume Poisson distributed source counts and we mask the region $|b| \leq 5°$. For clarity, the horizontal positions of the $S > 5$ mJy and $S > 15$ mJy data points are slightly offset.

where Ω_i denotes the solid angle of the ith declination strip. The results of this test are shown in table 4.1.

In this work, we choose flux density thresholds of 15 mJy and 25 mJy for cosmological analysis for following the reasons: The study of the the configuration effect suggests that there is a significant dependence on declination. As it is shown above, a flux density threshold of 15 mJy or 25 mJy reduces the value of χ^2 dramatically compared to the situation with lower thresholds. As we do not expect a perfect agreement with isotropy, it is not justified to rise the threshold even higher.

$S >$	5 mJy	10 mJy	15 mJy	25 mJy
χ^2	160.1	59.7	30.7	21.5

Table 4.1: χ^2-values testing for the isotropy in declination of the NVSS surface density (here with 13 degrees of freedom).

Our choice is supported by studies of the cosmic radio dipole from NVSS, which is one to two orders of magnitudes larger than the higher multipole moments. The previous NVSS dipole measurements show that for thresholds below 15 mJy, the dipole direction differs significantly from the CMB dipole direction, and the reduced χ^2 of the quadratic dipole estimator increases significantly [60, 62, 63, 67].

No cut-off at high flux densities is introduced as there is only a small number of sources at high flux densities and thus they play a subdominant role only. We also expect them to be less affected by calibration systematics.

4.3 Masking Strategy

Nevertheless, we have to mask regions around the brightest sources in order to minimize contamination from their side lobes. In the analysis of [65] all sources above 2.5 Jy have been masked by a disk with a radius of 0.6°. However, not all side lobes appear as spurious entries in the catalog, a uniform masking strategy will erase all the information from bright sources, since all sources above the cut threshold are masked. In [66] a list of 22 masks around bright galaxies was compiled based on a visual inspection of the survey.

Here, we introduce an automatic bright source selection method. We count the number of nearby (within 0.6°) sources with $S > 15$ mJy of the brightest sources whose flux densities are $S > 2.5$ Jy. The corresponding histogram is shown in Fig. 4.3.

We assume that the number of sources in a fixed solid angle follows a Poisson distribution, and use the so-called Poissonness plot [68] to identify the histogram bins that are significantly deviate from a Poisson distribution, where we assume that such a deviation is caused by the side lobe contamination of bright sources. The idea of the plot is to consider a simple variable substitution, which transforms the exponential Poisson distribution function to a linear function. We find that 49 sources fail the Poissonness test at the 99% confidence level (Fig. 4.4). It is worth clarifying that 'clean' regions containing bright sources that by chance contain the same amount of sources as 'dirty' regions are also excluded. We also verify that for most of the bright sources the nearby source count histogram is in good agreement with the histogram of randomly picked nearby source counts, which justifies the inclusion of many of the bright sources in our analysis.

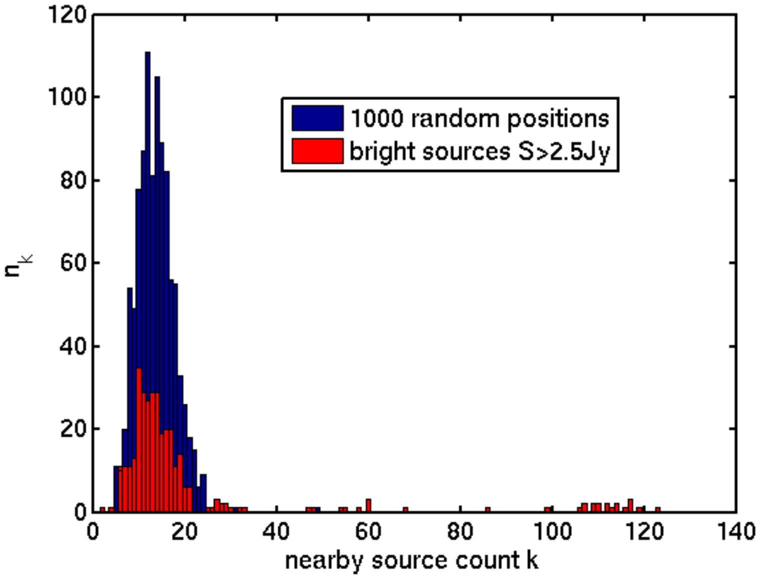

Figure 4.3: Nearby source count histogram (disks with radius 0.6°). The red bins correspond to nearby source counts around bright radio galaxies with $S > 2.5$ Jy. The blue bins correspond to 1000 randomly picked positions outside the galactic plane ($|b| > 5°$). The maximum of randomly picked counts results in 49 neraby sources.

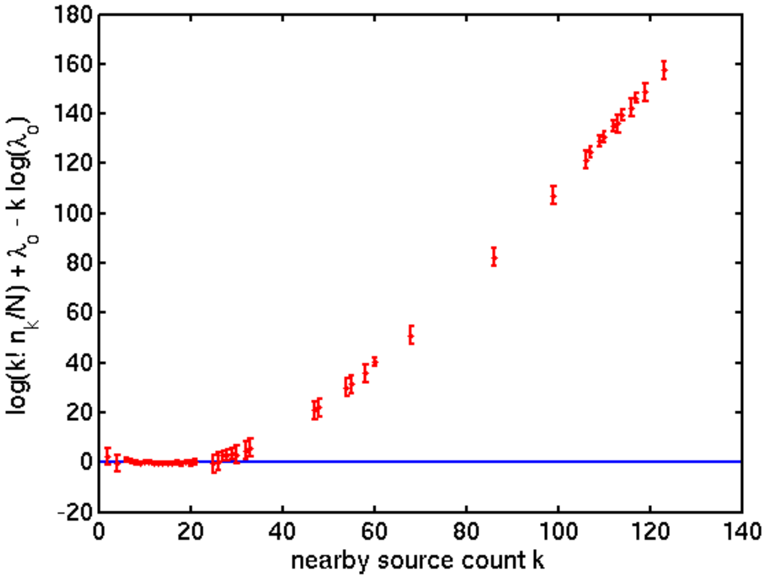

Figure 4.4: Poissonness plot of the nearby source counts. λ_o is the mean nearby count over the survey area. N is the total number of sources with $S > 2.5$ Jy. The solid horizontal line corresponds to a perfectly Possion distributed nearby source count. The error bars denote the 99% confidence levels.

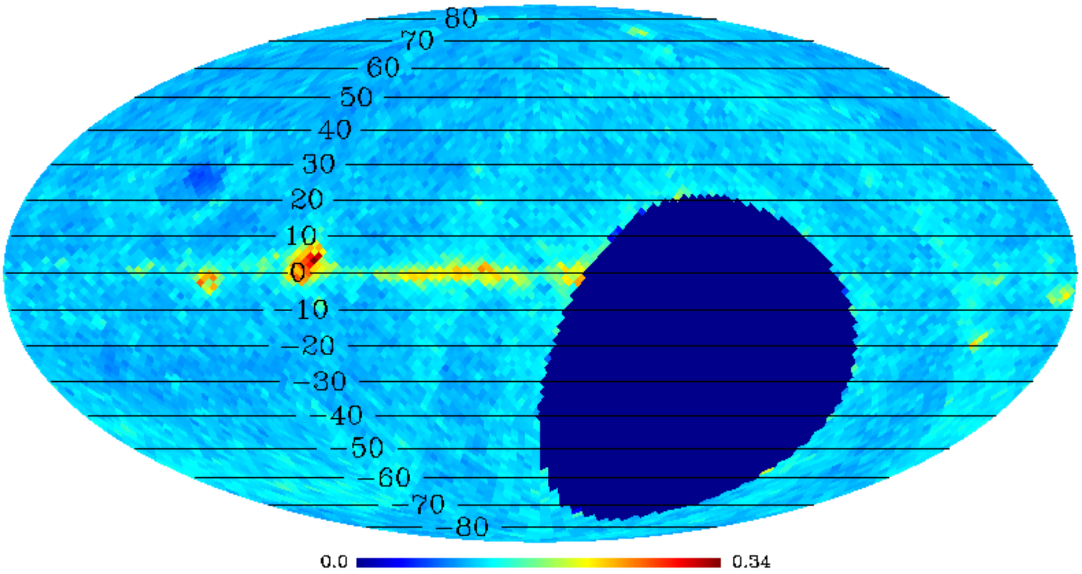

Figure 4.5: NVSS position uncertainty map, relative to the mean beam width $\theta_{\mathrm{FWHM}} = 45''$.

Let us now turn to the issue of noise and confusion. According to [10], the rms position uncertainty σ_{pos} is,

$$\sigma_{\mathrm{pos}} \propto \frac{\sigma_{\mathrm{b}}\theta_{\mathrm{FWHM}}}{2S_{\mathrm{p}}}, \tag{4.2}$$

where S_{p} is the peak flux density, σ_{b} is the rms brightness fluctuation (noise and confusion). Our idea is to use σ_p to trace σ_{b}. [10] point out that for flux densities below 15 mJy, the rms position uncertainty is dominated by noise. Accordingly, we create a position uncertainty map (Fig. 4.5) by averaging the position uncertainties

$$\sigma_\theta \equiv \sqrt{\frac{\sigma_\delta\sigma_\alpha}{\theta^2_{\mathrm{FWHM}}}\sin(\frac{\pi}{2} - \delta)} \tag{4.3}$$

for all point sources in a pixel whose flux density is smaller than 15 mJy. Note that the dominant sources are those with low flux density. The map is constructed using the HEALPIX package with the pixel size fixed by $Nside = 32$.

The resulting position uncertainty map is shown in Fig. 4.5. One sees clearly that the position uncertainty follows the theoretical rms noise level which, outside of the

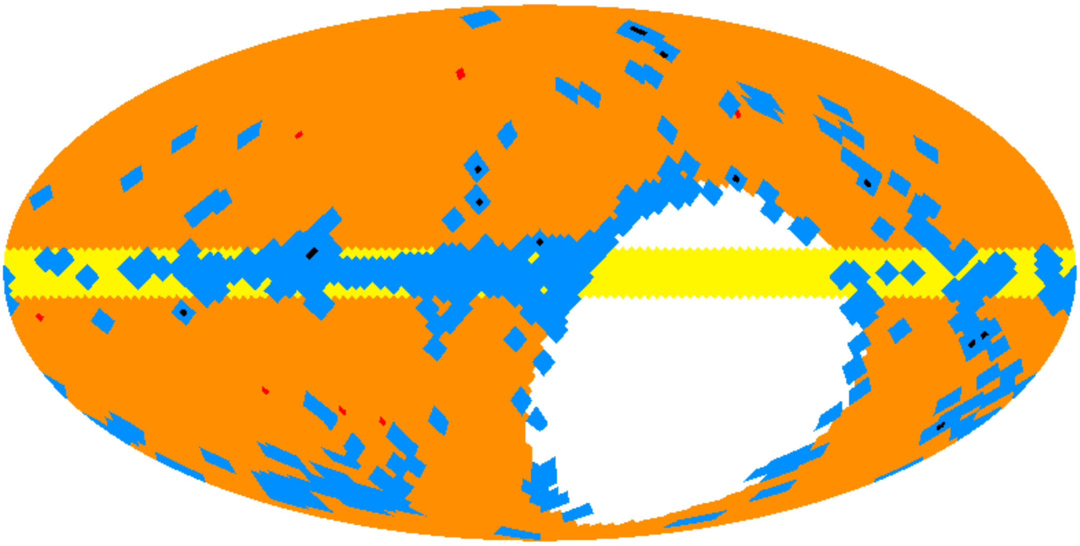

Figure 4.6: NVSS65 mask. The orange region makes up 64.7% of the sky. Yellow pixels are close to the galactic plane $|b| \leq 5°$ and are excluded to suppress galactic point sources and foregrounds. Blue pixels are excluded due to large position errors. Red and black pixels contain bright sources with significant side lobe effects, black pixels additionally overlap with pixels with high position error.

galactic plane, increases away from the zenith due to pickup of ground radiation, atmospheric emission, ionospheric effects and uv-projection. The galactic plane and nearby nebulas are also easy to identify. We further employ a 5% pixel cutoff for the pixels with highest $\sigma_\theta > 0.132$. In addition, we also mask galactic radio sources by excluding all sources with galactic latitude $|b| \leq 5°$.

To sum up, at 15 mJy and 25 mJy thresholds we mask all pixels in the neighborhood of 49 selected bright sources. Additional pixels and their neighborhood with highest mean position uncertainty σ_Ω and galactic sources with $|b| \leq 5°$ are masked as well. In the following we call this the NVSS65 mask[1]. It is shown in Fig. 4.6. In total, there is approximately 64.7% sky left. The total number of objects after applying the NVSS65 mask at 15 and 25 mJy is shown in Table 4.3.

---

[1] At the moment the NVSS65 mask is available at https://github.com/phychensong/NVSS.

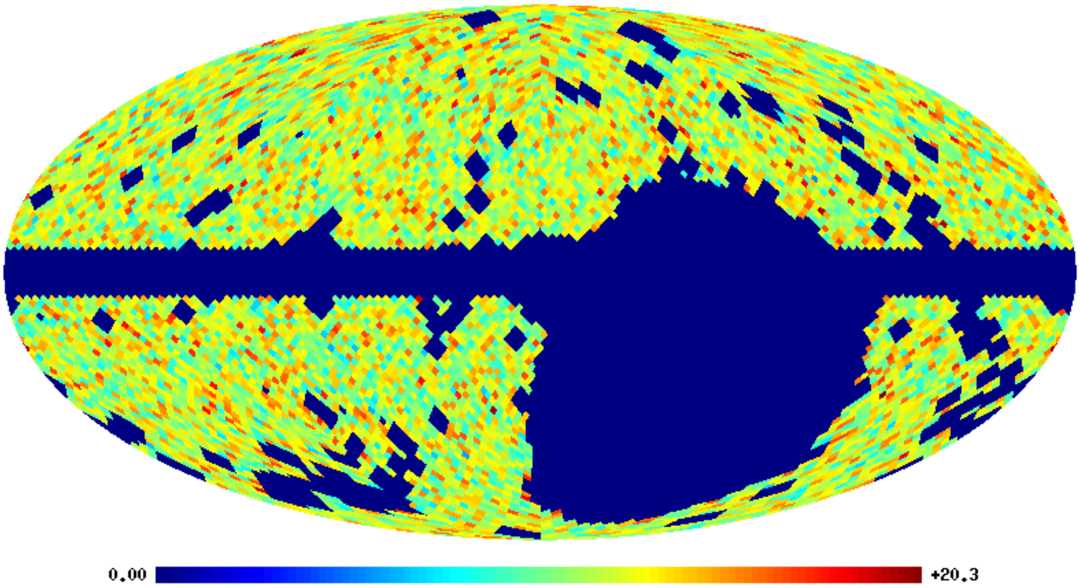

Figure 4.7: Surface density of the NVSS source catalog for a flux density threshold of $S > 15$ mJy and applying the NVSS65 mask, shown in galactic coordinates at pixel size *Nside*=32. The color bar shows the surface density σ in units of number of objects per square degree.

4.4 Theoretical Expectation

The expected C_l for the NVSS catalog are obtained using a modified version of the CLASS package [69]. The parameters for the best-fit cosmological model are taken from [23]. For the theoretical prediction of the angular two-point correlation we cut the Legendre series at $l_{\max} = 900$. We convinced ourselves that this cut-off is large enough to ensure numerical convergence of $w(\theta)$ at all angular scales considered in this work.

We use the Combined EIS-NVSS Survey Of Radio Sources (CENSORS) [70] to model the redshift distribution of the NVSS catalogue. CENSORS contains all NVSS sources above 7.2 mJy that are within a patch of 6 deg^2 in the ESO Imaging Survey (EIS). Following [71], we choose the gamma function redshift distribution,

$$\frac{\mathrm{d}\bar{\sigma}}{\mathrm{d}z} = \mathcal{N} \left(\frac{z}{z_0}\right)^{\beta} \exp\left(-\beta \frac{z}{z_0}\right) , \tag{4.4}$$

with $\mathcal{N}$ denoting a normalization factor that is irrelevant for the final result and the best-fit parameters to CENSORS data given by $z_0 = 0.53^{+0.11}_{-0.13}$ and $\beta = 0.81^{+0.34}_{-0.32}$. These numbers should however be treated with care as the redshift distribution is based on 149 galaxies only.

For the radio galaxy, the simplest constant bias is not a good approximation, in which case the evolution effect can not be neglected. In principle, this bias depends on the halo mass and it is a nonlinear and stochastic function of the underling dark matter density field[72, 73]. The recently developed halo models are in reasonable agreement with what is measured in numerical simulations with Gaussian initial conditions[74].

In this thesis, we use the Gaussian bias model[75], where the bias of one specific radio galaxy survey is given by a mass weighted integral

$$b(z) = \frac{\int_{M_{\rm min}}^{\infty} {\rm d}M b_{\rm H}(M,z) M n(M,z)}{\int_{M_{\rm min}}^{\infty} {\rm d}M M n(M,z)} \quad , \tag{4.5}$$

where $n(M,z)$ is the halo mass function, and $b_{\rm H}(M,z)$ is the corresponding halo bias function. Following [73], we adopted the modified Press-Schechter mass function

$$n(M,z) = -\frac{2A_{\rm n}}{\sqrt{\pi}} \frac{\bar{\rho}}{M^2} \frac{{\rm d}\ln\sigma_M}{{\rm d}\ln M} (1 + \frac{1}{(\beta\nu)^{\gamma}}) \sqrt{\frac{\beta\nu}{2}} e^{-\beta\nu/2} \quad , \tag{4.6}$$

where $\nu \equiv [\delta_c(z)/\sigma_M]$ and $\delta_c(z)$ is the critical density, above which the perturbations rapidly develop into bound objects. σ_M denote the rms of the density contrast. $\beta = 0.75$, $\gamma = 0.3$ are fitted to numerical simulations[76], and $A_{\rm n}$ is the normalization parameter,

$$\frac{1}{A_{\rm n}} \equiv \int_0^{\infty} \frac{{\rm d}\nu}{\nu} (1 + \frac{1}{(\beta\nu)^{\gamma}}) \sqrt{\frac{\beta\nu}{2}} e^{-\beta\nu/2} \quad . \tag{4.7}$$

This mass function is more consistent with simulations than the Press-Schechter mass function and the mass function computed using the Zeldovich approximation[77], and it reduces to the original Press-Schechter function for $\beta = 1$, $\gamma = 0$ and $A_{\rm n} = 1$. Using this mass function and following [72, 73], the halo bias function becomes

$$b_{\rm H}(M,z) = 1 + \frac{\beta\nu - 1}{\delta_c(z)} + \frac{2\gamma/\delta_c(z)}{1 + (\beta\nu)^{\gamma}} \quad . \tag{4.8}$$

Since $\beta < 1$, the massive halos are slightly less biased than the original Press-Schechter based formula results. For the less massive halos, this bias function shows more positive bias due to the extra term.

The Gaussian bias model strongly depends on the $M_{\rm min}$ as shown in Eq. 4.5. Following [78] for the radio galaxy survey like NVSS, we choose $M_{\rm min}$ equal to $10^{12.67}\ M_{\odot}$.

	N	d	α	δ
$S > 10$ mJy	436,733	1.32×10^{-2}	142.70°	30.47°
$S > 15$ mJy	314,594	1.44×10^{-2}	153.44°	−5.53°
$S > 25$ mJy	200,092	1.83×10^{-2}	157.12°	−15.10°
expected		0.46×10^{-2}	168°	−7°

Table 4.2: NVSS dipole for various flux density thresholds, measured by means of Healpix at resolution $Nside = 32$ after applying the NVSS65 mask. For comparison we quote the expected kinetic dipole for NVSS radio sources, based on the observed CMB dipole.

The full radio galaxy bias function can be approximated to a second order polynomial of redshift as,

$$b(z) = 0.9\left[1 + 0.54(1+z)^2\right]. \tag{4.9}$$

Utilizing Healpix, we find the radio dipole of the NVSS catalogue after masking with NVSS65 and as shown in table 4.2. The estimated dipole at our chosen flux density thresholds and sky coverage agrees with the estimates from the literature (see e.g. [67] for a recent summary).

In this study, we compare the results without and with dipole subtraction. We either subtract the measured radio dipole (see table 4.2) or the CMB predicted radio dipole. The dipole contribution in the angular two-point correlation function can be seen from Fig. 4.8. We find that the dipole has a significant effect and actually dominates the two-point correlation function at large angular scales above $\sim 10^\circ$. In the figure we account for the measured dipole. Considering just the CMB predicted dipole reduces the large angle correlation, but leaves us with a residual dipole that could be due to a local structure and is hard to predict without a much more detailed study. We therefore decide to correct for the measured NVSS radio dipole and suppress the (structure) dipole also in the theoretical prediction.

4.5 Results

We adopt the dipole subtracted Landy-Szalay estimator to measure the angular two-point correlations of the NVSS catalogue with thresholds 15 mJy and 25 mJy for two different masks (NVSS65 and a constant latitude cut of the galactic plane).

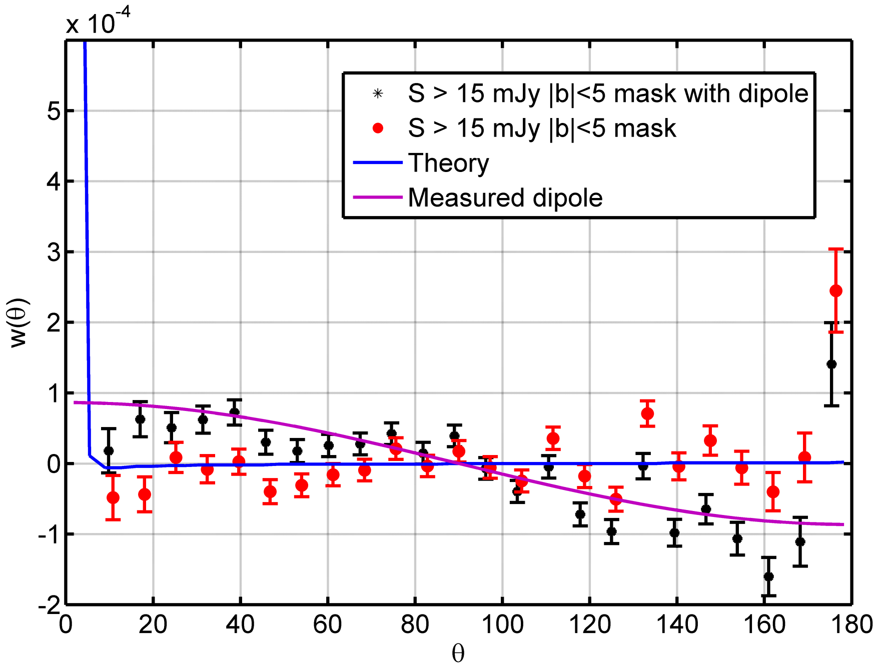

Figure 4.8: NVSS angular two-point correlations for a 5° galactic latitude mask with and without dipole correction.

The results agree with our expectation. After masking of the high rms noise and confusion pixels by means of the NVSS65 mask, the two-point correlation turns out to be less scattered, as shown in Fig. 4.9. For the simpler constant latitude cut, one can see that the first data point at $\sim 4^\circ$ is above the plot range of the figure. The NVSS65 mask efficiently reduces the amount of correlation at scales of a few degrees and brings the measurement in agreement with the theoretical expectation of the best-fit cosmological model. One can also observe a better agreement of the 15 and 25 mJy thresholded data sets after the mask NVSS65 has been applied. These findings are confirmed by the χ^2-values shown in Table 4.3. We infer that the new NVSS65 mask efficiently pushes the data points towards the theoretical prediction.

One can also see from Fig. 4.9 that the measurement using the NVSS65 mask agrees with the theoretical prediction until $\theta \sim 90^\circ$. Above that angular scale the data appear to be more noisy. Surprising are some quite large correlations at the largest angular scales close to 180°.

For angular scale between 1° and 20°, the 65% sky coverage guarantees that the $w(\theta)$ estimator is averaged over a large number of independent sky patches. Artificial

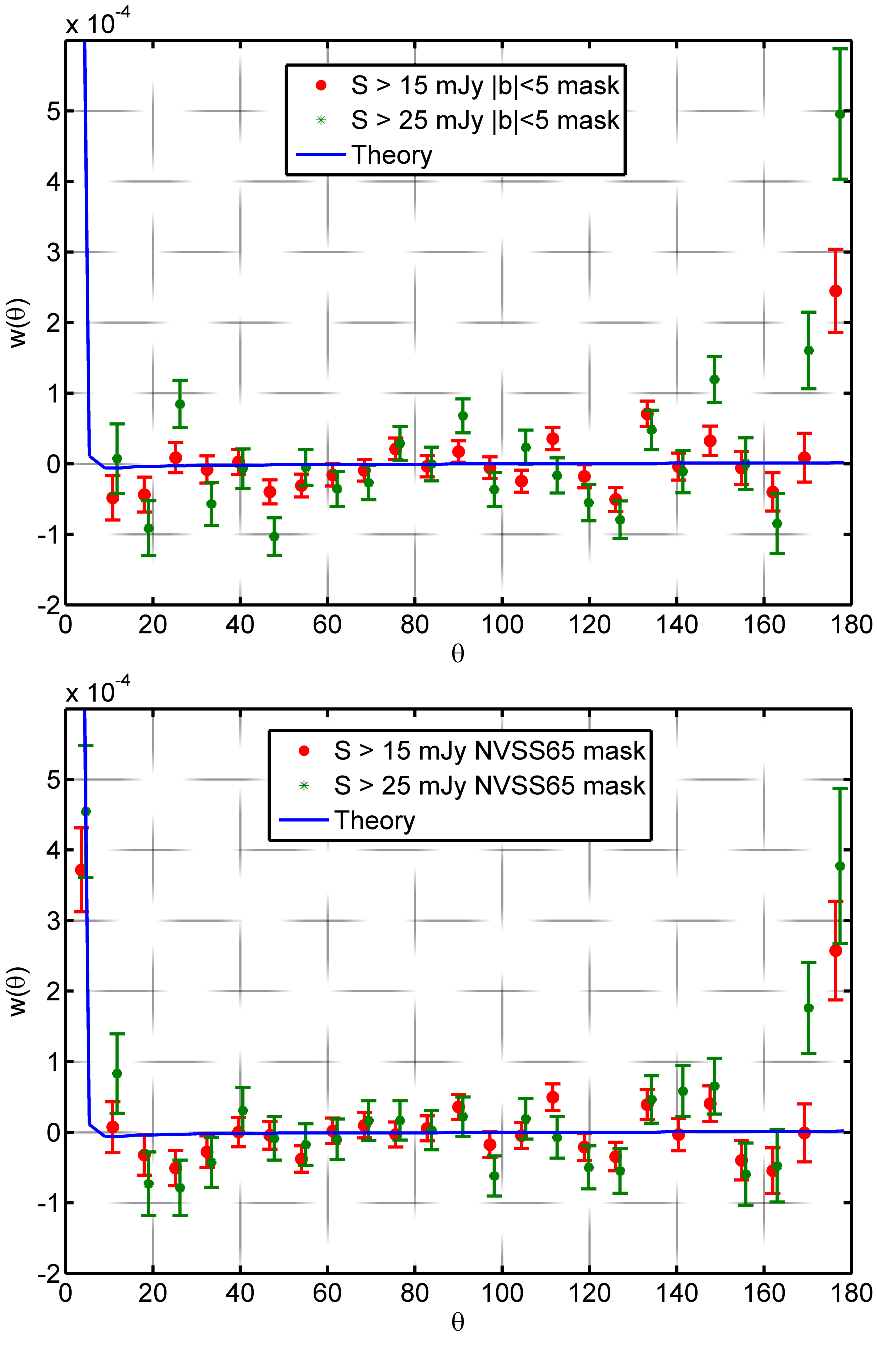

Figure 4.9: Angular two-point correlation function $w(\theta)$ from 5° galactic latitude cut (top panel) and the NVSS65 mask (bottom panel). In both cases we include a dipole correction.

	$\lvert b\rvert < 5^{o}$		NVSS65	
	N	χ^2	N	χ^2
$S > 15$ mJy	377,739	165.96	322,557	94.08
$S > 25$ mJy	240,872	222.49	205,103	99.80

Table 4.3: χ^2-test for $w(\theta)$ for 49 data points [excluding first bin: $0 < \theta < 3.6°$]. Note: We neglect the correlation between the data points.

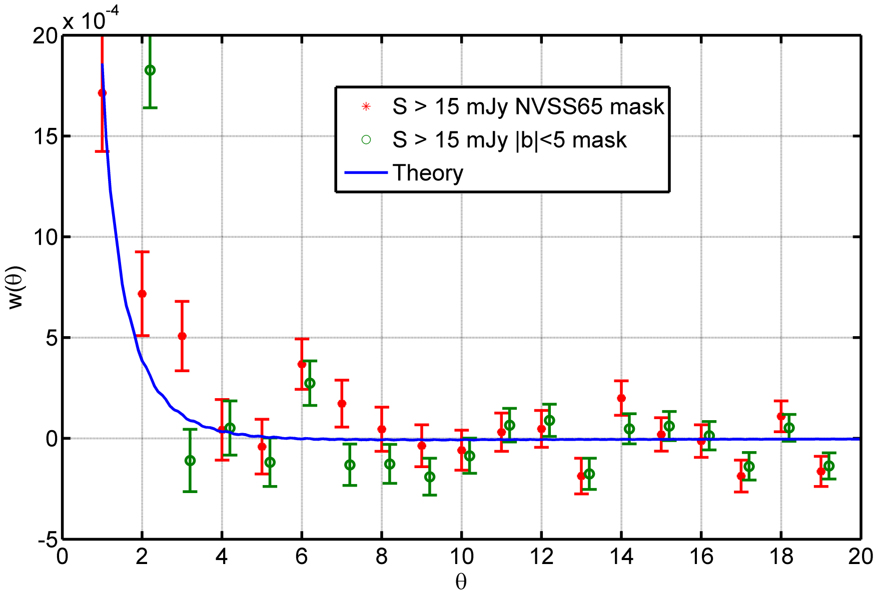

Figure 4.10: Angular two-point correlation function at $1° < \theta < 20°$ from the NVSS catalogue with dipole correction for two different masks.

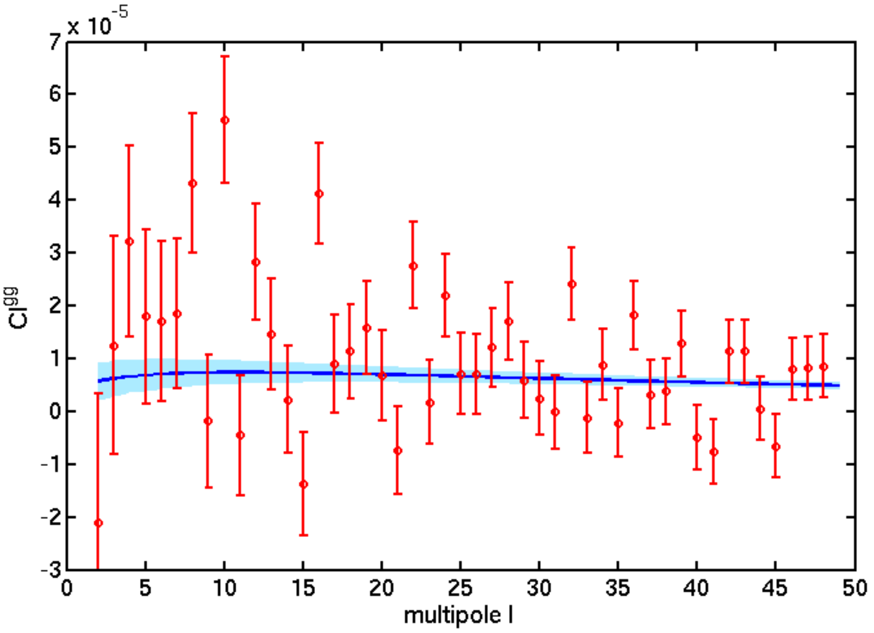

Figure 4.11: NVSS angular power spectrum C_l for $S > 15$ mJy, dipole corrected and NVSS65 mask. C_l is evaluated via a Legendre transformation from the angular two-point correlation function. The solid line and the band around it show the theoretical prediction and its cosmic variance.

fluctuations caused by the survey or galactic foreground are suppressed in the average, and side lobes and multi-components source effects are expected to contaminate smaller angular scales (up to 0.6°). In this range, $w(\theta)$ is expected to be consistent with the theoretical prediction.

The result of an analysis at higher angular resolution for $\theta < 20°$ is shown in Fig. 4.10. In order to suppress the shot noise contribution we now focus on the $S > 15$ mJy data set. We find that the NVSS65 mask improves the agreement with theoretical predictions considerably. A discussion of the cosmological consequences is given below.

A complementary analysis to the angular two-point correlation function is to study the angular power spectrum. One way of measuring C_l is to do a Legendre transformation of the angular two-point correlation. The result of that transformation is shown in Fig. 4.11. The fact that many of the C_l turn out to have negative values shows that this measurement is quite noisy. Nevertheless, in the mean the C_l seem to agree well with the theoretical expectations, apart from a hand full of multipoles with even l, most prominently the $l = 10$ mode.

Chapter 5

Discussion

5.1 Cosmological Implications

Let us now turn to the cosmological implications and a discussion of our findings in comparison with previous studies. In the following we focus on the results obtained by means of the NVSS65 mask, including the dipole correction as discussed above and a lower flux threshold of 15 mJy.

A question of interest is the determination of the cosmological parameters of our minimal six-parameter cosmological standard model. For that purpose, the NVSS data alone cannot compete with high fidelity data from the CMB or from optical galaxy redshift surveys. Nevertheless it is interesting to investigate the consistency of the NVSS angular two-point correlation and angular power spectrum with the standard lore.

In Fig 5.1 we compare the NVSS angular two-point correlation with theoretical predictions at angular scales below 9° for different values of the Hubble constant H_0. The extreme values of H_0 are disfavoured, and the Planck best-fit value of $H_0 = 67.8$ km/s/Mpc provides also a good fit to NVSS data. Unfortunately, one can not use it to break the discrepancy with somewhat higher values from local measurements of H_0.

It is important to note, that the redshift distribution function also affects the NVSS angular two-point correlation at this angular scale. As shown in Fig 5.2, the parameter β modifies the slope of the two-point correlation, and the parameter z_0 changes its slope and and angular scale. Our angular two-point correlation measurement seems to prefer low z_0 and β, which is agrees with the results of [71].

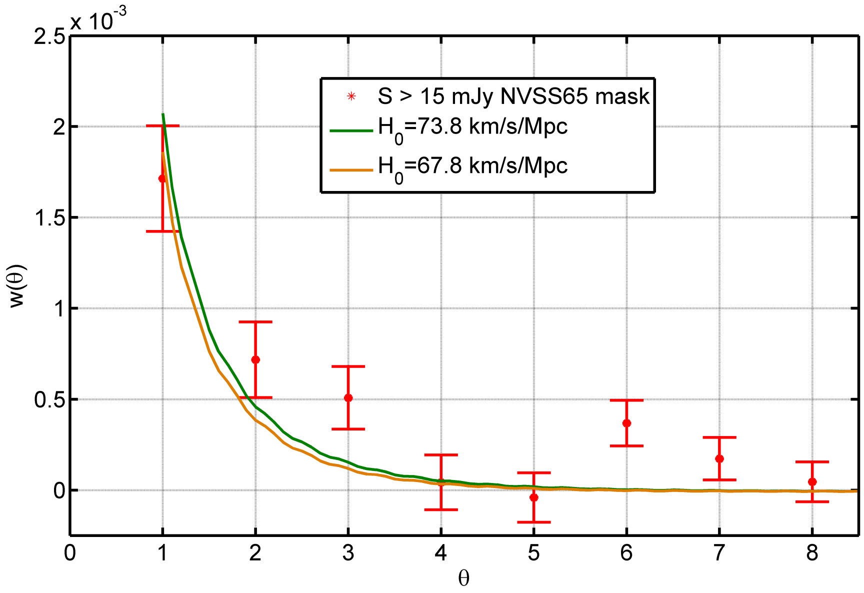

Figure 5.1: Angular two-point correlation function as a test for the Hubble constant H_0. The measurement uses the NVSS65 mask with dipole correction.

Putting those studies together we see a degeneracy of H_0, z_0 and β. The parameters of the bias factor $b(z)$ do also participate in that degeneracy, which limits our ability to use todays radio continuum surveys for cosmological parameter estimation. However, it is an encouraging finding that the completely independent measurements of H_0 (Planck), z_0 and β (CENSORS) give rise to a picture that seems to be fully consistent with $w(\theta)$ from NVSS.

The small angle two-point correlation is also an interesting probe of primordial non-Gaussianity. Previous results [75] claimed evidence for a primordial non-Gaussianity at the 3σ level. $w(\theta)$ is supposed to vanish at around $4°$ if the fluctuations are Gaussian, however their measurement of $w(\theta)$ showed a constant shift from zero at $1° < \theta < 10°$, which they attributed to the effect of a primordial non-Gaussianity. However, adapting our procedure of dipole correction and optimal estimation of $w(\theta)$, we do not see such a shift. Our result thus fully agrees with primordial Gaussianity, as is shown in Fig. 4.10. To turn that into a precise new upper limit on f_{nl} is beyond the scope of this work.

Consistency with Gaussianity is also confirmed by the angular power spectrum shown in Fig. 4.11. A primordial non-Gaussianity would lead to an increase of angular power C_l at small multipoles [75, 79]. Our analysis shows no evidence for such an

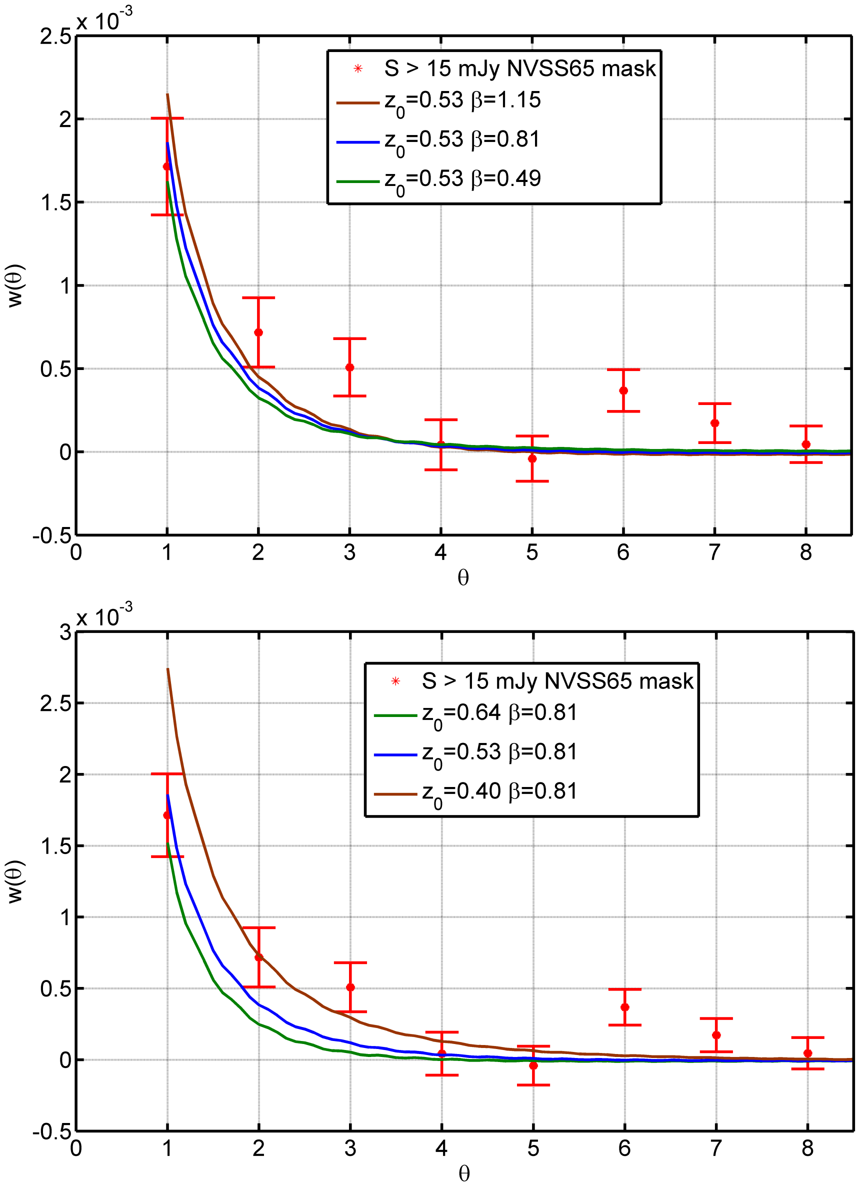

Figure 5.2: Angular two-point correlation function for different redshift distributions.

increase. Note that this contradicts the previous results from [52] and [71]. We tried to understand what is responsible for the removal of the apparent non-Gaussianity, but it turns out that it is impossible to attribute it to a single effect. The dipole changes the low l multipoles as one reconstructs the multipole moments from an incomplete sky, but we verified that the dipole effect alone is not large enough. We also use a slightly higher threshold (15 instead of 10 mJy) in our analysis, which also reduces the direction dependent effects in the NVSS catalogue (see table 4.1). The masking of regions around bright sources appears not to influence the analysis on the largest scales. On the other hand, using the Landy-Szalay estimator compared to suboptimal methods seems to be important. We conclude that the sum of our studies of the systematics of the NVSS catalogue is essential and allows us to get rid of a spurious non-Gaussianity.

5.2 Residual Systematics

The theoretical prediction based on the ΛCDM model suggested $C_l \approx 5 \times 10^{-6}$. Our measurements agree rather well with that prediction, with some exceptions. The quadrupole cannot be detected at any significant level and the power at $l = 10$ is an order of magnitude larger than expected. However, at larger l, up to $l \sim 60$, the C_l are consistent with the theoretical prediction, which is in agreement with previous analysis of the ISW effect [80]. Higher multipole moments are noisy and statistically consistent with zero.

Let us finally discuss the angular scales at $\theta > 20°$ and look in more detail at the corresponding multipole moments up to $l = 10$. For a simple galactic isolatitude cut, we found significantly more power at low multipole moments, with $l = 4$ being the dominant mode (not shown here). The essential step to get rid of this extra power is to take into account direction dependent systematic effects in the NVSS catalogue. Our NVSS65 mask allows us to reduce the $l = 4$ mode and to recover an overall flat angular power spectrum. However, even with the NVSS65 mask, some of the C_ls are one order of magnitude larger than the prediction at $l < 10$. One of the reason could be due to remaining surface density fluctuations at different declinations.

We find a clear anti-correlation between the surface density and the theoretical rms noise of the NVSS catalog, Fig. 5.3. The declination dependence of the theoretical rms noise fluctuations at $-40° < \delta < -10°$ is due to changes in the snapshot integration

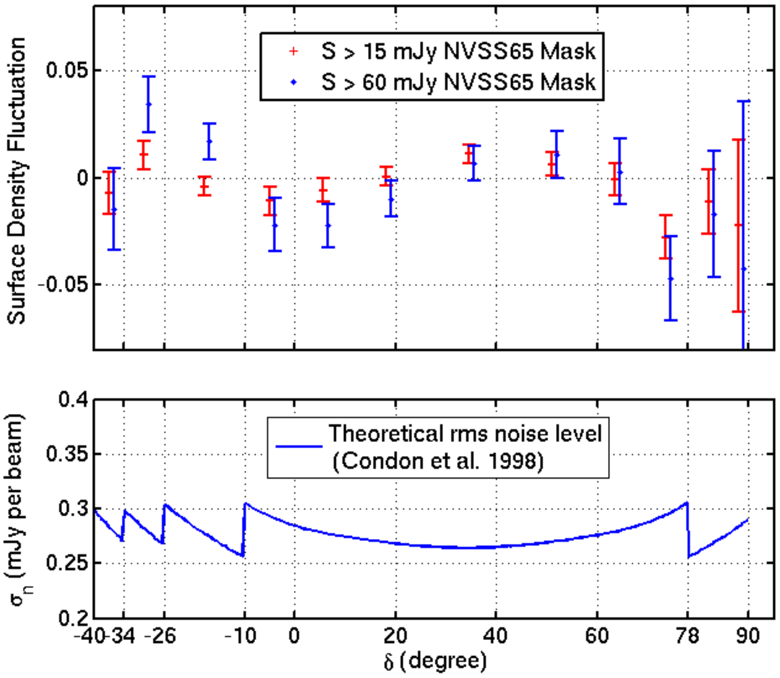

Figure 5.3: Top panel: Surface density fluctuation ($\Delta\sigma/\overline{\sigma}$) of NVSS sources at $S > 60$ mJy and $S > 15$ mJy after applying the NVSS65 mask. Bottom panel: The theoretical rms noise level of the NVSS catalogue from [10]. The VLA geodetic latitude is $34°04'44''$.

time. When the VLA points to the horizon, the effect of the projection of the uv plane, combined with ground and ionospheric noise, decreases the effective signal to noise ratio of the survey. As can be seen in Fig. 5.3 this effect is not limited to the faintest sources, but is also there for brighter sources at $S > 60$ mJy. Thus only the most extreme influence of the direction dependent systematics can be cured by means of a lower flux threshold.

To further probe whether these direction dependent effects affect the low-l multipoles, we investigated the angular pseudo-power spectrum, which are obtained through a decomposition into spherical harmonics on the pixelized galaxy number count. For this we used HEALPIX. In figure 5.4 we show estimates of the pseudo-C_l for two different normalizations. In the first case, we normalize the pixel count with the mean pixel count of the full survey $\bar{n}$, i.e.

$$x_i = \frac{n_i - \bar{n}}{\bar{n}} \ . \tag{5.1}$$

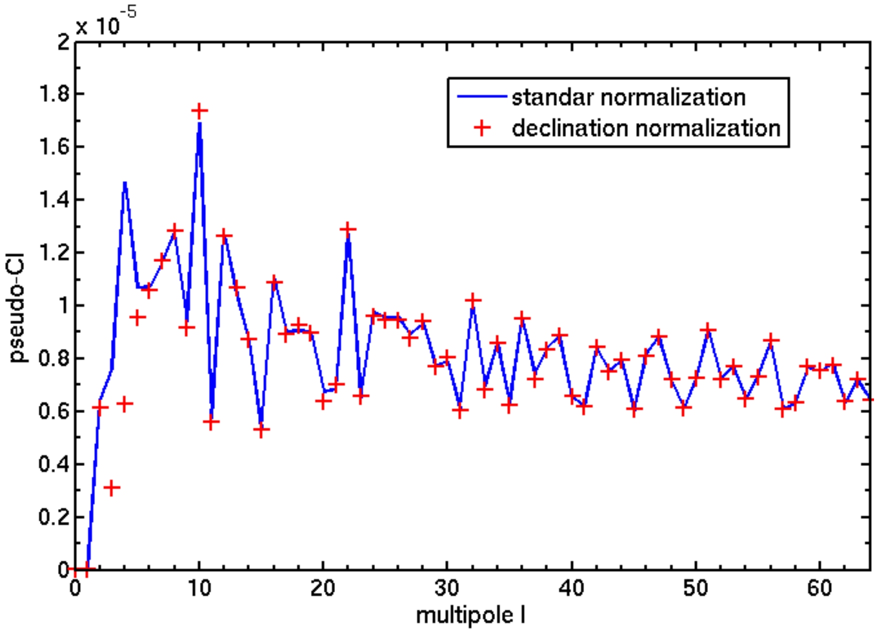

Figure 5.4: The HEALPIX pseudo-C_l of the NVSS catalogue with NVSS65 mask for $S > 15$ mJy and radio dipole subtracted.

The second case is motivated by [81]. We divide the map along the declination, based on durations of the snapshots, and subtract the mean pixel count $\bar{n}_{\delta_i}$ at declination δ_i,

$$x_i = \frac{n_i - \bar{n}_{\delta_i}}{\bar{n}} \ . \tag{5.2}$$

The latter procedure was also used in the Planck analysis of the ISW effect [78, 82].

The second procedure, erases the source density fluctuations along the declination direction. As can be seen in Fig. 5.4, the $l = 3, 4, 5$ multipoles are significantly reduced by the declination mean subtraction, which strongly implies that the $l = 4$ mode fluctuation are caused by the direction dependent noise of the NVSS catalogue. On the other hand, the large $l = 10$ mode is not affected by that normalization at all and it remains unclear why it exceeds the expectation by an order of magnitude. Using this declination normalisation for a cosmological analysis, like [81], [83] or [82], certainly suppresses fluctuations on large scales, but the procedure cannot distinguish direction dependent effects from real fluctuations and it is very hard to assign an error estimate to it.

5.3 Parity Asymmetry

We also found a curious observation. Looking carefully at Fig. 4.11, we observe a parity asymmetry in the C_l: the power of even multipoles $l = 4, 8, 10, 12, 16, 22, 24, 32...$ is higher than that of their odd neighbors. This even parity preference can also be seen from the fact that $w(180°) > 0$. A similar effect was observed in the CMB angular power spectrum, where the parity asymmetry is the opposite [84]. There the odd $l(l+1)C_l/2\pi$ are larger than the even ones, see Fig. 5.5.

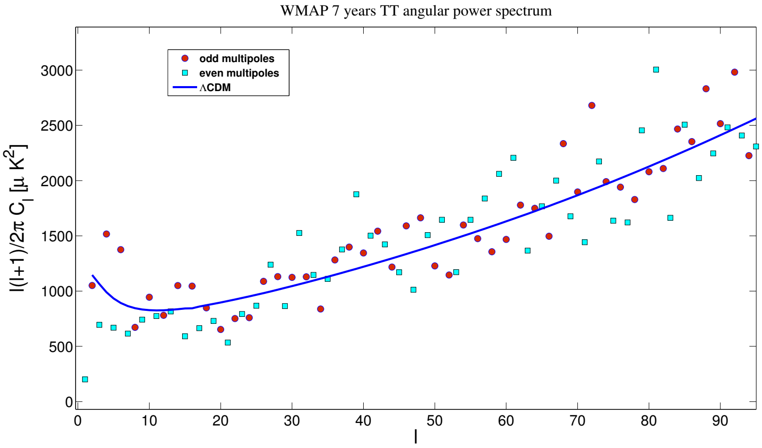

Figure 5.5: WMAP 7-year angular power spectrum - Power spectrum at even multipoles tend to be lower than those at neighboring odd multipoles.

However, this suggests that the two parity asymmetries do not share the same origin (if both of them are real). One possible reason for parity asymmetry is inhomogeneity. Breaking statistical homogeneity cause the observation depends on the observer position. The universe can be even or odd parity preference if an appropriate observer position is chosen.

5.4 Next-to-leading order Effects in the Radio Galaxy Angular Power Spectrum

In the above analysis, we only considered the density perturbations. The next-to-leading order contributions in the galaxy number density fluctuations are the radial

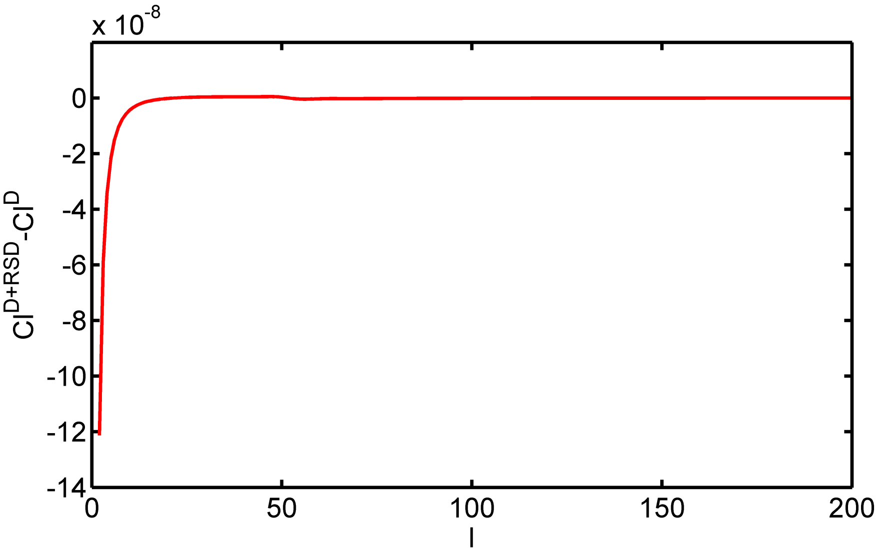

Figure 5.6: The angular power spectrum difference $C_l^{D+RsD} - C_l^D$ with the NVSS redshift distribution and Gaussian bias.

partial derivative of the comoving distance fluctuation $\partial_{r_o}\delta r$ and the gravitational lensing convergence κ [45]. Since we choose redshift space, δr will be dominated by $-\frac{\delta z}{\mathcal{H}}$. In the Newtonian limit, the largest contribution in δz comes from the line of sight peculiar velocity $V_i e^{ri}$. Therefore the radial partial derivative of the comoving distance fluctuation $\partial_{r_o}\delta r$ becomes

$$\partial_{r_o}\delta r \approx -\frac{1}{\mathcal{H}}\frac{\partial V_i e^{ri}}{\partial r_o} \quad . \tag{5.3}$$

This term is called redshift-space distortion and was first derived by Kaiser in 1987 [85]. The angular power spectrum with a redshift-space distortion term $C_l^{\mathrm{D+RsD}}$ is almost the same as the angular power spectrum C_l^D with density alone, the difference is shown in Fig. 5.6. Unlike the redshift space distortion, the lensing effect is very relevant. As shown in Fig. 5.7, the angular power spectrum with lensing effect is decreased by about 30% compared to the angular power spectrum with only density. The lensing contribution is dominated by the cross-correlation between density and the gravitational lensing convergence -2κ from the volume distortion.

Furthermore, since what we really observe are the galaxies above a flux density threshold S_t, rather than all galaxies inside a certain volume, we need to consider the

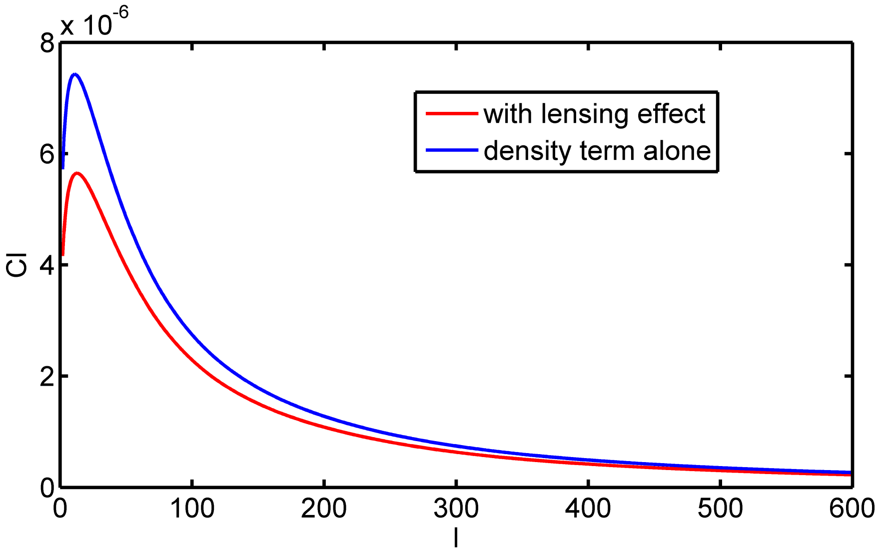

Figure 5.7: The angular power spectrum C_l with and without lensing effect.

luminosity distance fluctuation[86]. For the simplest case, where $\mathrm{d}n_{\mathrm{phy}}/\mathrm{d}L \propto L^{-s}$,

$$n_{\mathrm{phy}} = n_{\mathrm{phy}}(> L_t)(1 - 2(s-1)\delta_d) \quad , \tag{5.4}$$

where L_t is the specific luminosity threshold $L_t \equiv 4\pi(1+z)^{\alpha+1}R_{\mathrm{o}}^2 S_t$. The dominant effect inside δ_d is the gravitational lensing convergence $-\kappa_g$, see Eq. 2.66. Thus, the total lensing contribution is $2(s-2)\kappa_g$. For the double power-law luminosity function, when L_t is in the bright tail, the slope s is close to 2 and the lensing effect is maximally suppressed. However, when L_t is in the faint region, the slope s is close to 0 and the lensing effect is amplified.

Our results are obtained with a modified version of the CLASSgal code[69]. The previous code is designed for the redshift galaxy survey, in which the selection function is not suit for the continuum survey. We introduce a new type of selection function called "continuum", which is unit through redshift $0 < z < 2.9$. Considering the shape of the NVSS redshift distribution, our results are not sensitive to the upper bond of the selection function. Several modifications have been made to allow more sophisticate bias evolution function. Our results are consistent with Fig. 11 of [45].

Chapter 6

Conclusion

In this thesis, we present a theoretical framework for the prediction of number counts, both analytically and by means of simulations. This framework is based on fully relativistic linear perturbations of a spatially flat, isotropic and homogeneous space-time metric. In particular we did not assume any gauge condition. We have checked that the number of sources above a certain flux density threshold per solid angle is gauge invariant.

In previous works [45, 86, 87], the number density has been studied as a function of redshift. There the redshift distortion is one of the dominant effects in the radial direction. In our case, as shown in the chapter 2 the radial direction fluctuation comes from four effects, i.e. redshift distortions, physical distance fluctuations, variation of the source luminosities and spectral indices. This makes the evaluation more involved than the case when the redshifts of each source are accessible.

With the complete derivations of the covariant volume integral on the past light cone, we have identified several contributions in the differential number count fluctuations, including Doppler effect, generalized Sachs-Wolfe effect, lensing effect and astrophysical variations (luminosity and spectral index).

We revisited the angular two-point correlation function $w(\theta)$ and angular power spectrum C_l of the NVSS catalogue of radio galaxies. To model the galaxy distribution require not only accurate theoretical predictions, but also need to model and measure luminosity functions, luminosity and density evolution. Since the current redshift distribution of NVSS catalogue is more reliable than the luminosity function with evolution, our analyses is based on a fit of the redshift distribution of NVSS galaxies.

To obtain the true matter fluctuation, we spend significant attention to investigate systematic effects in the NVSS catalogue. In order to minimize the contribution of these effects in the cosmological analysis, we provide a new NVSS mask with 64.7% percent of sky, called NVSS65. We also find that it is essential to account for the cosmic radio dipole and to use a lower flux threshold. We found that our mask significantly improves the χ^2 value of the angular two-point correlation function on all angular scales.

For angular scales between 1 and 20 degrees, $w(\theta)$ agrees with the flat ΛCDM model without introducing primordial non-Gaussianity, which contrary to previous claims [75].

Thus we have shown that to fully explore the cosmological potential of continuum radio surveys, one has to understand and investigate the systematic effects related with flux calibration, especially direction dependent effects of the calibration. Besides, the effect of the cosmic radio dipole affects the reconstruction of higher multipole moments and the attempts to measure or constrain primordial non-Gaussianity.

To obtain an improved upper limit on $f_{\rm nl}$ or to constrain other cosmological parameters at a redshift of about unity is beyond the scope of this work, as it would need an extensive study of the uncertainties coming from our understanding of the density, luminosity and bias evolution of radio galaxies. However, our analysis shows, that the radio sky is in remarkable good agreement with the standard model of cosmology after Planck. It will also be interesting to improve the ISW analysis of the Planck-NVSS cross correlation by means of the new NVSS65 mask and to include a radio dipole correction, as well as a higher flux threshold.

As a response to the first part of the thesis, we also evaluated the next-to-leading order volume effects including redshift space distortion and gravitational lensing effect. Our results suggest that including the lensing effect can reduce the angular power spectrum by 30%. This number can be even larger if one considers the luminosity distance distortion in the luminosity function. Thus, the lensing effect can not be neglected in the radio continuum surveys angular power spectrum evaluation.

Our results further suggest that $w(\theta)$ from full sky radio continuum surveys can be used to constrain cosmological parameters at an epoch that is hardly accessible to other probes. Planned and upcoming surveys with instruments like LOFAR, ASKAP, MeerKAT and eventually SKA will allow us to reduce the shot noise, increase angular resolution and sensitivity, while covering all sky, extend the studies to several frequency bands (all of our discussion here is limited to 1.4 GHz) and improve the control of systematic effects (see [88, 89]). Finally, with these improvements radio survey precision cosmology will be accomplished in the nearly future.

Acknowledgements

This thesis was developed under the supervision of Prof. Dr. Dominik J. Schwarz. Firstly I would like to thank my supervisor Prof. Dr. Dominik J. Schwarz for his kindly and patiently advising. I have benefited a lot from the constructive discussions and inspiring colloquia that he organized during the last three years. I am also grateful to my second supervisor, Prof. Dr. Peter Schupp from the models of gravity research training group, for attending my presentations and for his valuable discussions and comments.

I would like to thank all members of theoretical high energy physics group in Bielefeld University for their various supports. Especially, I want to thank Dr. Matthias Rubart for proofreading this thesis and his revising opinions, and Thomas Luthe for English checking. My sincere thanks goes to Dr. Samae Bagheri, Florian Meyer, Isabel Oldengott and Jan Oldengott for making me feel warm and happy in the group and Dr. Daniel Boriero for plenty of interesting discussions as well as teaching me proposal writing. Besides, I also like to thank Gudrun and Susi for being the best secretaries from all over the world.

Thanks also goes to my colleagues in Models of Gravity research training group for enabling me to visit different research groups and making a lot of friends and so on.

Last but not least, I want to thank my fiancée for her understanding and my parents for everything they did for me, without them I could not have finished this thesis.

I acknowledge financial support from Deutsche Forschungsgemeinschaft(DFG) under grants RTG 1620 'Models of Gravity'. Their support enabled me to participate in several schools, workshops and conferences. I am grateful for the possibility to perform the numerical computations on the Nordrhein-Westfalen state computing cluster at RWTH Aachen. I acknowledge the use of the NVSS catalogue [10], provided by the National Radio Astronomy Observatory (NRAO). This work made extensive use of the GNU Scientific Library(GSL), HEALPIX [90] and CLASS [69, 91] packages.

References

[1] M.Colless. First results from the 2dF galaxy redshift survey. *Phil. Trans. Roy. Soc. Lond.*, A357:105, 1999. iv, 2, 3

[2] J.Loveday and J.Pier. The Sloan digital sky survey. 1998. iv, 2, 3

[3] M.J.Drinkwater et al. The WiggleZ Dark Energy Survey: Survey Design and First Data Release. *MNRAS*, 401:1429, 2010. iv, 2, 3

[4] Planck Collaboration. XI. Planck 2015 results. XI. CMB power spectra, likelihoods, and robustness of parameters. *ArXiv e-prints*, 2015. iv, 5

[5] R. D. Ekers and G. K. Miley. Radio Source Angular Sizes and Cosmology. In D. L. Jauncey, editor, *Radio Astronomy and Cosmology*, volume 74 of *IAU Symposium*, page 109, 1977. iv, 7

[6] P. N. Best, M. S. Longair, and H. J. A. Rottgering. Evolution of the aligned structures in z˜1 radio galaxies. *MNRAS*, 280:L9, 1996. iv, 9

[7] K. I. Kellermann. The cosmological deceleration parameter estimated from the angular-size/redshift relation for compact radio sources. *Nature*, 361:134, 1993. iv, 8, 10

[8] Planck Collaboration. XVI. Planck 2015 results. XV. Gravitational lensing. *ArXiv e-prints 1502.01591*, 2015. v, 8, 11

[9] T. Mauch and E. M. Sadler. Radio sources in the 6dFGS: Local luminosity functions at 1.4-GHz for star-forming galaxies and radio-loud AGN. *MNRAS*, 375:931, 2007. v, 35

[10] J. J. Condon, W. D. Cotton, E. W. Greisen, Q. F. Yin, R. A. Perley, G. B. Taylor, and J. J. Broderick. The nrao vla sky survey. *ApJ*, 115(5):1693, 1998. vii, 44, 45, 46, 50, 63, 72

[11] G. F. R. Ellis, R. Maartens, and M. A. H. MacCallum. *Relativistic Cosmology.* 1971. 1

[12] P. Sarkar, J. Yadav, B. Pandey, and S. Bharadwaj. The scale of homogeneity of the galaxy distribution in SDSS DR6. *MNRAS*, 399:L128, 2009. 2

[13] F. Sylos Labini. Inhomogeneities in the universe. *Journal of Cosmology*, 15:6110, 2011. 2

[14] A. H. Guth and S.Y. Pi. Fluctuations in the New Inflationary Universe. *Phys. Rev. Lett.*, 49:1110, 1982. 2

[15] S.W. Hawking. The Development of Irregularities in a Single Bubble Inflationary Universe. *Phys.Lett.*, B115:295, 1982. 2

[16] A. A. Starobinsky. Dynamics of Phase Transition in the New Inflationary Universe Scenario and Generation of Perturbations. *Phys.Lett.*, B117:175, 1982. 2

[17] J. M. Bardeen, P. J. Steinhardt, and M. S. Turner. Spontaneous Creation of Almost Scale - Free Density Perturbations in an Inflationary Universe. *Phys. Rev. D*, 28:679, 1983. 2

[18] J.C.Mather, . M.G.Hauser, C.L.Bennett, N.W.Boggess, E.S.Cheng, Jr.Eplee, H.T.Freudenreich, R.B.Isaacman, T.Kelsall, and S.Gulkis. Early results from the cosmic background explorer (cobe). *Advances in Space Research*, 11:181, 1991. 4

[19] E. M. Lifshitz and I. M. Khalatnikov. Investigations in relativistic cosmology. *Adv. Phys.*, 12:185, 1963. 4

[20] J. M. Bardeen. Radiative Transfer in Perturbed Friedmann Universes. *The Astronomical Journal Supplement*, 73:164, 1968. 5

[21] J. M. Bardeen. Gauge Invariant Cosmological Perturbations. *Phys. Rev. D*, 22:1882, 1980. 5

[22] U. H. Gerlach and U. K. Sengupta. Relativistic Equations for Aspherical Gravitational Collapse. *Phys. Rev. D*, 18:1789, 1978. 5

[23] Planck Collaboration. XVI. Planck 2013 results. XVI. Cosmological parameters. *A&A*, 571:A16, 2014. 5, 52

[24] C. Clarkson, G. Ellis, J. Larena, and O. Umeh. Does the growth of structure affect our dynamical models of the universe? The averaging, backreaction and fitting problems in cosmology. *Rept. Prog. Phys.*, 74:112901, 2011. 6

[25] V. Springel, C. S. Frenk, and S. D. M. White. The large-scale structure of the Universe. *Nature*, 440:1137, 2006. 6

[26] K. I. Kellermann. Radio Galaxies, Quasars, and Cosmology. *AJ*, 77:531, 1972. 6

[27] V. K. Kapahi. The Angular Size - Flux Density Relation. In D. L. Jauncey, editor, *Radio Astronomy and Cosmology*, volume 74 of *IAU Symposium*, page 119, 1977. 8

[28] M. Longair. *Galaxy Formation.* Springer-Verlag Berlin Heidelberg New York, 2008. 8

[29] E. E. Rigby, P. N. Best, M. H. Brookes, J. A. Peacock, J. S. Dunlop, H. J. A. Rottgering, J. V. Wall, and L. Ker. The luminosity-dependent high-redshift turnover in the steep spectrum radio luminosity function: clear evidence for downsizing in the radio-AGN population. *MNRAS*, 416:1900, 2011. 8

[30] D. Kirk et al. Cross correlation surveys with the Square Kilometre Array. *PoS*, AASKA14:020, 2015. 12

[31] M. Santos et al. Cosmology from a SKA HI intensity mapping survey. *PoS*, AASKA14:019, 2015. 12

REFERENCES

[32] V. Mukhanov. *Physical Foundations of Cosmology.* Cambridge University Press, Oxford, 2005. 13, 14

[33] S. M. Carroll. *Spacetime and geometry: An introduction to general relativity.* 2004. 14

[34] S. Weinberg. *Gravitation and Cosmology: Principles and Applications of the General Theory of Relativity.* Wiley-VCH , New York, 1972. 17

[35] M. Sasaki. The Magnitude - Redshift relation in a perturbed Friedmann universe. *MNRAS*, 228:653, 1987. 18, 24, 29

[36] T. Pyne and M. Birkinshaw. Null geodesics in perturbed space-times. *AJ*, 415:459, 1993. 18

[37] C. Bonvin, R. Durrer, and M. A. Gasparini. Fluctuations of the luminosity distance. *Phys. Rev. D*, 73:023523, 2006. [Erratum: Phys. Rev.D85,029901(2012)]. 18, 24, 29

[38] R. M. Wald. *General Relativity.* 1984. 18

[39] G. F. R. Ellis. *Proceedings of international school of physics, Course XLVII, General Relativity and Cosmology.* 1971. 22

[40] C. W. Misner, K. S. Thorne, and J. A. Wheeler. *Gravitation.* 1973. 22

[41] P. Schneider, J. Ehlers, and E. Falco. *Gravitational Lenses.* Berlin: Springer Verlag, 1992. 24

[42] L. Hui and P. B. Greene. Correlated Fluctuations in Luminosity Distance and the (Surprising) Importance of Peculiar Motion in Supernova Surveys. *Phys. Rev. D*, 73:123526, 2006. 24, 29

[43] J. Yoo, A. L. Fitzpatrick, and M. Zaldarriaga. A New Perspective on Galaxy Clustering as a Cosmological Probe: General Relativistic Effects. *Phys. Rev. D*, 80:083514, 2009. 24

[44] I. Heywood and M. J. Jarvis. Sample variance, source clustering and their influence on the counts of faint radio sources. *MNRAS*, 432:2625, 2013. 30

[45] C. Bonvin and R. Durrer. What galaxy surveys really measure. *Phys. Rev. D*, 84:063505, 2011. 31, 32, 66, 67, 68

[46] D. J. Bacon, S. Andrianomena, C. Clarkson, K. Bolejko, and R. Maartens. Cosmology with Doppler lensing. *MNRAS*, 443:1900, 2014. 33

[47] C. Bonvin. Effect of peculiar motion in weak lensing. *Phys. Rev. D*, 78(12):123530, 2008. 33

[48] J. Yoo. General Relativistic Description of the Observed Galaxy Power Spectrum: Do We Understand What We Measure? *Phys. Rev. D*, 82:083508, 2010. 34

[49] J. S. Dunlop and J. A. Peacock. The redshift cut-off in the luminosity function of radio galaxies and quasars. *MNRAS*, 247:19D, 1990. 34

[50] P. Schechter. An analytic expression for the luminosity function for galaxies. *ApJ*, 203:297, 1976. 34

[51] G. de Zotti, M. Massardi, M. Negrello, and J. Wall. Radio and millimeter continuum surveys and their astrophysical implications. *A&A Rev.*, 18:1, 2010. 38

[52] C. Blake, P. G. Ferreira, and J. Borrill. The angular power spectrum of NVSS radio galaxies. *MNRAS*, 351(3):923, 2004. 38, 62

[53] R.J.Barlow. *Statistics: A Guide to the Use of Statistical Methods in the Physical Sciences.* 1989. 39

[54] P.J.E. Peebles. *The Large-Scale Structure of the Universe.* Princeton Univ. Press, 1980. 40

[55] P. J. E. Peebles and M. G. Hauser. Statistical Analysis of Catalogs of Extragalactic Objects. III. The Shane-Wirtanen and Zwicky Catalogs. *ApJ*, 28:19, 1974. 40

[56] S. D. Landy and A. S. Szalay. Bias and variance of angular correlation functions. *ApJ*, 412:64, 1993. 40, 41

[57] G. F. R. Ellis and J. E. Baldwin. On the expected anisotropy of radio source counts. *MNRAS*, 206:377, 1984. 42

[58] N. Jarosik, C.L. Bennett, J. Dunkley, B. Gold, M.R. Greason, et al. Seven-Year Wilkinson Microwave Anisotropy Probe (WMAP) Observations: Sky Maps, Systematic Errors, and Basic Results. *ApJS*, 192:14, 2011. 42

[59] Planck Collaboration. XXVII. Planck 2013 results. XXVII. Doppler boosting of the CMB: Eppur si muove. *A&A*, 571:A27, 2014. 42

[60] C. Blake and J. Wall. Detection of the velocity dipole in the radio galaxies of the nrao vla sky survey. *Nature*, 416:150, 2002. 42, 48

[61] A. K. Singal. Large peculiar motion of the solar system from the dipole anisotropy in sky brightness due to distant radio sources. *ApJ*, 742:L23, 2011. 42

[62] C. Gibelyou and D. Huterer. Dipoles in the Sky. *MNRAS*, 427:1994, 2012. 42, 48

[63] M. Rubart and D. J. Schwarz. Cosmic radio dipole from NVSS and WENSS. *A&A*, 555:A117, 2013. 42, 48

[64] M. Rubart, D. Bacon, and D. J. Schwarz. Impact of local structure on the cosmic radio dipole. *A&A*, 565:A111, 2014. 42

[65] S. Ho, C. Hirata, N. Padmanabhan, U. Seljak, and N. Bahcall. Correlation of CMB with large-scale structure: I. ISW Tomography and Cosmological Implications. *Phys. Rev. D*, 78:043519, 2008. 44, 48

[66] C. Blake and J. Wall. Measurement of the angular correlation function of radio galaxies from the NRAO VLA Sky Survey. *MNRAS*, 329(2):L37, 2002. 46, 48

[67] M. Rubart. *The Cosmic Radio dipole.* PhD thesis, University Bielefeld, 2015. 48, 54

[68] D. C. Hoaglin and J. W. Tukey. *Exploring Data Tables, Trends, and Shapes.* John Wiley & Sons, Inc, 2006. 48

[69] E. Di Dio, F. Montanari, J. Lesgourgues, and R. Durrer. The CLASSgal code for Relativistic Cosmological Large Scale Structure. *J. Cosmology Astropart. Phys.*, 1311:044, 2013. 52, 67, 72

---

[70] M.H. Brookes, P.N. Best, J.A. Peacock, H.J.A. Rottgering, and J.S. Dunlop. A Combined EIS-NVSS Survey Of Radio Sources (CENSORS) III: Spectroscopic observations. *MNRAS*, 385:1297, 2008. 52

[71] A. Marcos-Caballero, P. Vielva, E. Martinez-Gonzalez, F. Finelli, A. Gruppuso, and F. Schiavon. A new model for NVSS galaxy catalogue using the redshift distribution and halo minimum mass. *ArXiv e-prints 1312.0530*, 2013. 52, 59, 62

[72] H. J. Mo and S. D. M. White. An Analytic model for the spatial clustering of dark matter halos. *MNRAS*, 282:347, 1996. 53

[73] R. K. Sheth and G. Tormen. Large scale bias and the peak background split. *MNRAS*, 308:119, 1999. 53

[74] C. G. Lacey and S. Cole. Merger rates in hierarchical models of galaxy formation. 2. Comparison with N body simulations. *MNRAS*, 271:676, 1994. 53

[75] J.Q. Xia, M. Viel, C. Baccigalupi, G. De Zotti, S. Matarrese, et al. Primordial Non-Gaussianity and the NRAO VLA Sky Survey. *ApJ*, 717:L17, 2010. 53, 60, 69

[76] R. Scoccimarro, R. K. Sheth, L. Hui, and B. Jain. How many galaxies fit in a halo? Constraints on galaxy formation efficiency from spatial clustering. *AJ*, 546:20, 2001. 53

[77] J. Lee and S. F. Shandarin. The Cosmological mass distribution function in the Zeldovich approximation. *AJ*, 500:14, 1998. 53

[78] Planck Collaboration. XXI. Planck 2015 results. XXI. The integrated Sachs-Wolfe effect. *ArXiv e-prints 1502.01595*, 2015. 53, 64

[79] V. Desjacques and U. Seljak. Primordial non-Gaussianity from the large-scale structure. *Classical and Quantum Gravity*, 27(12):124011, 2010. 60

[80] C. Hernndez-Monteagudo. Revisiting the wmap-nvss angular cross correlation. a skeptic's view. *A&A*, 520:A101, 2010. 62

[81] P. Vielva, E. Martínez-González, and M. Tucci. Cross-correlation of the cosmic microwave background and radio galaxies in real, harmonic and wavelet spaces: detection of the integrated Sachs-Wolfe effect and dark energy constraints. *MNRAS*, 365:891, 2006. 64

[82] Planck Collaboration. XIX. Planck 2013 results. XIX. The integrated Sachs-Wolfe effect. *A&A*, 571:A19, 2014. 64

[83] R. Fernández-Cobos, P. Vielva, D. Pietrobon, A. Balbi, E. Martínez-González, and R. B. Barreiro. Searching for a dipole modulation in the large-scale structure of the Universe. *MNRAS*, 441:2392, 2014. 64

[84] J. Kim and P. Naselsky. Anomalous parity asymmetry of the Wilkinson Microwave Anisotropy Probe power spectrum data at low multipoles. *ApJ*, 714:L265, 2010. 65

[85] N. Kaiser. Clustering in real space and in redshift space. *MNRAS*, 227:1, 1987. 66

[86] J. Yoo. Complete Treatment of Galaxy Two-Point Statistics: Gravitational Lensing Effects and Redshift-Space Distortions. *Phys. Rev. D*, 79:023517, 2009. 67, 68

[87] A. Challinor and A. Lewis. The linear power spectrum of observed source number counts. *Phys. Rev. D*, 84:043516, 2011. 68

[88] A. Raccanelli et al. Cosmological Measurements with Forthcoming Radio Continuum Surveys. *MNRAS*, 424:801, 2012. 70

[89] M. Jarvis, D. Bacon, C. Blake, M. Brown, S. Lindsay, et al. Cosmology with SKA Radio Continuum Surveys. *PoS*, AASKA14:018, 2015. 70

[90] K.M. Gorski, E. Hivon, A.J. Banday, B.D. Wandelt, F.K. Hansen, et al. HEALPix - A Framework for high resolution discretization, and fast analysis of data distributed on the sphere. *ApJ*, 622:759, 2005. 72

[91] J. Lesgourgues and T. Tram. The Cosmic Linear Anisotropy Solving System (CLASS) IV: efficient implementation of non-cold relics. *J. Cosmology Astropart. Phys.*, 1109:032, 2011. 72

[1]

---

[1] The numbers at the end of each reference stand for the page number of this thesis.